Optical forces
in the
T-matrix formalism

Relatore: Presentata da:

Prof.   Paolo Polimeno
Cristian Degli Esposti-Boschi

Correlatori:

Dr.ssa Maria Antonia Iatì
Dr. Onofrio M. Maragò

To the Sun of my life and my family ...

Abstract

Le pinzette ottiche, fasci laser fortemente focalizzati, sono uno strumento cruciale per la manipolazione e lo studio senza contatto meccanico di particelle micro- e nanoscopiche di diversa natura che spaziano da componenti organici come biomolecole, batteri, cellule, fino a nanoparticelle plasmoniche, nanotubi, nanofili e perfino singoli atomi. Nonostante le tantissime applicazioni interdisciplinari, solo di recente si è riusciti a sviluppare una modellizzazione teorica accurata per il range della mesoscala che vada oltre le forti approssimazioni utilizzate per il calcolo delle forze ottiche su particelle molto più piccole (approssimazione di dipolo) o molto più grandi (ottica geometrica) della lunghezza d'onda della luce.

In questo ambito di ricerca si inserisce il nostro lavoro di tesi che si basa sull'utilizzo del metodo della matrice di transizione (T-matrix) per il calcolo delle forze ottiche su particelle sferiche e nanofili alla mesoscala. Il formalismo della T-matrix, introdotto da Waterman negli anni '70, costituisce attualmente uno dei metodi più accurati per il calcolo dello scattering elettromagnetico da particelle non-sferiche, sia isolate che interagenti in strutture composite. L'idea di espandere i campi incidenti e diffusi in armoniche sferiche vettoriali e di connettere i coefficienti di espansione attraverso una matrice di transizione si è dimostrato estremamente efficace anche nell'ambito della modellizzazione delle forze ottiche.

In questo lavoro di tesi, abbiamo studiato le forze ottiche su nano e microstrutture intrappolate. In primo luogo, abbiamo studiato la dipendenza delle forze dalle dimensioni di particelle di morfologia sferica e filiformi (nanofili) di polistirene. Successivamente, abbiamo dimostrato per la prima volta come, rompendo la simmetria cilindrica in nanofili di ossido di zinco, possa essere evidenziata una componente di forza non conservativa legata all'elicità della luce e proporzionale al momento lineare di Belinfante. Gli effetti di questa forza ottica trasversa, tradizionalmente ritenuta 'virtuale', sono stati di recente misurati in esperimenti con onde evanescenti e nell'intrappolamento di nanofili.

Contents

Introduction

Light can exert a mechanical action on matter. This simple concept, known since Kepler's explanation of comet tails, has brought to a real scientific revolution with the advent of the laser [1, 2, 3]. *Optical tweezers* [4], in their simplest configuration, are instruments based on a tightly focused laser beam that is capable to trap and manipulate a wide range of particles in its focal high intensity spot [5]. Since their invention in 1986 by Sir Arthur Ashkin [4], they have become a key technique for the trapping, manipulation, and characterization of atoms, microscopic and nanoscopic particles, such as nanostructures (nanotubes, nanowires, plasmonic nanoparticles, layered materials), biomolecules, viruses, bacteria and cells [5, 6, 7, 8, 9, 10, 11, 12]. When used as a force transducer, optical tweezers are able to measure forces in the femtonewton range [5, 12]. The concept of photonic force microscopy has been also developed by scanning a trapped particle over surfaces in a liquid environment and sensing the force interaction between trapped probe and surface [13, 14].

Despite the tremendous progress in optical trapping techniques, the development of an accurate theoretical modeling for optical tweezers has been slower and often based on strong approximations [12]. In the limiting cases of spherical particles either much smaller (dipole approximation) [15] or much larger (ray optics) [16] than the trapping wavelength, the force in optical tweezers separates into different contributions: a conservative gradient force, proportional to the light intensity gradient, responsible for trapping, and a non-conservative scattering force, proportional to the light intensity that generally is detrimental for trapping, but fundamental for optical manipulation and laser cooling [5, 12]. However, for non-spherical particles or at intermediate (meso)scale, the situation is more complex and this traditional identification of gradient and scattering force is more elusive [17]. Moreover, shape and composition can have dramatic consequences for optically trapped particle dynamics [12, 18, 19].

In this context, the aim of our work has been to study and exploit electromagnetic scattering theory within the transition matrix formalism (T-

matrix) to accurately calculate optical forces on model particles of spherical and linear shape (nanowires). The T-matrix method, initially introduced by Waterman [20], is among the most efficient tools for the accurate calculation of light scattering from non-spherical particles, both isolated and interacting in composite structures [21]. It is based on the calculation of a linear operator (the *Transition* operator) which, acting on the multipole amplitudes of the incident fields, gives as a result the multipole amplitudes of the scattered field. For a homogeneous spherical particle under plane wave illumination this is simply Mie theory [22]. The T-matrix approach is particularly advantageous when we deal with particles that can be modeled as cluster or aggregates of spheres, spheres with spherical (eccentric) inclusions, and multilayered spheres [21]. This technique takes into proper account the multiple scattering processes occurring among the spherical subunits composing the aggregate and the contribution of all the details of the model structure. Optical properties of composite scatterers can be exactly calculated without introducing any approximation except the truncation of the expansion of the fields, being able to check the convergence of the results at every step. The elements of the T-matrix contain all the information on the particle nature (refractive index, size relative to the wavelength, and shape) and on the orientation of the scatterer with respect to the incident field. A fundamental feature is that the T-matrix is independent of the propagation direction and polarization states of the incident and of the scattered fields. This means that, once we compute the T-matrix elements, we do not need to compute them again if the incident field direction and polarization state changes [23]. This is a key property when dealing with optical trapping calculations since the particle has to be placed in different positions to reconstruct the optical force within the focal spot [17]. Thanks to the flexibility and the accuracy of the T-matrix technique, we have the possibility to explore several systems and configurations in a broad range of applications, going from interstellar dust modelling [24, 25] to the study of the behaviour of plasmonic systems [26].

The outline of the thesis is as follows. In the first chapter we give a brief overview on optical forces and optical tweezers. After an historical review, we introduce the basic concepts underlying the principles of optical trapping. We focus on two different particle size regimes, much larger (ray optics) and much smaller (dipole approximation) than the light wavelength, where simple expressions are obtained thanks to the approximated approaches. We conclude this review chapter by discussing some implications of optical forces in the recent field of optomechanics with levitated particles.

The second chapter deals with the electromagnetic theory of optical forces and light scattering in the T-matrix formalism. After introducing the Maxwell

stress tensor, we describe the general equations from which optical forces and torques can be calculated within electromagnetic scattering theory. Thus, we introduce the T-matrix formalism discussing the special cases of Mie theory and light scattering by aggregates of spheres. Within this formalism, we describe how to calculate optical forces both from plane wave and optical tweezers.

In the third chapter we present numerical results on optical trapping of dielectric (polystyrene) spherical particles and nanowires. We use numerical codes based on light scattering in the T-matrix framework to calculate optical forces and optical trapping properties as a function of particle size (size scaling) for both spheres and nanowires. Then, we discuss how shape and symmetry controls the mechanical effects of light at the mesoscale.

The fourth chapter is devoted to spin-dependent optical forces, a novel aspect that has been recently investigated theoretically and experimentally. First, we discuss the role and implications of Belinfante's correction to the energy-momentum tensor associated with the classical free electromagnetic field. Then, we present novel results associated with the onset of spin-dependent optical force components in tilted optically trapped ZnO nanowire. Our theoretical results are complementary to recent experimental work at CNR-IPCF that shows evidence of non-conservative spin-dependent thermal dynamics of optical trapped ZnO nanowires.

Chapter 1

Optical forces and optical tweezers

Here we give a brief overview on optical forces and optical tweezers. After an historical outline, we introduce the basic concepts underlying the principles of optical trapping. We focus on two different particle size regimes, much larger (ray optics) and much smaller (dipole approximation) than the light wavelength, where approximations lead to simple expressions for the optical forces. Finally, we discuss some implications of optical forces in the recent field of optomechanics with levitated particles.

1.1   Historical perspective

Historically, the idea that light exerts a mechanical action on matter has been known since the explanation of comet tails given by Kepler [5, 27]. In fact, comets generally show two tails while approaching the Sun. A first tail, more diffused, composed by dust and ice particles formed by the radiation pressure of the solar light; and a second one composed of ions and charged particles due to the solar wind. It was only in 1873 that James C. Maxwell gave the first theoretical explanation of radiation pressure [28]. He demonstrated within his electromagnetic theory that light can exert a force on matter due to the momentum exchanged between light and matter. Since this momentum exchange is extremely small, only in 1901 Lebedev [29], Nichols and Hull [30] provided a first experimental evidence of the radiation pressure due to an arc or electric lamps on a mirror fixed on a torsion balance. Other experiments were carried out during the next decades but, because of the non coherent nature of the light sources, the results were small and hard to be detected. Only from the 1960s, radiation pressure and its applicability
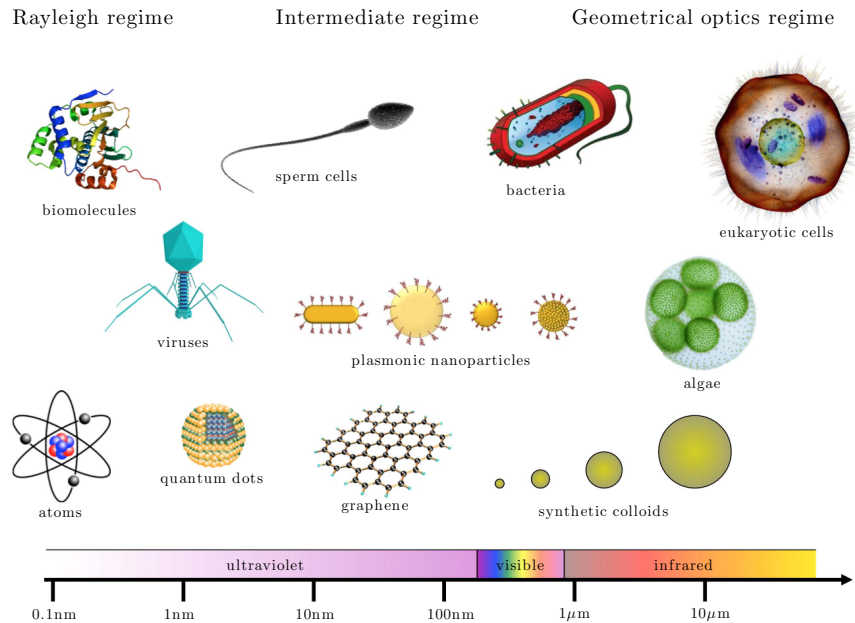
Figure 1.1: Optical trapping of particles in different regimes. Optical tweezers are able to confine atoms, viruses, small nanostructures, for which a dipole approximation can often give a reasonable account of optical forces (Rayleigh regime). In the opposite size regime optical trapping of bacteria, algae, cells, and microparticles can be studied using geometrical optics. The intermediate mesoscale is instead the most interesting and complex and a full electromagnetic theory must be used. From Ref. [5].

have been better understood thanks to the invention and availability of laser sources [31] that, compared to standard lamps, have increased drastically the intensity of the electromagnetic fields provided.

In the early 1970s, Arthur Ashkin, at Bell laboratories, while trying to reproduce the effects of the solar wind, demonstrated that the motion of microscopic particles [2] and neutral atoms [1] could be altered by laser-induced optical forces. In particular, he found out an unexpected effect: the micro-spherical particles suspended in water were attracted perpendicular to the propagation axis and pushed in the propagation direction [2]. This attraction is due to the *gradient force* perpendicular to the propagation axis and it is caused by the focusing of the laser beam [3]. After the discovery of the optical gradient force component, Ashkin built a first optical trap made of two focussed counterpropagating laser beams in order to balance the detrimental effects of radiation pressure and get a stable optical trap [3]. This

kind of trap is a static trap since the two lasers fix, on average, the particle's position along the propagation axis, unless the power of one of the two beams is changed. In this situation the particle can shift along the propagation direction. Soon after, in 1971 Ashkin demonstrated the first levitation trap. In this case the radiation pressure is balanced by gravity and the gradient force keeps the sample trapped [32]. The restriction of this method is that the maximum radiation pressure applicable is equal to the gravity. This kind of trap is generally not very stable and the sample can be moved only along the propagation direction. A real breakthrough occurred in 1986, when all the problems encountered before were solved by using a highly focussed laser beam [4]. Ashkin and his collaborators demonstrated that by using a *high numerical aperture* objective the focal spot is so tight that it is possible to obtain a gradient force also along the propagation direction. This force is directed towards the focal spot and can be used to trap and manipulate dielectric micro-spheres and atoms, this technique is called *optical tweezers* [5]. The applications of optical forces and optical tweezers in atomic physics with the development of techniques for atom trapping and cooling lead to the Nobel prize in Physics in 1997 for Steven Chu, Claude Cohen-Tannoudji and William D. Phillips [3, 5].

Since its first demonstration, optical tweezers are commonly used tools for the manipulation of micro- [9, 10] and nanostructures [12, 33, 34] and as a force transducer with resolution at the femtonewton [35]. As shown in Fig. (1.1), optical tweezers find applications in many fields of physics, biology, chemistry and material sciences. They are useful tools to sort and organize cells, control bacterial motion, measure linear and torsional forces, alter biological structures via modification of cellular membranes, cellular fusion, or the interaction between red blood cells and viruses [6, 7, 11, 36] with the possibility to apply and measure forces with femtonewton sensitivity on micro- and nanometer-sized particles [13, 35, 37, 38].

1.2   Theory of optical trapping and approximations

Optical trapping of particles is a consequence of the radiation force that stems from the conservation of electromagnetic momentum upon scattering [5]. Historically, the theoretical understanding of this physical process has been investigated through the use of suitable approximations that depend on the size of the particle. For homogeneous spherical particles, accurate evaluation of optical forces can be obtained by Mie theory [22]. In general, when

we study the scattering process involving non-spherical or non-homogenous particles, we must use a full electromagnetic theory based on the Maxwell's equations [23] and the integration of the Maxwell stress tensor [5]. Such calculations can be extremely complex and often obtaining the radiation forces could result in computational intensive procedures. For this reason different methods, such as the transition matrix (T-matrix) approaches [20, 21], have been developed to solve the scattering problem and calculate optical forces more efficiently. We will discuss this method in details in the next chapter, while here we give an overview of the approximated approach that often can grant a fast and simple way to obtain reasonable results in specific regimes.

For calculating optical forces acting on spherical or quasi-spherical particles, it is customary to identify several regimes which depend on the particle size [5]. For each regime, simplifications and approximations have been made for a better and more qualitative understanding and calculation of optical forces. The *size parameter* x is crucially used to determine the range of validity of these approximations:

$$x = k_{\mathrm{m}}a = \frac{2\pi n_{\mathrm{m}}}{\lambda_0}a \tag{1.1}$$

where $k_{\mathrm{m}} = 2\pi n_{\mathrm{m}}/\lambda_0$ is the light wavenumber in the medium surrounding the particle, a is the particle radius, λ_0 is the laser wavelength in vacuum used for trapping and n_{m} is the refractive index of the surrounding medium, no-magnetic in the optical wavelength with magnetic permeability $\mu_{\mathrm{m}} = 1$, as water (n_{m}=1.33) or air (n_{m}=1).

When the particle size is much bigger than the wavelength of the laser beam, that is $k_{\mathrm{m}}a \gg 1$, optical trapping forces can be calculated by the so-called *ray optics regime* or geometrical optics approximation [39]. The accuracy of this approximation increases with the size parameter, whereas the exact theories become unpractical due to the increasing computational complexity. This makes ray optics very useful when dealing with large particles.

In the *intermediate regime*, that is when the particle size is comparable with the light wavelength ($k_{\mathrm{m}}a \simeq 1$), we need a complete wave-optical modeling of the particle-light interaction to calculate the trapping forces and, for example, the T-matrix approach is convenient.

If the size of the particle is much smaller than λ_0 ($k_{\mathrm{m}}a \ll 1$), we can adopt the *Rayleigh approximation* and consider the particle as a dipole [40] or a collection of dipoles [41]. This means we are considering the electromagnetic fields homogeneous inside the particle under this condition:

$$\left| \frac{n_{\mathrm{p}}}{n_{\mathrm{m}}} \right| ka \ll 1 \tag{1.2}$$

where n_{p} is the refractive index of the particle. This condition has to be considered when we deal with high refractive index dielectric particles (*e.g.*, silicon) or noble metal (*e.g.*, gold, silver) nanoparticles, where the presence of plasmonic resonances dominate the optical response [26].

1.3 Ray optics regime $(x \gg 1)$

We start by considering a particle with refractive index n_{p}, immersed in a medium with refractive index $n_{\mathrm{m}} < n_{\mathrm{p}}$. In the ray optics regime the optical field is described by considering it as a collection of N light rays and employing the tools of geometrical optics [5]. Each ray carries with it an portion of the incident power P_{i} so that the total power is $P = N \sum_{\mathrm{i}} P_{\mathrm{i}}$ and a linear momentum per second $n_{\mathrm{m}} P_{\mathrm{i}}/c$. When a ray impinges on a surface with an incident angle θ_{i}, it will be partly reflected and partly transmitted with a transmitted angle θ_{t}, according to the well-known Snell's law [42]. As a consequence of energy conservation, the power is split between the reflected and transmitted part of the ray following Fresnel coefficients [43]. Moreover, at each scattering event, the ray changes its direction and hence its momentum causing a reaction force on the center-of-mass of the particle. Thus, the force associated with the reflection and transmission of a ray $\mathbf{r}_{\mathrm{i}}$ and power P_{i} in the direction $\hat{\mathbf{r}}_{\mathrm{i}}$ is written as:

$$\mathbf{F}_{\mathrm{ray},0} = \frac{n_{\mathrm{m}} P_{\mathrm{i}}}{c} \hat{\mathbf{r}}_{\mathrm{i}} - \frac{n_{\mathrm{m}} P_{\mathrm{r}}}{c} \hat{\mathbf{r}}_{\mathrm{r}} - \frac{n_{\mathrm{p}} P_{\mathrm{t}}}{c} \hat{\mathbf{r}}_{\mathrm{t}}. \tag{1.3}$$

where $\hat{\mathbf{r}}_{\mathrm{r}}$, P_{r} and $\hat{\mathbf{r}}_{\mathrm{t}}$, P_{t} are the unit vector and power in the direction of the reflected and transmitted rays, respectively. Most of the power carried by the incident ray is delivered to the transmitted ray that travels inside the particle until it impinges on the opposite surface. Here it will be reflected and transmitted again and a large portion of the power will be transmitted outside the sphere. The process will continue until all light escapes from the sphere. By considering these reflection and refraction events the optical force can be calculated directly as [16, 43]:

$$\mathbf{F}_{\mathrm{ray}} = \frac{n_{\mathrm{m}} P_{\mathrm{i}}}{c} \hat{\mathbf{r}}_{\mathrm{i}} - \frac{n_{\mathrm{m}} P_{\mathrm{r}}}{c} \hat{\mathbf{r}}_{\mathrm{r}}^{(0)} - \sum_{j=1}^{+\infty} \frac{n_{\mathrm{p}} P_{\mathrm{t}}^{(j)}}{c} \hat{\mathbf{r}}_{\mathrm{t}}^{(j)}. \tag{1.4}$$

The optical force $\mathbf{F}_{\mathrm{ray}}$ has components only in the incidence plane and can be split in two perpendicular components. The component in the direction
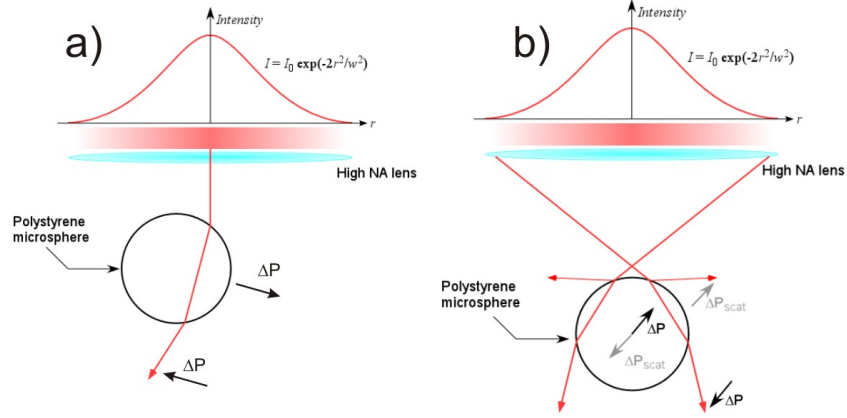
Figure 1.2: Principles of optical trapping in ray optics regime for particles with size parameter $x \gg 1$. (a) A spherical particle of refractive index n_{p} is suspended in a medium (generally water) of refractive index $n_{\mathrm{m}} < n_{\mathrm{p}}$ and illuminated by a Gaussian laser beam. Refraction of a ray, composing the beam, as it crosses the sphere implies a change of linear momentum of ray, and hence an equal and opposite transfer of momentum from the ray to the sphere. The gradient in light intensity (number of rays carrying different power) across the sphere produces a net transverse force towards the beam axis, *i.e.*, an optical gradient force. (b) To achieve trapping in the axial z-direction requires focussing of the beam where a similar considerations for refraction providing an optical gradient force towards the focus can be made. From Ref. [13].

of the incoming ray $\hat{\mathbf{r}}_{\mathrm{i}}$ represents the *scattering force* $\mathbf{F}_{\mathrm{ray,scat}}$, that pushes the particle away from the center of the trap. The component perpendicular to the incoming ray is the *gradient force* $\mathbf{F}_{\mathrm{ray,grad}}$, that pulls the particle towards the optical axis when $n_{\mathrm{m}} < n_{\mathrm{p}}$. Instead, if $n_{\mathrm{m}} > n_{\mathrm{p}}$ the particle is pushed away from the high intensity focal region.

$$\mathbf{F}_{\mathrm{ray}} = \mathbf{F}_{\mathrm{ray,scat}} + \mathbf{F}_{\mathrm{ray,grad}} \tag{1.5}$$

It is often useful to define the dimensionless quantities (*trapping efficiencies*) obtained dividing the force components $F_{\mathrm{ray,scat}}$ and $F_{\mathrm{ray,grad}}$ by $n_{\mathrm{m}}P_{\mathrm{i}}/c$, that quantify how efficiently the momentum is transferred from the ray to the particle.

10

For a circularly polarized ray on a sphere Ashkin derived the following theoretical expression for the scattering and gradient efficiencies [16]:

$$
\begin{aligned}
Q_{\text{scat}} &= 1 + R\cos 2\theta_{\text{i}} - T^2 \frac{\cos(2\theta_{\text{i}} - 2\theta_{\text{r}}) + R\cos 2\theta_{\text{i}}}{1 + R^2 + 2R\cos 2\theta_{\text{r}}}, \\
& \tag{1.6} \\
Q_{\text{grad}} &= R\sin 2\theta_{\text{i}} - T^2 \frac{\sin(2\theta_{\text{i}} - 2\theta_{\text{r}}) + R\sin 2\theta_{\text{i}}}{1 + R^2 + 2R\cos 2\theta_{\text{r}}}
\end{aligned}
$$

where R and T are the (intensity) Fresnel reflection and transmission coefficients and θ_{i} and θ_{r} are the incidence and transmission angle relative to the scattering of the incident beam.

In general, if more than one ray interacts with a particle, the total force is given by the sum of the forces generated by the reflection and refraction of each ray. To model an optical trap we need to model a highly focused laser beam [see Fig. (1.2)], that means a set of many rays that converge at a very large angle in the focal spot, and hence sum up all contributions from each ray forming the beam. This means that the total force acting on the particle is the sum of all the contributions from each ray forming the beam. Considering Eq. (1.3), the force acting on the centre of mass of the sphere is

$$
\mathbf{F}_{\text{GO}} = \sum_m \mathbf{F}_{\text{ray}}^{(m)} = \sum_m \left[\frac{n_{\text{m}} P_{\text{i}}^{(m)}}{c} \hat{\mathbf{r}}_{\text{i}}^{(m)} - \frac{n_{\text{m}} P_{\text{r}}^{(m)}}{c} \hat{\mathbf{r}}_{\text{r},0}^{(m)} - \sum_{j=1}^{+\infty} \frac{n_{\text{p}} P_{\text{t},j}^{(m)}}{c} \hat{\mathbf{r}}_{\text{t},j}^{(m)} \right].
\tag{1.7}
$$

For a single-beam optical tweezers, the focused rays will generate a restoring force proportional to the particle's displacement from an equilibrium point, that is for small displacements optical trapping can be modeled as an harmonic response. Due to the scattering force, the particle's is displaced from the nominal focus to an equilibrium position $\mathbf{C}_{eq} = [x_{\text{eq}}, y_{\text{eq}}, z_{\text{eq}}]$. Thus, for small displacements optical trapping forces are modeled as:

$$
\begin{aligned}
F_x &\approx -\kappa_x(x - x_{\text{eq}}) \\
F_y &\approx -\kappa_y(y - y_{\text{eq}}) \\
F_z &\approx -\kappa_z(z - z_{\text{eq}})
\end{aligned}
\tag{1.8}
$$

where κ_x, κ_y and κ_z are the *trap stiffnesses* or *spring constants* of the trap. Calculating or measuring the spring constants, we can obtain a calibration of the optical trap.

The geometrical optics approach can be also used when we deal with non spherical particles, such as cylindrical objects. The basic interaction of the

ray with this kind of particles is the same introduced in Eq. (1.3) but now two new aspects must be considered: *induced torque* and *transverse radiation force*. Induced torque is calculated from the difference of the angular momentum associated with the incoming and outgoing ray with respect to a pole [5]. Also in this case, the total torque on the object can be obtained as the sum of the torque produced by each ray, $\mathbf{\Gamma} = \sum_m \mathbf{\Gamma}_{\text{ray}}^{(m)}$. For example, the effect of the torque due to the rays is to align a cylindrical particle along the optical axis. The second aspect, the transverse radiation force, yields the optical lift effect [44]. This component arises from the anisotropic shape of non-spherical particles and generates a motion transversely to the incident light propagation direction. We can note that the accuracy of ray optics approximation increases with the size of the particle, whereas exact electromagnetic theories become unpractical due to the increasing computational complexity. Thus, ray optics has not only a pedagogical value but represents a key technique for modeling optical trapping of large particles [45].

1.4   Focusing

The easiest and most used configuration of optical tweezers is the single-beam optical trap as devised by Ashkin in 1986 [4]. This is obtained by a single highly-focused light beam. In fact, rays originating from diametrically opposite points of a high numerical aperture (NA) focusing lens produce in practise a set of rays that converge at very large angle [see Fig. (1.2)]. While the ray optics view is extremely useful for rapid calculations, it misses out many aspects of the focusing process that have a crucial importance when performing accurate modelling. Thus, here we give a brief description on the focusing of a paraxial optical beam by an ideal aplanatic optical lens [46, 47]. A sketch of the focusing process of this ideal optical tweezers is shown in Fig. (1.3).

Using the Abbe's sine condition, the deflection angle θ at position $\mathbf{R}$ (the intersection point of a ray with aplanatic lens p_2) is:

$$\theta = \arcsin\left(\frac{\rho}{f}\right) = \arcsin\left(\rho \, \frac{\text{NA}}{n_{\text{m}} R}\right) \tag{1.9}$$

where ρ is the radial coordinate of the incident wave, R is the radius of the iris, n_{m} is the index of refraction for the medium beyond p_2 and NA is the *numerical aperture* of the objective lens:

$$\text{NA} = n_{\text{m}} \sin(\theta_{\text{max}}) = n_{\text{m}} \frac{R}{f} \tag{1.10}$$
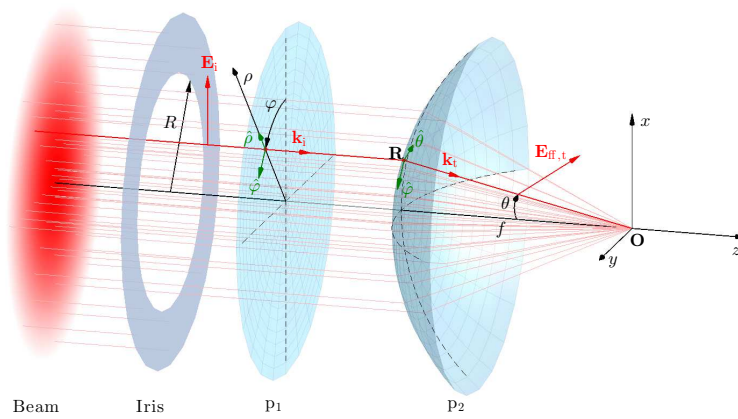
Figure 1.3: An optical beam crosses an aperture stop, or iris, with radius R and then propagates toward the principal plane p_1 of the lens and is transferred to the principal plane p_2, which is a spherical surface with centre at the focal point $\mathbf{O}$ and with radius equal to the focal length f. The diffraction that occurs inside the objective is modelled by propagating the electromagnetic wave from the aperture stop to the principal plane p_1. The aperture stop is often placed in the back focal plane, *i.e.*, at a distance f from p_1, which results in a telecentric imaging system. At p_2, the beam is refracted and focused towards $\mathbf{O}$. Taken from Ref. [5].

13

with θ_{max} angle over which the rays are focused and which determines the trapping characteristics of the focus. The complex focused field $\mathbf{E}_{\mathrm{f}}(x, y, z)$ near $\mathbf{O}$ is then:

$$\mathbf{E}_{\mathrm{f}}(x, y, z) = \frac{ik_{\mathrm{m}}fe^{-ik_{\mathrm{m}}f}}{2\pi} \int\limits_{0}^{\theta_{\mathrm{max}}} \sin\theta \int\limits_{0}^{2\pi} \mathbf{E}_{\mathrm{ff,m}}(\theta, \varphi) e^{i[k_{\mathrm{m},x}x + k_{\mathrm{m},y}y]} e^{ik_{\mathrm{m},z}z} \, \mathrm{d}\varphi \, \mathrm{d}\theta \ .$$

(1.11)

This is the integral representation of the focused field [48] where the plane wave *angular spectrum representation* is used such as $\mathbf{E}_{\mathrm{ff,m}}(\theta, \varphi)$ is the so called *far field*.

1.5 Dipole approximation regime $(x \ll 1)$

When the particle size parameter is small, $x \ll 1$, optical trapping forces can be calculated exploiting a dipole approximation, *i.e.*, the particle can be approximated as a small induced dipole immersed in an electromagnetic field $\mathbf{E}(\mathbf{r}, t)$, which can be considered homogeneous inside the particle $(x|n_{\mathrm{p}}/n_{\mathrm{m}}| \ll 1)$ [40]. A key example is that of a neutral atom. When placed in an external electric field, the negative electron cloud surrounding the positive nucleus will be displaced, leading to a separation between the centre-of-mass of the positive and negative charge distributions. An induced dipole is thus generated that experiences electrostatic forces arising from its interaction with the inducing electric field. Consequently, an oscillating electromagnetic field, such as that of the laser beam used for an optical tweezers, induces an oscillating dipole, which also experiences forces arising from its interaction with the inducing electromagnetic field. Furthermore, an oscillating dipole radiates an electromagnetic field that can produce a mechanical effect on other induced dipoles leading to, in some cases, *optical binding* [5, 49].

This picture can be extended to a small particle, so that if the external field is not too large, the induced dipole moment, $\mathbf{p}(\mathbf{r}, t)$, can be expressed in terms of a linear polarisability:

$$\mathbf{p}(\mathbf{r}, t) = \alpha_{\mathrm{p}}\mathbf{E}(\mathbf{r}, t) \tag{1.12}$$

where α_{p} is the complex polarisability of the particle with respect to the surrounding medium and it is given by [50]:

$$\alpha_{\mathrm{p}} = \alpha_0 \left(1 - i\frac{k_{\mathrm{m}}^3 \alpha_0}{6\pi\varepsilon_{\mathrm{m}}}\right)^{-1} \tag{1.13}$$

with ε_{m} dielectric permittivity of the medium and α_0 being the static Clausius-Mossotti polarisability:

$$\alpha_0 = 3V\varepsilon_{\mathrm{m}} \left(\frac{\varepsilon_{\mathrm{p}} - \varepsilon_{\mathrm{m}}}{\varepsilon_{\mathrm{p}} + 2\varepsilon_{\mathrm{m}}} \right) \tag{1.14}$$

where V is the particle volume and ε_{p} dielectric permittivity of the particle.

It is now useful to introduce the general concept of cross-sections that are linked to the light scattering process and here we define them within the dipole approximation. When a dipole, or more generally a particle, is illuminated by an electromagnetic wave, it both scatters and absorbs power. The light-particle interaction, including optical forces, can be described in terms of the following quantities:

- the *scattering cross-section*, σ_{scat}, that multiplied by the power density of the incident wave, represents the rate at which energy is removed from the electromagnetic wave due to scattering in all directions;

- the *absorption cross-section*, σ_{abs}, that multiplied by the power density of the incident wave, represents the rate at which energy is absorbed, resulting in the heating of the particle;

- the *extinction cross-section*, σ_{ext}, that describes the rate at which energy is removed from the electromagnetic wave through scattering and absorption and therefore $\sigma_{\mathrm{ext}} = \sigma_{\mathrm{scat}} + \sigma_{\mathrm{abs}}$

These cross-sections represent the apparent area of the object on which scattering, absorption, and extinction processes take place.

For an electric dipole of polarisability α_{p}, we can write the cross-sections in accordance with Poynting's theorem [5]:

$$\sigma_{\mathrm{ext,d}} = \frac{k_{\mathrm{m}}}{\varepsilon_{\mathrm{m}}} \Im\{\alpha_{\mathrm{p}}\} \tag{1.15}$$

$$\sigma_{\mathrm{scat,d}} = \frac{k_{\mathrm{m}}^4}{6\pi\varepsilon_{\mathrm{m}}^2} |\alpha_{\mathrm{p}}|^2 \tag{1.16}$$

$$\sigma_{\mathrm{abs,d}} = \sigma_{\mathrm{ext,d}} - \sigma_{\mathrm{scat,d}} = \frac{k_{\mathrm{m}}}{\varepsilon_{\mathrm{m}}} \Im\{\alpha_{\mathrm{p}}\} - \frac{k_{\mathrm{m}}^4}{6\pi\varepsilon_{\mathrm{m}}^2} |\alpha_{\mathrm{p}}|^2 \tag{1.17}$$

1.5.1 Optical forces

The time-averaged optical force experienced by a small particle when illuminated by time-varying electromagnetic field can be also expressed in terms of its polarisability [15]:

$$\langle \mathbf{F} \rangle_{\mathrm{DA}} = \frac{1}{2} \Re \left\{ \sum_i \alpha_{\mathrm{p}} E_i \nabla E_i^* \right\}. \tag{1.18}$$

where E_i are the electric field components. Starting from this expression, one can explicitly write the optical force in terms of extinction cross-section and particle's polarisability [51, 52]:

$$\langle \mathbf{F} \rangle_{\mathrm{DA}} = \frac{1}{4} \Re \left\{ \alpha_{\mathrm{p}} \right\} \nabla |\mathbf{E}|^2 + \frac{n_{\mathrm{m}}}{c} \sigma_{\mathrm{ext}} \langle \mathbf{S} \rangle - \frac{1}{2} c n_{\mathrm{m}} \sigma_{\mathrm{ext}} \nabla \times \langle \mathbf{s} \rangle \tag{1.19}$$

where $\langle \mathbf{S} \rangle = \frac{1}{2} \Re \{ \mathbf{E} \times \mathbf{H}^* \}$ is the time-averaged Poynting vector of the incoming wave and $\langle \mathbf{s} \rangle = i \frac{\varepsilon_{\mathrm{m}}}{2\omega} \mathbf{E} \times \mathbf{E}^*$ is the time-averaged spin angular momentum density [51, 52].

The first term in Eq. (1.19) represents the gradient force and is responsible for particle confinement in optical tweezers:

$$\mathbf{F}_{\mathrm{DA,grad}}(\mathbf{r}) = \frac{1}{2} \frac{n_{\mathrm{m}}}{c \varepsilon_{\mathrm{m}}} \Re \left\{ \alpha_{\mathrm{p}} \right\} \nabla I(\mathbf{r}) \tag{1.20}$$

where $I(\mathbf{r}) = \frac{1}{2} n_{\mathrm{m}} c |\mathbf{E}(\mathbf{r})|^2$ is the intensity of the electric field and $\mathbf{r}_{\mathrm{p}}$ is the position of the center of the dipole. The gradient force, arising from the potential energy of a dipole immersed in the electric field, is conservative and its work does not depend on the path taken. Particles with refractive index higher than that of the surrounding medium ($n_{\mathrm{p}} > n_{\mathrm{m}}$) have a positive $\Re \{ \alpha_{\mathrm{p}} \}$, and will be attracted toward the high intensity region of the optical field [4]. Conversely, when $n_{\mathrm{p}} < n_{\mathrm{m}}$ the polarisability is negative and the particles are repelled by the high intensity region.

The second term in Eq. (1.19) is the scattering force:

$$\mathbf{F}_{\mathrm{DA,scat}}(\mathbf{r}) = \frac{n_{\mathrm{m}}}{c} \sigma_{\mathrm{ext}} \langle \mathbf{S} \rangle = \frac{n_{\mathrm{m}}}{c} \sigma_{\mathrm{ext}} I(\mathbf{r}). \tag{1.21}$$

This term is responsible for the radiation pressure and is non-conservative. Note the dependence on the extinction cross-section because momentum transfer from the electromagnetic field to the particle is a result of both scattering and absorption processes. This force is directed along the propagation direction of the laser beam [2].

The last term in Eq. (1.19) is a spin-dependent force [51]:

$$\mathbf{F}_{\mathrm{DA,spin}}(\mathbf{r}) = -\frac{1}{2} c n_{\mathrm{m}} \sigma_{\mathrm{ext}} \nabla \times \langle \mathbf{s} \rangle. \tag{1.22}$$

This term is also non-conservative and dependent on the extinction cross-section. It can be generated by polarisation gradients in the electromagnetic
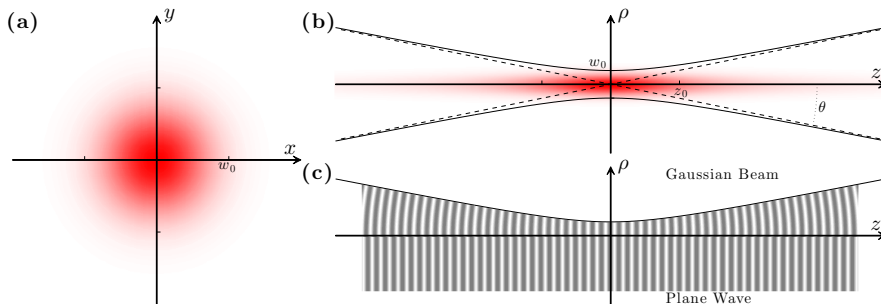
Figure 1.4: The intensity distribution of a Gaussian beam is (a) Gaussian in the transverse x, y plane and (b) cylindrically symmetric around the propagation z-axis. (c) As the beam propagates along the z-axis, its phase deviates (top) with respect to the one of a reference plane wave (bottom) leading to a phase shift of exactly π as z goes from $-\infty$ to $+\infty$ (Gouy phase shift). The shades of grey represent the phase of the beam from 0 to 2π. From Ref. [5].

field, but usually does not play a major role in optical trapping because it is zero or very small compared to the other contributions. However, it may play a more significant role when considering optical trapping with optical beams of higher order with inhomogeneous polarization patterns such as cylindrical vector beams [53, 54] or superpositions of circularly polarized Hermite-Gauss beams [55].

1.5.2 Gradient force with Gaussian beam

We now consider some examples that show the usefulness of the dipole approximation. Being a simple analytical approach it permits to obtain quantitative information on optical trapping (force components, trap stiffness) of small particles in many different beam configuration.

The first case is the single-beam trap configuration. We calculate the gradient force and the related trap stiffness of an incident laser beam with a typical Gaussian intensity profile which propagates along z axis [5] as in Fig. (1.4).

The complex electric field of a Gaussian beam $\mathbf{E}^{\mathrm{G}}(\rho, z)$ is [5]:

$$\mathbf{E}^{\mathrm{G}}(\rho, z) = \mathbf{E}_0 \frac{w_0}{w(z)} e^{-\frac{\rho^2}{w(z)^2}} e^{+ik_{\mathrm{m}}z - i\zeta(z) + ik_{\mathrm{m}}\frac{\rho^2}{2R(z)}} . \tag{1.23}$$

where ρ is the radial coordinate, $\mathbf{E}_0$ is a vector in xy plane specifying the amplitude, phase and polarisation of the beam, w_0 is the waist radius, $w(z)$ is the beam width such that $w(z) = w_0\sqrt{1 + \frac{z^2}{z_0^2}}$, $R(z)$ is the wavefront radius

17

$R(z) = z \left(1 + \frac{z_0^2}{z^2}\right)$, $\zeta(z)$ is phase correction $\zeta(z) = \operatorname{atan}\left(\frac{z}{z_0}\right)$ and z_0 is the Rayleigh range which denotes the distance from the beam waist at $z = 0$ to where the beam width has increased by a factor $\sqrt{2}$, $z_0 = \frac{k_\mathrm{m} w_0^2}{2}$. In the last equation the coordinate φ does not appear due to the cylindrical symmetry and the *paraxial approximation* has been used because the electromagnetic fields of a laser beam propagate mostly along a certain direction, which in this case along the z axis is assumed, spreading out only slowly in the transverse direction. Then the wave number along z axis can be approximate as follows:

$$k_{\mathrm{m},z} = k_\mathrm{m}\sqrt{1 - \frac{k_{\mathrm{m},x}^2 + k_{\mathrm{m},y}^2}{k_\mathrm{m}^2}} \approx k_\mathrm{m} - \frac{k_{\mathrm{m},x}^2 + k_{\mathrm{m},y}^2}{2k_\mathrm{m}} \ . \tag{1.24}$$

Thus, we can write the expression for the intensity of the beam:

$$\begin{aligned}
I^\mathrm{G}(\rho, z) &= \frac{1}{2}cn_\mathrm{m}|\mathbf{E}^\mathrm{G}(\rho, z)|^2 \\
&= \frac{1}{2}cn_\mathrm{m}|\mathbf{E}_0|^2 \frac{w_0^2}{w(z)^2} e^{-\frac{2\rho^2}{w(z)^2}} \\
&= I_0 \frac{w_0^2}{w(z)^2} e^{-\frac{2\rho^2}{w(z)^2}}
\end{aligned} \tag{1.25}$$

where $I_0 = \frac{1}{2}cn_\mathrm{m}|\mathbf{E}_0|^2$ is the maximum intensity at the center of the beam.

In the transverse plane $(z = 0)$, for small displacements from axis, we can approximate the intensity profile:

$$I^\mathrm{G}(\rho) \approx I_0 \left(1 - 2\frac{\rho^2}{w_0^2}\right) \tag{1.26}$$

so that the radial component of the gradient force [Eq. (1.20)] can be approximated by an elastic restoring force proportional and opposite to the displacement from the origin:

$$F_{\mathrm{DA,grad},\rho}^\mathrm{G} = -\kappa_\rho^\mathrm{G} \rho \tag{1.27}$$

in which the trap stiffness is:

$$\kappa_\rho^\mathrm{G} = 2\frac{\Re\{\alpha_\mathrm{p}\}}{cn_\mathrm{m}} \frac{I_0}{w_0^2}. \tag{1.28}$$

Similarly, we can calculate the force along z axis $(\rho = 0)$. Then for small displacements in the transverse plane:

$$I^{\mathrm{G}}(z) \approx I_0 \left(1 - \frac{z^2}{z_0^2} \right) \tag{1.29}$$

so that the z component of the gradient force [Eq. (1.20)]

$$F_{\mathrm{DA,grad},z}^{\mathrm{G}} = -\kappa_z^{\mathrm{G}} z \tag{1.30}$$

has spring constant:

$$\kappa_z^{\mathrm{G}} = \frac{\Re\{\alpha_{\mathrm{p}}\}}{c n_{\mathrm{m}}} \frac{I_0}{z_0^2}. \tag{1.31}$$

Eqs. (1.28 - 1.31) reveals that the spring constants are proportional to the electric field intensity maximum and the real part of the polarisability. Furthermore, these trap stiffness are inversely proportional to the beam area so, as may be expected, tighter focusing leads to stronger confinement.

1.5.3 Gradient force with counterpropagating Gaussian beams

A second important example is the situation of two counterpropagating gaussian beams. This is not only one of the first configuration used by Ashkin in his pioneering work [3], but a configuration often used in vacuum for the optical trapping and laser cooling of atoms and particles [8]. In liquid, this permits the trapping and optical binding of spherical and non-spherical particles with a wide tunability [56, 57]. Recent experiments in optomechanics with levitated particles also exploit this counterpropagating configuration [12, 58, 59].

Here, we show the calculation of the gradient force for a scheme of optical trap composed by two incident Gaussian beam which travel one opposite to the other along the z axis [60] and the two waste coincide with the origin of the laboratory reference system. Taking the expression of the Gaussian electric field [Eq. (1.23)] for this counterpropagating configuration, the intensity of stationary laser beam is:

$$I^{\mathrm{c.p.}}(\rho, z) = 4 I_0 \frac{w_0^2}{w(z)^2} e^{-\frac{2\rho^2}{w(z)^2}} \cos^2\left(k_{\mathrm{m}} z - \zeta(z) + k_m \frac{\rho^2}{2R(z)} \right) \tag{1.32}$$

In the transverse plane ($z = 0$), for small displacements from axis:

$$I^{\mathrm{c.p.}}(\rho) \approx 4 I_0 \left(1 - 2 \frac{\rho^2}{w_0^2} \right) \tag{1.33}$$

19

so that the radial component of the gradient force (1.20)

$$F_{\mathrm{DA,grad},\rho}^{\mathrm{c.p.}}(\rho) = -\kappa_\rho^{\mathrm{c.p.}}\rho \qquad (1.34)$$

in which the trap stiffness is:

$$\kappa_\rho^{\mathrm{c.p.}} = 8\frac{\Re\{\alpha_{\mathrm{p}}\}}{cn_{\mathrm{m}}}\frac{I_0}{w_0^2}. \qquad (1.35)$$

We note that this spring constant is four times greater than that associated with the Gaussian beam [Eq. (1.28)], demonstrating that stationary setup traps better than one single laser beam. Similarly, we can calculate the force along z axis ($\rho = 0$). Then for small displacements in the transverse plane we have:

$$I^{\mathrm{c.p.}}(z) \approx 4I_0\left[1 - \left(2 - 2k_{\mathrm{m}}z_0 + k_{\mathrm{m}}^2 z_0^2\right)\frac{z^2}{z_0^2}\right] \qquad (1.36)$$

so that the z component of the gradient force [Eq. (1.20)]

$$F_{\mathrm{DA,grad},z}^{\mathrm{c.p.}}(z) = -\kappa_z^{\mathrm{c.p.}}z \qquad (1.37)$$

with a spring constant:

$$\kappa_z^{\mathrm{c.p.}} = 4\frac{\Re\{\alpha_{\mathrm{p}}\}}{cn_{\mathrm{m}}}\left(2 - 2k_{\mathrm{m}}z_0 + k_{\mathrm{m}}^2 z_0^2\right)\frac{I_0}{z_0^2}. \qquad (1.38)$$

This result is more complex than the trap stiffness for a single Gaussian beam [Eq. (1.31)] and it depends also on the wavenumber k_{m}. Indeed, the generation of a stationary wave yield a modulation of intensity along the z-axis that result in a strong wavelength-dependent modulation of the axial optical force.

1.6 Classical and quantum optomechanics at the mesoscale

We conclude this chapter with a brief review of some quantum implications of optical forces at the mesoscale. In the last years, much effort has been devoted to developing techniques that bridge the gap between laser cooling of atomic species [8] and optical trapping of colloidal materials in order to study quantum phenomena at mesoscopic length scales. For this purpose, protocols for reaching the quantum regime at the mesoscale have been proposed for ground-state laser cooling of optically levitated nanoparticles [61, 62, 63]. The aim is to explore and exploit quantum effects, *e.g.*,
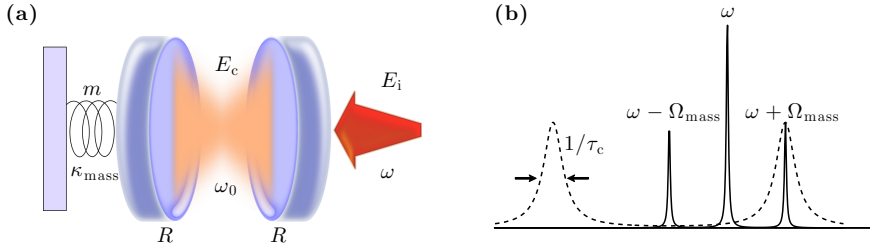
Figure 1.5: (a) A typical scheme of an optomechanical system is a cavity formed by a fixed mirror and a moving mirror and pumped by an incident field: a small displacement of the moving mirror changes the electromagnetic field present in the cavity and the field feeds back through its radiation force on the mirror position. (b) The mechanical oscillator modulates the pumping light (ω) producing two sidebands (Stokes sideband $\omega - \Omega_{\mathrm{mass}}$ and the anti-Stokes sideband $\omega + \Omega_{\mathrm{mass}}$). By detuning the input field on the red side of one of the cavity resonances (dashed line), the anti-Stokes sideband gets enhanced and, since anti-Stokes photons have more energy than the pumping field's ones, energy is extracted from the mechanical oscillator into the cavity field (optical cooling). For blue detuning, the Stokes sideband is enhanced and, thus, energy transferred from the field to the mechanical oscillator (optical amplification, not shown). Adapted from Ref. [5].

entanglement, quantum superposition of motional states and long quantum coherence, in systems much larger than atomic species. Here, we first review the general theoretical concepts of optomechanics, then we focus on some recent schemes for optomechanics with optically trapped particles in vacuum and their cooling towards their quantum motional ground state.

1.6.1 Classical cavity optomechanics

The first system where optical and mechanical degrees of freedom were coupled by radiation pressure was investigated by Braginskii and Manukin [64] in the context of experiments for the interferometric detection of gravitational waves [65]. They considered an optical cavity of length L with one fixed mirror and one moving mirror of mass m attached to a mechanical oscillator characterised by a stiffness κ_{mass}, as shown in Fig. (1.5a).

Transmission of light through the cavity occurs at resonance, *i.e.*, when $2L = q\lambda_q/n_{\mathrm{m}}$, where q is an integer, λ_q/n_{m} is the intracavity wavelength, n_{m} is the refractive index of the intracavity medium and λ_q is the wavelength of the cavity mode with frequency [5]:

$$\omega_q = q\frac{\pi c}{n_\mathrm{m} L} \ . \tag{1.39}$$

Now, suppose there is an incident field with (complex) amplitude E_i going into the cavity with a coupling constant K (K takes into account, *e.g.*, the losses due to the partial transmission into the cavity of the incoming field). Considering a frequency close to the fundamental resonance at ω_0, the dynamic equation for the cavity field $E_\mathrm{c}(t)$ can be derived from Helmholtz equation obtaining [66]:

$$\frac{dE_\mathrm{c}(t)}{dt} = \left[i(\omega - \omega_0) - \frac{1}{2\tau_\mathrm{c}}\right] E_\mathrm{c}(t) + KE_\mathrm{i} \ , \tag{1.40}$$

in which τ_c is the light intensity decay time that depends by the quality of the cavity [42]. A small displacement of the moving mirror, $x(t)$, from its equilibrium position at $x = 0$ changes the cavity length by $\Delta L(t) = x(t)$ and, hence, shifts the resonance frequency by

$$\Delta\omega_0(t) = -\omega_0\frac{x(t)}{L}. \tag{1.41}$$

Therefore, the intracavity field is coupled to the mirror displacement as

$$\frac{dE_\mathrm{c}(t)}{dt} = \left[i(\omega - \omega_0) + i\omega_0\frac{x(t)}{L} - \frac{1}{2\tau_\mathrm{c}}\right] E_\mathrm{c}(t) + KE_\mathrm{i}. \tag{1.42}$$

The mechanical motion of the moving mirror driven by the radiation pressure from the cavity field can be described by the Langevin equation for a damped noisy oscillator:

$$m\frac{d^2x(t)}{dt^2} + m\Gamma_\mathrm{mass}\frac{dx(t)}{dt} + m\Omega_\mathrm{mass}^2 x(t) = \chi(t) + F_\mathrm{rad}(t), \tag{1.43}$$

where Γ_mass is the mechanical damping coefficient, $\Omega_\mathrm{mass} = \sqrt{\kappa_\mathrm{mass}/m}$ is the oscillator characteristic frequency, $\chi(t) = W(t)\sqrt{2m\Gamma_\mathrm{mass}k_\mathrm{B}T}$ is a thermal noise, $W(t)$ is a white noise, $F_\mathrm{rad}(t) = 2\varepsilon_\mathrm{m}AR|E_\mathrm{c}(t)|^2$ is the radiation force on the mirror and A is the illumination area of the mirror.

Therefore, the dynamics of the optomechanical system is fully described by the two coupled Eqs. (1.41 - 1.43). Their solutions for $E_\mathrm{c}(t)$ and $x(t)$ depend on the parameters of the system, *e.g.*, the cavity resonance, the incident light intensity and frequency, and the cavity and oscillator loss terms. The dynamical back-action, *i.e.*, the fact that a displacement of the mirror feeds back on itself through radiation pressure, is clearly visible in the fact that $x(t)$ depends on $|E_\mathrm{c}(t)|^2$, which in turn is a function of $x(t)$. The radiation

force acting on the mirror yields a change in the damping term and in the oscillation frequency of the mirror so that Eq. (1.43) can be re-written as [67]:

$$\frac{d^2x(t)}{dt^2} + (\Gamma_{\text{mass}} + \Delta\Gamma_{\text{mass}})\frac{dx(t)}{dt} + (\Omega_{\text{mass}} + \Delta\Omega_{\text{mass}})^2 x(t) = \frac{\chi(t)}{m}, \quad (1.44)$$

with $\Delta\Gamma_{\text{mass}}$ and $\Delta\Omega_{\text{mass}}$ related with Stokes and anti-Stokes scattering. The vibration of the mirror modulates the driving field in two sidebands, as shown by the solid line in Fig. (1.5b). The optomechanical damping rate $\delta = \omega - \omega_0$ can be tuned to be positive (red detuning, $\delta < 0$), yielding effective cooling of the system, or negative (blue detuning, $\delta > 0$), yielding amplification of the mechanical oscillations. The optimum coupling occurs for $\delta = -(2\tau_c)^{-1}$ (cooling) and $\delta = +(2\tau_c)^{-1}$ (amplification). In the case of red detuning, the enhanced damping yields an effective cooling of the system and an effective temperature can be associated with the optomechanical Langevin equation [Eq. (1.44)], which can be written for $\Delta\Omega_{\text{mass}} \ll \Omega_{\text{mass}}$ as

$$T_{\text{eff}} \simeq T\frac{\Gamma_{\text{mass}}}{\Gamma_{\text{mass}} + \Delta\Gamma_{\text{mass}}}, \quad (1.45)$$

where T is the equilibrium absolute temperature in absence of radiation force and the above relation holds for $\tau_c\Delta\Gamma_{\text{mass}} \ll 1$ and for $T_{\text{eff}} > 2T\Gamma_{\text{mass}}/\Omega_{\text{mass}}$.

1.6.2 Quantum cavity optomechanics

The classical treatment of optomechanics does not pose any lower limit to the temperature achievable in the cooling process. However, the quantum nature of light and the discrete energy spectrum of the oscillator with states separated by $\hbar\Omega_{\text{mass}}$ and zero point fluctuation amplitude. The zero point fluctuation amplitude can be easily calculated by equating this zero point energy to the average energy of a classical oscillator. In fact, for a classical oscillator the average energy is double the average potential energy (from the virial theorem), hence $\langle E \rangle = m\Omega_{\text{mass}}^2\langle x^2 \rangle$. Thus, by posing $\langle E \rangle = E_0 = \hbar\Omega_{\text{mass}}/2$ the value of $x_0 = \sqrt{\langle x^2 \rangle} = \sqrt{\hbar/2m\Omega_{\text{mass}}}$ is found. Alternatively, one can use the expression of the position operator in terms of ladder operators, $\hat{x} = \sqrt{\frac{\hbar}{2m\Omega_{\text{mass}}}}(\hat{b} + \hat{b}^\dagger)$, and evaluate the positional fluctuations over the ground state, $x_0^2 = \langle \hat{x}^2 \rangle = \hbar/2m\Omega_{\text{mass}}$. $x_0 = \sqrt{\hbar/(2m\Omega_{\text{mass}})}$ need to be taken into account to evaluate the ultimate cooling temperature.

The quantum theory of optomechanical cooling [68, 69] starts by treating the optically driven cavity coupled to the mechanical oscillator as an open

quantum system. The total physical Hamiltonian is written in terms of the quantum ladder operators of the optical, $(\hat{a}, \hat{a}^\dagger)$, and mechanical, $(\hat{b}, \hat{b}^\dagger)$, quantum oscillators respectively [70], *i.e.*,

$$\hat{H} = -\hbar \, \delta \, \hat{a}^\dagger \hat{a} + \hbar \, \Omega_{\text{mass}} \, \hat{b}^\dagger \hat{b} + \hbar \, \eta \, \Omega_{\text{mass}} \, \hat{a}^\dagger \hat{a} (\hat{b}^\dagger + \hat{b}) + \hbar \, \frac{\Omega_{\text{R,i}}}{2} \, (\hat{a}^\dagger + \hat{a}) \, , \quad (1.46)$$

where $\Omega_{\text{R,i}} = 2\sqrt{P_{\text{i}} \Delta \omega_{\text{out}}/(\hbar \omega)}$ is the driving amplitude of the input radiation and $\eta = \omega_0 x_0 / \Omega_{\text{mass}} L$ is a dimensionless parameter characterising the optomechanical coupling via radiation pressure. The coupling is generally very small, *i.e.*, as small as $\eta \approx 10^{-4}$ for typical experimental conditions. This implies that the interaction between the mechanical oscillator and the electromagnetic fields can be treated pertubatively and, by the use of the generalised master equation [71] for the density matrix of the system and the adiabatic elimination of the fast rotating terms ($\propto e^{\pm i\omega t}$), it is possible to identify the light scattering contributions yielding the cooling and heating processes [68, 69]. The cooling process is based on scattering Stokes and anti-Stokes photons with rates that are weighted by the sidebands amplitudes:

$$A^{\mp} = \eta^2 \, \frac{4\Omega_{\text{R,i}}^2}{4\tau_{\text{c}}^2 \delta^2 + 1} \frac{\Omega_{\text{mass}}^2 \tau_{\text{c}}^3}{4\tau_{\text{c}}^2 (\delta \pm \Omega_{\text{mass}})^2 + 1}. \quad (1.47)$$

The balance between these two scattering processes yields the final mean thermal occupation number of the quantum-mechanical oscillator that is related to the ultimate temperature limit. Thus, including also the contribution from the thermal reservoir given by Eq. (1.45), the final occupation that can be achieved is [67]:

$$\bar{n}_{\text{f}} = \frac{A^+}{A^- - A^+} + \frac{\Gamma_{\text{mass}}}{\Gamma_{\text{mass}} + \Delta\Gamma_{\text{mass}}} \bar{n}_{\text{i}} \, , \quad (1.48)$$

where $\bar{n}_{\text{i}}$ is the initial occupancy at thermal equilibrium. The effective temperature limit is thus obtained as

$$T_{\text{eff}} = \bar{n}_{\text{f}} \frac{\hbar \Omega_{\text{mass}}}{k_{\text{B}}}. \quad (1.49)$$

In order to achieve ground state cooling of the mechanical oscillator, we need $\bar{n}_{\text{f}} < 1$ and hence $T_{\text{eff}} < \hbar\Omega_{\text{mass}}/k_{\text{B}}$, which, *e.g.*, for a 100 kHz oscillator leads to a temperature below $5 \, \mu$K. This regime is achieved in the resolved sideband cooling for which $\Omega_{\text{mass}}\tau_{\text{c}} \gg 1$ and $\bar{n}_{\text{f}} \approx (4\Omega_{\text{mass}}\tau_{\text{c}})^{-2}$ [72].

1.6.3 Laser cooling of optically trapped particles

Several schemes have been proposed to achieve optomechanical cooling of levitated particles [61, 62, 63]. In these schemes a particle is generally held in a high-finesse cavity in vacuum either by the cavity standing wave field [62] or by a separate optical tweezers [63, 73] [see the sketch in Fig. (1.6)]. The mechanical oscillator is then created by the effective confining potential of the optical tweezers with spring constant κ_{trap}, oscillator frequency $\omega_{\text{trap}} = \sqrt{\kappa_{\text{trap}}/m}$ and zero point fluctuation amplitude $x_0 = \sqrt{\hbar/(2m\omega_{\text{trap}})}$. A radiation field excites a cavity mode that couples to the trapped particle's centre-of-mass motion. Conversely, the presence of the dielectric particle in the cavity modifies the cavity mode yielding the position-dependent optomechanical coupling responsible for cooling.

In particular, the dielectric particle alters the cavity resonance through the change in refractive index occurring within the small particle volume, V, so that the cavity mode, $E_{\text{c}}(\mathbf{r})$, where $\mathbf{r}$ is position, is frequency-shifted by an amount [62, 73]

$$\Delta\omega_0 \approx -\frac{\omega_0}{2}\frac{\displaystyle\int_V \Delta\mathcal{P}(\mathbf{r})E_{\text{c}}(\mathbf{r})\ \mathrm{d}V}{\displaystyle\int_V \varepsilon_0|E_{\text{c}}(\mathbf{r})|^2\ \mathrm{d}V}\ , \tag{1.50}$$

where $\Delta\mathcal{P}(\mathbf{r})$ is the modification of the polarisation produced by the particle in the cavity. For a small particle, we can use the dipole approximation for the polarisability, so that $\Delta\mathcal{P}(\mathbf{r}) \approx \alpha_{\text{p}}E_{\text{c}}(\mathbf{r}_{\text{p}})\delta(\mathbf{r}_{\text{p}} - \mathbf{r})$, where α_{p} is the dipole polarisability and $\mathbf{r}_{\text{p}}$ is the centre-of-mass position of the particle. The zeroth-order contribution in the particle position yields a constant shift of the cavity resonance

$$\Delta\omega_0 \approx -\omega_0\frac{\alpha_{\text{p}}}{8\varepsilon_0 V_{\text{c}}}\ , \tag{1.51}$$

where V_{c} is the cavity volume. The first-order contribution in the particle position gives the optomechanical coupling characterized by the adimensional parameter

$$\eta \approx \frac{x_0}{\omega_{\text{trap}}}\frac{\omega_0^2\alpha_{\text{p}}}{4c\varepsilon_0 V_{\text{c}}}\ . \tag{1.52}$$

From the experimental point of view, optical trapping of particles has been recently achieved in vacuum as in the case of atoms, *i.e.*, in a chamber with a controllable vacuum pressure. In this case, the damping of the residual
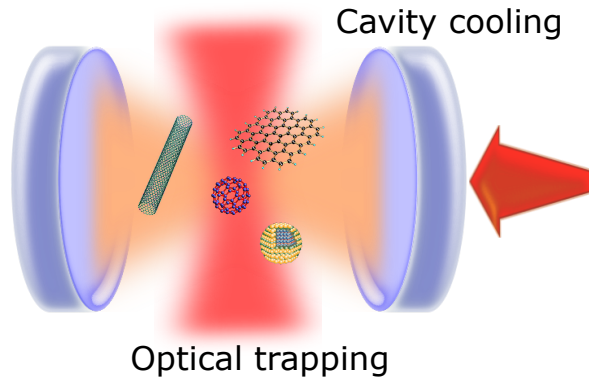
Figure 1.6: Optomechanics with optically trapped nanoparticles. Different schemes have been proposed to trap and cool nanoparticles in a high-finesse optical cavities. Nanostructures can be trapped by optical tweezers (red vertical beam), so that their centre-of-mass motion is confined by an effective harmonic potential with characteristic frequency ω_{trap}. The interaction with the cavity field (orange) generates an additional (dissipative) optical force cooling the particle motion to the trap ground-state. Adapted from Ref. [12].

gas is so low that the ballistic regime and harmonic oscillations can be easily observed in the trap.

For example, cavity cooling of nanoparticles particle has been demonstrated by Kiesel et al. [74], where a high finesse optical cavity has been used for both trapping and manipulation, demonstrating optomechanical control and laser cooling of the centre-of-mass motion of the particle (limited to 64 K because of the residual gas pressure). Instead, the scheme used by Li et al. [75] is based on a counterpropagating optical tweezers (in the near-infrared) to create a harmonic potential where to trap a silica microparticle and on pairs of additional counterpropagating beams (in the visible) to cool down its centre-of-mass motion. Laser cooling is achieved by an external feedback that adjusts the cooling beam power depending on the measured particle velocity so that the excess radiation pressure of one beam counteracts the motion of the particle. The result is an effective cooling that reaches temperatures in the millikelvin range. Similar feedback cooling schemes have been used by Gieseler et al. [76] that demonstrated laser cooling of a silica nanoparticle (70 nm radius) in a single-beam optical tweezers in vacuum. With this configuration, an effective temperature as low as about 50 mK was reached, as measured by observing residual thermal fluctuations.

Finally, we stress how the progress on the laser cooling of nanoparti-

cles, both spherical and non-spherical (nanowires, layered materials), is an on-going process with novel and exciting results obtained world-wide. For example, several experiments on nanowires (silicon, zinc oxide) are running in several laboratories (Vienna, Brno-Messina). In this context, having an accurate modeling, both at the classical and quantum level, on the optical forces and dynamics of non-spherical particles is of crucial importance to shed light on these complex systems.

Chapter 2

Full electromagnetic theory and T-matrix formalism

Here we present the Transition matrix formalism which has proved to be a very powerful approach to study light scattering by non spherical and non homogenous particles. The Transition matrix method gives an accurate solution to the problem, with no need to use approximations, and with a very satisfactory agreement with experimental results. The flexibility and elegance of the mathematical formalism together with the efficiency of the developed computational approach make the T-matrix a very good choice especially when dealing with light scattering by aggregated particles.

2.1 Introduction

As discussed in Chap. (1), when we study the light scattering process by non-spherical or non-homogenous particles with a size comparable with the light wavelength ($ka \simeq 1$), both the ray optics description [see Sect. (1.3)] and the dipole approximation [see Sect. (1.5)] are ruled out. A full electromagnetic theory based on the Maxwell equations has to be used [23]. However, the calculation can be complicated and different computational methods have been developed in the literature to handle the problem. In this chapter, after the description of the general equations related to optical forces and torques, within the framework of the electromagnetic scattering theory, we discuss the *T-matrix formalism*, *i.e.*, a method based on the multipole expansions of the electromagnetic fields [20]. The T-matrix is the matrix representation of a linear operator which, acting on the multipole amplitudes of the incident field, gives as a result the multipole amplitudes of the scattered field. When the scatterer is a homogeneous spherical particle, *i.e.*, in the highly
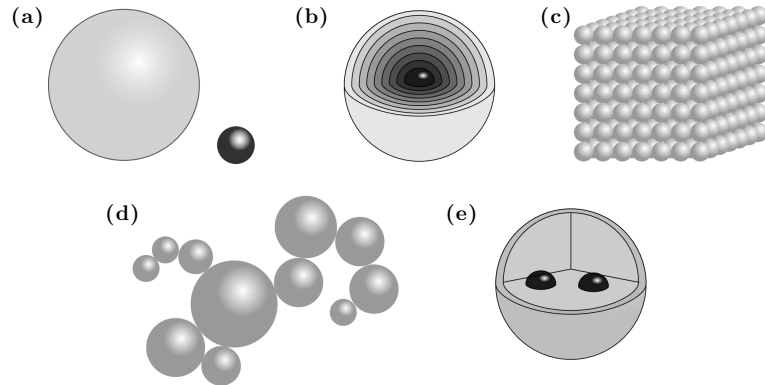
Figure 2.1: Complex non-spherical particles. A variety of computational methods are required to calculate the optical forces on objects other than (a) homogeneous spheres, such as (b) layered spheres, (c) cubes (here made of an array of spheres), (d) aggregates of spheres and (e) particles with inclusions of different materials. From Ref. [5].

symmetric case, the scattered field does not depend on the orientation of the particle and is exactly described by the Mie theory [22]. Anyway, the spherical model is not able to describe a great number of real scatterers, which, in general, may exhibit an asymmetric shape or may result from the aggregation of several constituent monomers. The introduction of asymmetry is immediately reflected in the polarization of the scattered field as well as in its dependence on the position and orientation of the particle. In such case, a model scatterer must be used which can simulate as accurately as possible the details of the structure of such composite particles. The T-matrix approach is particularly advantageous when we deal with particles composed by spherical constituents, *i.e.*, cluster or aggregates of spheres, spheres with spherical (eccentric) inclusions, and multilayered spheres [21], such as the ones shown in Fig. (2.1).

By varying the number of the constituent spheres (as well as of the layers of the inclusions), their refractive index and their mutual position, structures can be obtained which better approximate the shape and the composition of the scatterers in the analysed system. This technique takes into proper account the multiple scattering processes occurring among the spherical sub-units composing the aggregate and the contribution of all the details of the model structure. Optical properties of composite scatterers can be exactly calculated without introducing any approximation except the truncation of the expansion of the fields, being able to check the convergence of the results at every step.

The elements of the T-matrix contain all the information on the par-

ticle nature (refractive index, size relative to the wavelength, and shape) and on the orientation of the scatterer with respect to the incident field. A fundamental feature is that the T-matrix is independent of the propagation direction and polarization states of the incident and of the scattered fields. This means that, once we compute the T-matrix elements, we do not need to compute them again if the incident field direction and polarization state changes [23]. Borghese et al. [77] succeeded in showing that the transformation properties of the multipole fields under rotation of the coordinate frame imply corresponding transformation properties of the T-matrix elements under rotation of the scattering particle. Such transformation properties enable us to calculate orientational averages of the optical quantities of interest with a reasonable computational effort [21]. This is one of the greatest advantages offered by the T-matrix approach respect to other computational techniques like, for example, the discrete dipole approximation [41, 78]. Thanks to the flexibility and the accuracy of the T-matrix technique, we have the possibility to explore several systems and configurations in a broad range of fields of applications, going from interstellar dust modelling [24, 25] to the study of the behaviour of plasmon systems and finally to the optical trapping theory that we discuss in this thesis.

2.2 Maxwell stress tensor, radiation force, and torque

Particles illuminated by a radiation field experience a radiation force $\mathbf{F}_{\mathrm{rad}}$ and torque $\mathbf{T}_{\mathrm{rad}}$, which contribute to determining their dynamical behaviour. Since the interaction between radiation and matter is regulated by conservation laws, it is possible to derive $\mathbf{F}_{\mathrm{rad}}$ and $\mathbf{T}_{\mathrm{rad}}$ using the conservation of linear and angular momentum. So, the time-averaging optical force exerted by a monochromatic light on a particle is given by [21, 79, 80, 81]:

$$\mathbf{F}_{\mathrm{rad}} = \oint_S \hat{\mathbf{n}} \cdot \langle \mathsf{T}_{\mathrm{M}} \rangle \, \mathrm{d}S \tag{2.1}$$

where the integration is carried out over the surface S surrounding the scattering particle, $\hat{\mathbf{n}}$ is the outward normal unit vector, and $\langle \mathsf{T}_{\mathrm{M}} \rangle$ is the averaged *Maxwell stress tensor* which describes the mechanical interaction of light with matter. The general expression of the Maxwell stress tensor in a medium in the Minkowski form is:

$$\mathsf{T}_{\mathrm{M}} = \boldsymbol{\mathcal{E}} \otimes \boldsymbol{\mathcal{D}} + \boldsymbol{\mathcal{H}} \otimes \boldsymbol{\mathcal{B}} - \frac{1}{2} \left(\boldsymbol{\mathcal{E}} \cdot \boldsymbol{\mathcal{D}} + \boldsymbol{\mathcal{H}} \cdot \boldsymbol{\mathcal{B}} \right) \mathsf{I} . \tag{2.2}$$

31

where $\boldsymbol{\mathcal{E}}$ is the electric field, $\boldsymbol{\mathcal{D}}$ is the electric displacement, $\boldsymbol{\mathcal{H}}$ is the magnetic field, $\boldsymbol{\mathcal{B}}$ is the magnetic induction, $\otimes$ represents the dyadic product and I is the dyadic unit. Since we consider always harmonic fields, at angular frequency ω in a homogeneous, linear, and non-dispersive medium, we can simplify this expression by using the complex amplitudes of the fields, $\mathbf{E} = \mathbf{E}(\mathbf{r})$ and $\mathbf{B} = \mathbf{B}(\mathbf{r})$, so that, $i.e.$, the real physical electric field is written as $\boldsymbol{\mathcal{E}}(\mathbf{r}, t) = \Re\{\mathbf{E}(\mathbf{r})e^{-i\omega t}\}$ and in the same manner the real physical magnetic field [5]. Thus, the averaged Maxwell stress tensor simplifies as:

$$\langle\mathsf{T_M}\rangle = \frac{\varepsilon_{\mathrm{m}}}{2}\Re\left\{\mathbf{E}\otimes\mathbf{E}^* + \frac{c^2}{n_{\mathrm{m}}^2}\mathbf{B}\otimes\mathbf{B}^* - \frac{1}{2}\left(|\mathbf{E}|^2 + \frac{c^2}{n_{\mathrm{m}}^2}|\mathbf{B}|^2\right)\mathsf{I}\right\} \qquad (2.3)$$

where the fields, $\mathbf{E} = \mathbf{E}_{\mathrm{i}} + \mathbf{E}_{\mathrm{s}}$ and $\mathbf{B} = \mathbf{B}_{\mathrm{i}} + \mathbf{B}_{\mathrm{s}}$, are the total electric and magnetic fields, superposition of the incident $(\mathbf{E}_{\mathrm{i}}, \mathbf{B}_{\mathrm{i}})$ and scattered $(\mathbf{E}_{\mathrm{s}}, \mathbf{B}_{\mathrm{s}})$ fields.

In a similar way, considering the conservation of the angular momentum, the time averaged radiation torque is expressed as [21]:

$$\boldsymbol{\Gamma}_{\mathrm{rad}} = -\oint_S (\langle\mathsf{T_M}\rangle \times \mathbf{r}) \cdot \hat{\mathbf{n}}\, \mathrm{d}S \qquad (2.4)$$

where $\mathbf{r}$ is the vector position.

2.2.1 Angular momentum of light

In the previous part of this chapter we mentioned the conservation of angular momentum which leads to the definition of torque, given by Eq. (2.4). The total angular momentum $\mathbf{J}$ can be split in two contributions [82], in which $\mathbf{J}_{\mathrm{mech}}$ takes into account the mechanical effects on the scatterer while $\mathbf{J}_{\mathrm{field}}$ is the angular momentum of the field, that is [70]:

$$\mathbf{J}_{\mathrm{field}} = \frac{n_{\mathrm{m}}^2}{c^2}\int_V \mathbf{r} \times \boldsymbol{\mathcal{S}}\, \mathrm{d}V, \qquad (2.5)$$

where the term on the right-hand-side represents the flux of angular momentum that enters the surface S and $\frac{n_{\mathrm{m}}^2}{c^2}\boldsymbol{\mathcal{S}} = \varepsilon_{\mathrm{m}}\boldsymbol{\mathcal{E}} \times \boldsymbol{\mathcal{B}}$ is the Poynting's vector that is the energy flux density associated with a propagating wave. Using the Helmholtz decomposition of the electromagnetic fields and introducing respectively the scalar and the vector potentials ϕ and $\boldsymbol{\mathcal{A}}$ in the Coulomb gauge, the Eq. (2.5) can be rewritten as:

$$\mathbf{J}_{\mathrm{field}} = \varepsilon_{\mathrm{m}}\int_V \mathbf{r} \times \left[\boldsymbol{\mathcal{E}}_\parallel \times (\nabla \times \boldsymbol{\mathcal{A}}) + \boldsymbol{\mathcal{E}}_\perp \times (\nabla \times \boldsymbol{\mathcal{A}})\right]\, \mathrm{d}V, \qquad (2.6)$$

in which $\boldsymbol{\mathcal{E}}_\parallel$ is the irrotational component and $\boldsymbol{\mathcal{E}}_\perp$ is the rotational one of the electric field. The first term on the right-hand-side of Eq. (2.6) is related to the canonical angular momentum and is associated with the source term ϱ [5]:

$$\mathbf{J}_{\text{field,canonical}} = \varepsilon_{\text{m}} \int_V \mathbf{r} \times \left[\boldsymbol{\mathcal{E}}_\parallel \times (\nabla \times \boldsymbol{\mathcal{A}}) \right] \, dV = \varrho \int_V \mathbf{r} \times \boldsymbol{\mathcal{A}} \, dV. \qquad (2.7)$$

Therefore, in a source-free space or in the case of radiating fields rapidly vanishing at infinity, the canonical part of the electromagnetic angular momentum is negligible. The second term on the right-had-side of Eq. (2.6) is related to the rotational fields and can be further split into orbital and spin components:

$$\varepsilon_{\text{m}} \int_V \mathbf{r} \times [\boldsymbol{\mathcal{E}}_\perp \times (\nabla \times \boldsymbol{\mathcal{A}})] \, dV = \varepsilon_{\text{m}} \int_V \left[\sum_{j=x,y,z} \mathcal{E}_{\perp,j} (\mathbf{r} \times \nabla) \mathcal{A}_j \right] - \mathbf{r} \times (\boldsymbol{\mathcal{E}}_\perp \cdot \nabla) \boldsymbol{\mathcal{A}} \, dV \ . \qquad (2.8)$$

After other manipulations, the following expressions for the orbital, $\mathbf{L}$, and spin, $\mathbf{s}$, components of the light angular momentum can be obtained [82]:

$$\mathbf{L} = \varepsilon_{\text{m}} \int_V \sum_{j=x,y,z} \mathcal{E}_{\perp,j} (\mathbf{r} \times \nabla) \mathcal{A}_j \, dV \ , \qquad (2.9)$$

$$\mathbf{s} = \varepsilon_{\text{m}} \int_V \boldsymbol{\mathcal{E}}_\perp \times \boldsymbol{\mathcal{A}} \, dV \ . \qquad (2.10)$$

For a monochromatic transverse electromagnetic field, we can use the complex amplitudes of the field to express the electric field in terms of the vector potential, *i.e.*, $\mathbf{E} = \mathbf{E}_\perp = i\omega\mathbf{A}$. Thus, we can write the orbital, $\langle \mathbf{L}_{\text{d}} \rangle$, and spin, $\langle \mathbf{s}_{\text{d}} \rangle$, averaged angular momentum densities in a form that is useful in many practical cases:

$$\langle \mathbf{L}_{\text{d}} \rangle = i \frac{\varepsilon_{\text{m}}}{2\omega} \sum_{j=x,y,z} E_j (\mathbf{r} \times \nabla) E_j^* \qquad (2.11)$$

$$\langle \mathbf{s}_{\text{d}} \rangle = i \frac{\varepsilon_{\text{m}}}{2\omega} \mathbf{E} \times \mathbf{E}^* \ . \qquad (2.12)$$
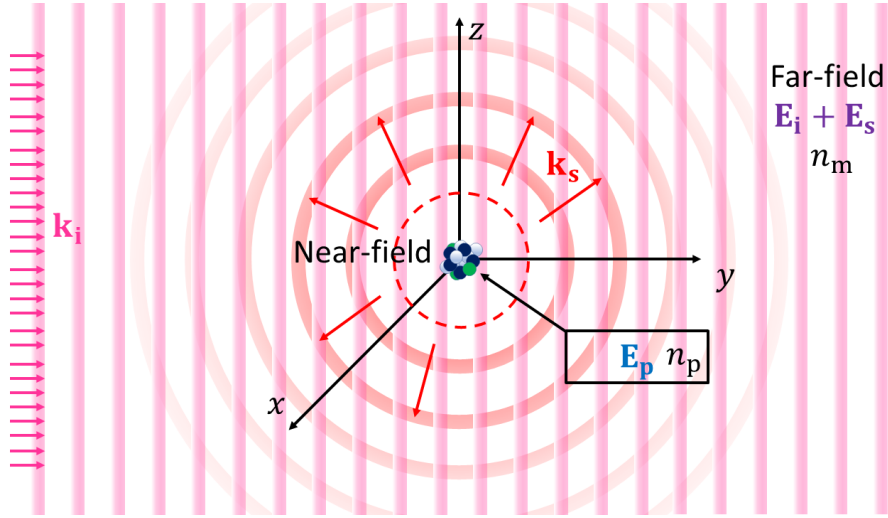
33

Figure 2.2: Pictorial view of a scattering process. Scattering theory studies how an incoming electromagnetic wave is scattered by a particle. In general, when light impinges on an object, the latter emits a scattered electromagnetic field, which in the far-field is a spherical wave. In particular, given an incoming linearly polarised plane electromagnetic wave ($\mathbf{E}_\mathrm{i}$) in a medium of refractive index n_m impinging on a particle of homogeneous refractive index n_p, one wants to determine the electromagnetic field inside the particle ($\mathbf{E}_\mathrm{p}$) and the scattered electromagnetic field ($\mathbf{E}_\mathrm{s}$), both in the near-field and in the far-field.

2.3   The scattering problem

In order to calculate radiation forces and torques acting on a particle through Eqs. (2.1 - 2.4), it is necessary to solve the scattering problem aiming at describing the electromagnetic fields scattered by a particle when it is illuminated by an incoming electromagnetic wave. In Fig. (2.2) we represent a pictorial view of a scattering process.

For a homogeneous particle of refractive index n_p in a medium of refractive index n_m, the three-dimensional homogeneous Helmholtz equations describe the scattering process:

$$\begin{cases} \left(\nabla^2 + k_\mathrm{m}^2\right)\mathbf{E}_\mathrm{i}(\mathbf{r}) &= \mathbf{0} \\ \left(\nabla^2 + k_\mathrm{m}^2\right)\mathbf{E}_\mathrm{s}(\mathbf{r}) &= \mathbf{0} \\ \left(\nabla^2 + k_\mathrm{p}^2\right)\mathbf{E}_\mathrm{p}(\mathbf{r}) &= \mathbf{0} \end{cases}, \qquad (2.13)$$

where $\mathbf{E}_\mathrm{i}(\mathbf{r})$ is the incident electric field, $\mathbf{E}_\mathrm{s}(\mathbf{r})$ is the scattered electric field, so that the total electric field outside the particle is $\mathbf{E}_\mathrm{t}(\mathbf{r}) = \mathbf{E}_\mathrm{i}(\mathbf{r}) + \mathbf{E}_\mathrm{s}(\mathbf{r})$,

$\mathbf{E}_p(\mathbf{r})$ is the total electric field inside the particle, $k_m = n_m k_0$, $k_p = n_p k_0$ and k_0 is the vacuum wavenumber. To derive the vector solutions of the previous equations, it is advisable to introduce a spherical coordinate system (r, ϑ, φ) and a scalar function $F(r, \vartheta, \varphi)$, solution of the scalar Helmholtz equation:

$$(\nabla^2 + k^2) F(r, \vartheta, \varphi) = 0. \tag{2.14}$$

The most general solution of the Helmholtz equation that is regular at the origin is:

$$F_j(\mathbf{r}) = \sum_{l=0}^{+\infty} \sum_{m=-l}^{+l} B_{lm} \, j_l(kr) \, Y_{lm}(\hat{\mathbf{r}}) \tag{2.15}$$

and the general solution that satisfies the radiation condition at infinity is

$$F_h(\mathbf{r}) = \sum_{l=0}^{+\infty} \sum_{m=-l}^{+l} C_{lm} \, h_l(kr) \, Y_{lm}(\hat{\mathbf{r}}) \,, \tag{2.16}$$

where B_{lm} and C_{lm} are the amplitudes corresponding to each mode, $j_l(kr)$ and $h_l(kr)$ are respectively the Bessel and the Hankel functions, $Y_{lm}(\hat{\mathbf{r}})$ are the spherical harmonics and l is a natural number. The electromagnetic fields outside and inside the particle are related by the boundary conditions across the surface of the particle.

2.3.1 Cross sections

Since any electromagnetic field can be described as a superpositions of plane waves and Maxwell's equations are linear, it suffices to consider the scattering produced by a single linearly polarised incoming homogeneous plane wave [5]:

$$\mathbf{E}_i(\mathbf{r}) = E_0 e^{i\mathbf{k}_i \cdot \mathbf{r}} \hat{\mathbf{e}}_i, \tag{2.17}$$

where $\hat{\mathbf{e}}_i$ is the unit vector indicating the polarisation direction and $\mathbf{k}_i = k_m \hat{\mathbf{k}}_i$ is the real wavevector along the incidence propagation direction. $\mathbf{E}_s(\mathbf{r}) = [E_{s,x}(\mathbf{r}), E_{s,y}(\mathbf{r}), E_{s,z}(\mathbf{r})]$ satisfies the vector Helmholtz equation and its Cartesian components must satisfy the scalar Helmholtz equation. The solution to this equation satisfies the radiation condition at infinity [83, 84], *i.e.*, for the x-component:

$$E_{s,x}(\mathbf{r}) = E_{s,x}(r, \hat{\mathbf{k}}_s) = \sum_{lm} h_l(k_m r) C_{lm,x}(\hat{\mathbf{k}}_i) \, Y_{lm}(\hat{\mathbf{k}}_s), \tag{2.18}$$

where $\hat{\mathbf{k}}_\mathrm{s}$ is the radial unit vector indicating the direction of the scattered wave, $\mathbf{r} = r\hat{\mathbf{k}}_\mathrm{s}$ and the amplitudes $C_{lm,x}(\hat{\mathbf{k}}_\mathrm{i})$, which depend on the direction of the incident wave, are determined by the boundary conditions at the surface of the particle.

Using the asymptotic properties of $h_l(k_\mathrm{m}r)$ for $k_\mathrm{m}r \to \infty$, the asymptotic form of $E_{\mathrm{s},x}(\mathbf{r})$ can be written as a spherical wave

$$E_{\mathrm{s},x}(\mathbf{r}) = E_0 \, \frac{e^{ik_\mathrm{m}r}}{r} \, f_x(\hat{\mathbf{k}}_\mathrm{s}, \hat{\mathbf{k}}_\mathrm{i}) \,, \tag{2.19}$$

where the x-component of the normalised scattering amplitude has been introduced as

$$f_x(\hat{\mathbf{k}}_\mathrm{s}, \hat{\mathbf{k}}_\mathrm{i}) = k_\mathrm{m}^{-1} \sum_{lm} (-i)^{l+1} C_{lm,x}(\hat{\mathbf{k}}_\mathrm{i}) \, Y_{lm}(\hat{\mathbf{k}}_\mathrm{s}) \,. \tag{2.20}$$

Repeating the same procedure on $E_{\mathrm{s},y}(\mathbf{r})$ and $E_{\mathrm{s},z}(\mathbf{r})$, the normalised scattering amplitude $\mathbf{f}(\hat{\mathbf{k}}_\mathrm{s}, \hat{\mathbf{k}}_\mathrm{i}) = \left[f_x(\hat{\mathbf{k}}_\mathrm{s}, \hat{\mathbf{k}}_\mathrm{i}),\ f_y(\hat{\mathbf{k}}_\mathrm{s}, \hat{\mathbf{k}}_\mathrm{i}),\ f_z(\hat{\mathbf{k}}_\mathrm{s}, \hat{\mathbf{k}}_\mathrm{i}) \right]$ and the asymptotic form of the scattered field can be obtained and

$$\mathbf{E}_\mathrm{s}(\mathbf{r}) = \mathbf{E}_\mathrm{s}(r, \hat{\mathbf{k}}_\mathrm{s}) = E_0 \, \mathbf{f}(\hat{\mathbf{k}}_\mathrm{s}, \hat{\mathbf{k}}_\mathrm{i}) \, \frac{e^{ik_\mathrm{m}r}}{r} \,. \tag{2.21}$$

As known, from the scattering amplitude $\mathbf{f}(\hat{\mathbf{k}}_\mathrm{s}, \hat{\mathbf{k}}_\mathrm{i})$ it is possible to derive all the other optical properties such as the scattering cross-section σ_scat (taking the square modulus of the scattering amplitude and integrating over the solid angle), the extinction cross-section σ_ext thanks to the optical theorem, and finally the absorption cross-section σ_abs. The asymmetry of the scattering with respect to the incoming wave direction and polarisation can be quantified by the asymmetry parameters and, in particular, by the asymmetry parameter in the direction of the incoming wave defined as

$$g_\mathrm{i} = \frac{1}{\sigma_\mathrm{scat}} \oint_\Omega \frac{\mathrm{d}\sigma_\mathrm{scat}}{\mathrm{d}\Omega} \hat{\mathbf{r}} \cdot \hat{\mathbf{k}}_\mathrm{i} \, \mathrm{d}\Omega \tag{2.22}$$

and the transverse asymmetry parameters defined as

$$g_1 = \frac{1}{\sigma_\mathrm{scat}} \oint_\Omega \frac{\mathrm{d}\sigma_\mathrm{scat}}{\mathrm{d}\Omega} \hat{\mathbf{r}} \cdot \hat{\mathbf{u}}_1 \, \mathrm{d}\Omega \tag{2.23}$$

and

$$g_2 = \frac{1}{\sigma_\mathrm{scat}} \oint_\Omega \frac{\mathrm{d}\sigma_\mathrm{scat}}{\mathrm{d}\Omega} \hat{\mathbf{r}} \cdot \hat{\mathbf{u}}_2 \, \mathrm{d}\Omega \,, \tag{2.24}$$

where $\hat{\mathbf{u}}_1 = \hat{\mathbf{e}}_i$ and $\hat{\mathbf{u}}_2 = \hat{\mathbf{k}}_i \times \hat{\mathbf{e}}_i$. It is often convenient to characterize a scattering particle through efficiencies that are defined by the ratios:

$$Q_{\text{scat}} = \frac{\sigma_{\text{scat}}}{\sigma_{\text{geom}}} \, , Q_{\text{ext}} = \frac{\sigma_{\text{ext}}}{\sigma_{\text{geom}}} \, , Q_{\text{abs}} = \frac{\sigma_{\text{abs}}}{\sigma_{\text{geom}}}. \tag{2.25}$$

in which, σ_{geom} is the geometrical cross section of the particle in a plane orthogonal to the direction of incidence. Another quantity that characterizes the optical properties of a particle is the albedo that is defined as

$$\bar{\omega} = \frac{\sigma_{\text{scat}}}{\sigma_{\text{ext}}} = \frac{Q_{\text{scat}}}{Q_{\text{geom}}}. \tag{2.26}$$

The albedo, when considered in terms of photons impinging on a particle, gives the probability that a photon be scattered rather than absorbed [85].

2.3.2 Multipole expansion of a plane wave

Let us consider a homogeneous electromagnetic plane wave where planes of equal phase and of equal amplitude are mutually parallel to each other [Eq. (2.17)]. Since it is finite at the origin, it can be decomposed in **J**-multipoles whose radial function is a spherical Bessel function $j_l(kr)$ to ensure the finiteness at the origin:

$$\mathbf{E}_i(r, \hat{\mathbf{r}}) = E_0 \sum_{p=1,2} \sum_{lm} W_{i,lm}^{(p)}(\hat{\mathbf{e}}_i, \hat{\mathbf{k}}_i) \mathbf{J}_{lm}^{(p)}(kr, \hat{\mathbf{r}}). \tag{2.27}$$

In this equation the scalar spherical harmonics $Y_{lm}(\hat{\mathbf{r}})$ are been extended in the *radial vector orthonormal spherical harmonic* $\mathbf{Y}_{lm}(\hat{\mathbf{r}})$ and in the *transversal vector orthonormal spherical harmonic* $\mathbf{Z}_{lm}^{(1)}(\hat{\mathbf{r}})$ and $\mathbf{Z}_{lm}^{(2)}(\hat{\mathbf{r}})$ to deal with vector fields. So they are defined as [21]:

$$\begin{cases} \mathbf{Y}_{lm}(\hat{\mathbf{r}}) & = & Y_{lm}(\hat{\mathbf{r}})\hat{\mathbf{r}} \\ \mathbf{Z}_{lm}^{(1)}(\hat{\mathbf{r}}) & = & -\dfrac{i}{\sqrt{l(l+1)}} \, \hat{\mathbf{r}} \times \nabla Y_{lm}(\hat{\mathbf{r}}) \\ \mathbf{Z}_{lm}^{(2)}(\hat{\mathbf{r}}) & = & \mathbf{Z}_{lm}^{(1)}(\hat{\mathbf{r}}) \times \hat{\mathbf{r}} \end{cases} . \tag{2.28}$$

Then:

$$\begin{aligned} W_{i,lm}^{(1)} & = & 4\pi i^l \, \hat{\mathbf{e}}_i \cdot \mathbf{Z}_{lm}^{(1)*}(\hat{\mathbf{k}}_i) \\ \\ W_{i,lm}^{(2)} & = & 4\pi i^{l+1} \, \hat{\mathbf{e}}_i \cdot \mathbf{Z}_{lm}^{(2)*}(\hat{\mathbf{k}}_i) \end{aligned} \tag{2.29}$$

are numerical coefficients referred to the multipolar components of magnetic ($p = 1$) and electric ($p = 2$) fields [86]. In analogy to incoming field, the scattered wave is expanded in **H**-multipoles, whose radial function is a spherical Hankel function $h_{(1),l}(kr)$ of the first kind because the scattered field has to satisfy the radiation condition at infinity [84]:

$$\mathbf{E}_{\mathrm{s}}(r, \hat{\mathbf{r}}) = E_0 \sum_{p=1,2} \sum_{lm} A_{\mathrm{s},lm}^{(p)}(\hat{\mathbf{e}}_{\mathrm{i}}, \hat{\mathbf{k}}_{\mathrm{i}}) \mathbf{H}_{lm}^{(p)}(k_{\mathrm{m}} r, \hat{\mathbf{r}}), \tag{2.30}$$

where $A_{\mathrm{s},lm}^{(1)}$ and $A_{\mathrm{s},lm}^{(2)}$ are the amplitudes of the magnetic and electrical scattered fields respectively which are determined by the boundary conditions across the surface of the particle. In general, they depend on the orientation of the scattering particle with respect to the incident field. The multipole expansion of the normalized scattering amplitude is easily obtained by taking the limit of the **H**-multipole fields for $kr \to \infty$ [21]. Then, the asymptotic form of the scattered field is:

$$\mathbf{E}_{\mathrm{s}}(r, \hat{\mathbf{k}}_{\mathrm{s}}) = E_0 \frac{e^{ik_{\mathrm{m}} r}}{k_{\mathrm{m}} r} \sum_{plm} (-i)^{l+p} A_{\mathrm{s},lm}^{(p)}(\hat{\mathbf{e}}_{\mathrm{i}}, \hat{\mathbf{k}}_{\mathrm{i}}) \mathbf{Z}_{lm}^{(p)}(\hat{\mathbf{k}}_{\mathrm{s}}). \tag{2.31}$$

The comparison with Eq. (2.21) yields

$$\mathbf{f}(\hat{\mathbf{k}}_{\mathrm{s}}, \hat{\mathbf{k}}_{\mathrm{i}}) = \frac{1}{k_{\mathrm{m}}} \sum_{plm} (-i)^{l+p} A_{\mathrm{s},lm}^{(p)}(\hat{\mathbf{u}}_{\mathrm{i},\eta}, \hat{\mathbf{k}}_{\mathrm{i}}) \mathbf{Z}_{lm}^{(p)}(\hat{\mathbf{k}}_{\mathrm{s}}), \tag{2.32}$$

in which the temporary argument $\hat{\mathbf{e}}_{\mathrm{i}}$ has been substituted by the label η that recalls the polarization of the incident field. Therefore the normalized scattering amplitude matrix elements on the basis $\hat{\mathbf{u}}_{\mathrm{s},\eta'}$ of the scattered field is:

$$f_{\eta'\eta} = -\frac{i}{4\pi k_{\mathrm{m}}} \sum_{plm} W_{\mathrm{i},lm}^{(p)*}(\hat{\mathbf{u}}_{\mathrm{s},\eta'}, \hat{\mathbf{k}}_{\mathrm{s}}) A_{\mathrm{s},lm}^{(p)}(\hat{\mathbf{u}}_{\mathrm{i},\eta}, \hat{\mathbf{k}}_{\mathrm{i}}). \tag{2.33}$$

At this stage, the explicit expressions of the scattering and the extinction cross section of a particle can be written in terms of the amplitudes of the fields. Taking the square modulus of Eq. (2.32) and operating the integral over the entire solid angle, the scattering cross section is:

$$\sigma_{\mathrm{scat}} = \frac{1}{k_{\mathrm{m}}^2} \sum_{plm} A_{\mathrm{s},lm}^{(p)*}(\hat{\mathbf{e}}_{\mathrm{i}}, \hat{\mathbf{k}}_{\mathrm{i}}) A_{\mathrm{s},lm}^{(p)}(\hat{\mathbf{e}}_{\mathrm{i}}, \hat{\mathbf{k}}_{\mathrm{i}}). \tag{2.34}$$

The extinction cross section is related to the scattering amplitude through the optical theorem, then:

$$\sigma_{\text{ext}} = -\frac{1}{k_{\text{m}}^2} \Re \left\{ \sum_{plm} W_{\text{i},lm}^{(p)*}(\hat{\mathbf{e}}_{\text{i}}, \hat{\mathbf{k}}_{\text{i}}) A_{\text{s},lm}^{(p)}(\hat{\mathbf{e}}_{\text{i}}, \hat{\mathbf{k}}_{\text{i}}) \right\} \qquad (2.35)$$

2.4   T-matrix

The transition matrix, or T-matrix, formalism was derived by Waterman [20] starting from the integral equation formulation of electromagnetic scattering to solve the scattering problem. The T-matrix was calculated by expanding the field into a series of spherical multipole fields and by imposing boundary conditions across the surface of the particles. This formulation of the T-matrix method, which is known as extended boundary condition method (EBCM), can then be regarded as a generalisation of Mie theory which is the paradigmatic solution of the light scattering problem obtained by Gustav Mie for a homogeneous sphere of arbitrary size. While, as we have seen, the analytical approach of the multipole expansion is relatively simple and general, the computational methods needed to calculate the expansion coefficients from the imposition of the boundary conditions can be quite complex [23]. The formulation used hereinafter is provided by Ferdinando Borghese and coworkers and shows the advantage that most calculations are carried out analytically and the resulting algorithms are, therefore, computationally efficient and accurate.

Because of the linearity of Maxwell's equations and of the boundary conditions, the scattering process can be considered as a linear operator $\mathbb{T}$ (*transition operator*) so that

$$\mathbf{E}_{\text{s}} = \mathbb{T}\mathbf{E}_{\text{i}} , \qquad (2.36)$$

with $\mathbf{E}_{\text{i}}$ the incoming electric field and $\mathbf{E}_{\text{s}}$ the scattered electric field. Therefore, if both $\mathbf{E}_{\text{i}}$ and $\mathbf{E}_{\text{s}}$ are expanded on suitable bases (not necessarily the same), it is possible to find a transition matrix $\mathbb{T}$ that relates the coefficients of such expansions, encompassing all the information on the morphology and orientation of the particle with respect to the incident field [20]. Since $\mathbf{E}_{\text{i}}$ is in general finite at the origin, its expansion is conveniently given in terms of **J**-multipoles [Eq. (2.27)] with amplitudes $W_{\text{i},lm}^{(p)}$ [Eq. (2.29)]. Since $\mathbf{E}_{\text{s}}$ must satisfy the radiation condition at infinity, it is convenient to expand it in terms of **H**-multipoles [Eq. (2.30)] with amplitudes $A_{\text{s},lm}^{(p)}$. These amplitudes are determined by imposing the boundary conditions across the surface of the scattering particle. The transition matrix $\mathbb{T} = \{T_{l'm'lm}^{(p'p)}\}$ of the scattering particle acts on the known multipole amplitudes of the incident field $W_{\text{i},lm}^{(p)}$

to give the unknown amplitudes of the scattered field $A_{\mathrm{s},l'm'}^{(p')}$, *i.e.*,

$$A_{\mathrm{s},l'm'}^{(p')}(\hat{\mathbf{e}}_{\mathrm{i}}, \hat{\mathbf{k}}_{\mathrm{i}}) = \sum_{plm} T_{l'm'lm}^{(p'p)} \, W_{\mathrm{i},lm}^{(p)}(\hat{\mathbf{e}}_{\mathrm{i}}, \hat{\mathbf{k}}_{\mathrm{i}}) \ . \qquad (2.37)$$

The quantities $T_{l'm'lm}^{(p'p)}$ take into account the morphology of the particle as well as the boundary conditions, but are independent of the state of polarization of the incident field. Therefore, Eq. (2.37) holds true whatever the polarization is. For instance, the equation

$$A_{\mathrm{s},\eta l'm'}^{(p')} = \sum_{plm} T_{l'm'lm}^{(p'p)} \, W_{\mathrm{i},\eta lm}^{(p)} \qquad (2.38)$$

relates the basis-polarized amplitudes of the incident and of the scattered field. Then, substituting Eq. (2.38) into Eq. (2.33), the explicit relation between the scattering amplitude and the T-matrix can be obtained:

$$f_{\eta'\eta} = -\frac{i}{4\pi k_{\mathrm{m}}} \sum_{plm} \sum_{p'l'm'} W_{\mathrm{s},\eta'lm}^{(p)*} T_{l'm'lm}^{(p'p)} W_{\mathrm{i},\eta l'm'}^{(p')}. \qquad (2.39)$$

This equation, giving the explicit relation between the scattering amplitude and the Transition matrix, is perhaps the most important equation in the theory of light scattering. In fact, the observable quantities, such as the optical cross sections of the particles, are given in terms of the scattering amplitude matrix elements, and so can be easily computed once the T-matrix elements are known.

2.5 Applications to model particles

The T-matrix method can be used to rigorously describe light scattering by many particle models, specifically, homogeneous spheres, first described by Gustav Mie [22], radially non-homogeneous spheres, which is an extension of Mie theory to spheres where the refractive index is a regular function of the distance from the center [87], and aggregates or cluster of spheres, where the T-matrix approach proves to be a very powerful approach.

2.5.1 Mie theory

A milestone result in electromagnetic scattering theory is the complete solution to the problem of light scattering of a linearly polarised plane wave by a homogeneous sphere of arbitrary radius a and refractive index n_{p} surrounded by a medium of refractive index n_{m} [22]. This result was obtained

by Gustav Mie in 1908 and is therefore known as *Mie theory*. If the material of the sphere and that of the surrounding medium are nonmagnetic, the boundary conditions reduce to the requirement of continuity of the tangential components of both the electric and magnetic fields, where the latter is related to the electric components by the rotor operator. The relations between the amplitudes of the scattered and of the incident fields represent the Mie coefficients, which are defined as:

$$a_l = -\frac{A^{(2)}_{\mathrm{s},lm}}{W^{(2)}_{\mathrm{i},lm}}$$

$$b_l = -\frac{A^{(1)}_{\mathrm{s},lm}}{W^{(1)}_{\mathrm{i},lm}}. \qquad (2.40)$$

Mie coefficients are used to calculate the exact expressions of the scattered electrical and magnetic fields and, imposing the appropriate boundary conditions, they are:

$$a_l = \frac{n_{\mathrm{m}}u'_l(\rho_{\mathrm{p}})u_l(\rho_{\mathrm{m}}) - n_{\mathrm{p}}u_l(\rho_{\mathrm{p}})u'_l(\rho_{\mathrm{m}})}{n_{\mathrm{m}}u'_l(\rho_{\mathrm{p}})w_l(\rho_{\mathrm{m}}) - n_{\mathrm{p}}u_l(\rho_{\mathrm{p}})w'_l(\rho_{\mathrm{m}})} \qquad (2.41)$$

$$b_l = \frac{n_{\mathrm{p}}u'_l(\rho_{\mathrm{p}})u_l(\rho_{\mathrm{m}}) - n_{\mathrm{m}}u_l(\rho_{\mathrm{p}})u'_l(\rho_{\mathrm{m}})}{n_{\mathrm{p}}u'_l(\rho_{\mathrm{p}})w_l(\rho_{\mathrm{m}}) - n_{\mathrm{m}}u_l(\rho_{\mathrm{p}})w'_l(\rho_{\mathrm{m}})} \qquad (2.42)$$

where $u_l(\rho) = \rho j_l(\rho)$ and $w_l(\rho) = \rho h_l(\rho)$ are Riccati-Bessel and Riccati-Hankel functions, respectively [88], while the prime denotes derivation with respect to the argument, $\rho_{\mathrm{m}} = n_{\mathrm{m}}k_0 a$ and $\rho_{\mathrm{p}} = n_{\mathrm{p}}k_0 a$. Thus, the scattering problem is reduced to the calculations of these coefficients through, *e.g.*, the imposition of the boundary conditions across the particle surface or by point matching numerically the fields at the surface [21]. The T-matrix formalism for a spherical scatterer provides the Mie coefficients. The T-matrix for a homogenous spherical particle is diagonal, independent of m and connected to the Mie coefficients a_l and b_l , *i.e.*,

$$\mathbf{A}_{\mathrm{s}} = -\mathbb{R}\mathbf{W}_{\mathrm{i}} , \qquad (2.43)$$

where $\mathbb{R} = \{-T^{(p'p)}_{l'm'lm}\} = \{R^{(p'p)}_{l'm'lm}\}$ [85] and

$$R^{(p'p)}_{l'm'lm} = \begin{cases} b_l & p = p' = 1 \text{ and } l = l' \text{ and } m = m' \\ a_l & p = p' = 2 \text{ and } l = l' \text{ and } m = m' \\ 0 & \text{otherwise} \end{cases} \qquad (2.44)$$

Moreover, according to Eq. (2.39) and Eq. (2.43) the scattering amplitude has the form:

$$f_{\eta'\eta} = \frac{i}{4\pi k_{\mathrm{m}}} \sum_{plm} W^{(p)*}_{\mathrm{s},\eta lm} R^{(p)}_l W^{(p)}_{\mathrm{i},\eta'lm}. \qquad (2.45)$$

It is actually diagonal in η on account of the reciprocity theorem and the diagonal elements $f_{\eta'\eta}$ are complex numbers with a different phase, so that the scattered wave may turn out to be elliptically polarized even when the incident wave is linearly polarized. To get an accurate representation of the scattered field, the sum in Eq. (2.45) must be extended to a sufficiently high value of l, say l_M. In other words, the convergence of the calculation must always be checked [21]. To get a fair convergence for a sphere of size parameter x, it is necessary to include into Eq. (2.45) terms up to $l_M > x$ [83]. In practice, when $x \leq 0.1$ one needs to include terms up to $l_M = 1$ or, at most, up to $l_M = 2$ only. For smaller values of x, one can expand the elements of the T-matrix in powers of x, thus obtaining the Rayleigh scattering approximation that assumes the scattered field from a small sphere is well approximated by the field of the dipole moment induced by the incident electromagnetic wave [85]. However, the elements of the T-matrix as well as the convergence of the scattered field depend not only on the size parameter but also on the refractive index n_{p} (that is contained in ρ_{p}). Therefore, as long as the refractive indexes are frequency independent, the response of a spherical scatterer does not depend separately on a and λ, but rather on their ratio. This is the principle of optical scaling that allows the experimentalists to test the reliability of the theoretical predictions using microwave devices and large scale scatterers [89].

2.5.2 Aggregates of spheres

The spherical scatterer model, on account of the ease of computation, has been widely used in the scientific literature and in many fields of application. However, the particles that are most commonly met in actual observations are nonspherical and the effects that stem from the lack of sphericity may be attenuated but never cancelled, not even by the use of an averaging procedure.

Several attempts were made to devise model nonspherical particles such that the optical properties could be calculated as exactly as possible, *i.e.*, without resorting to any approximation. The first real progress was marked by Bruning and Lo [90], who devised a technique to calculate the optical properties of linear chains of identical spherical scatterers. The properties of

this model were investigated by Peterson and Ström [91] for general geometry of the aggregation, whereas, the first application of the cluster model to the description of real particles is due to Gérardy and Ausloos [92]. In this subsection, we present the procedure devised by Borghese et al. for the calculation of the T-matrix for a group of N, not necessarily equal, spheres whose mutual distances are so small that they must be dealt with as one object [77]. The geometry of such kind of scatterer is arbitrary to a large extent, so that aggregates can be built to model particles of various shapes. The emphasis is on the T-matrix on account of the usefulness of the latter for performing orientational averages. The surrounding medium is assumed to be a homogeneous dielectric so that the incident field still has the form of a polarized plane wave whose multipole expansion is given by Eq. (2.27). The spheres are numbered by an index α while $\mathbf{R}_\alpha$ is the vector position of the center of the αth sphere of radius a_α and refractive index n_α. Furthermore, the following theory refers to aggregates of spheres that, if isolated, could be described by Mie Theory. The field scattered by the whole aggregate as the superposition of the fields scattered by each of the spheres is

$$\mathbf{E}_{\mathrm{s},\eta} = E_0 \sum_{\alpha=1}^{N} \sum_{plm} \mathcal{A}_{\eta\alpha lm}^{(p)} \mathbf{H}_{lm}^{(p)}(k_{\mathrm{m}}, \mathbf{r}_\alpha) \qquad (2.46)$$

where the amplitudes $\mathcal{A}_{\eta\alpha lm}^{(p)}$ should be calculated so that $\mathbf{E}_{\mathrm{s}\eta}$ satisfy the appropriate boundary conditions at the surface of each of the spheres. The radiation condition at infinity is automatically satisfied because the expansion includes $\mathbf{H}$-multipole fields only. The field within each sphere is taken in the form

$$\mathbf{E}_{\mathrm{p},\eta\alpha} = E_0 \sum_{plm} \mathcal{C}_{\eta\alpha lm}^{(p)} \mathbf{J}_{lm}^{(p)}(k_\alpha, \mathbf{r}_\alpha) \qquad (2.47)$$

where k_α is the wavenumber for each sphere. Due to the presence of the $\mathbf{J}$-multipole fields, the field is regular everywhere within the sphere. While the scattered field is given by a linear combination of multipole fields that have different origins, the incident field is given by a combination of multipole fields centered at the origin of the coordinates. Since the boundary conditions must be imposed at the surface of each of the spheres, e.g., of the αth sphere, the whole field can be rewritten in terms of multipole fields centered at $\mathbf{R}_\alpha$, resorting to the addition theorem [93]. The scattered field at the surface of the αth sphere turns out to be

$$\mathbf{E}_{\mathrm{s},\eta\alpha} = E_0 \sum_{plm} \left[\mathcal{A}^{(p)}_{\eta\alpha lm} \mathbf{H}^{(p)}_{lm}(k_{\mathrm{m}}, \mathbf{r}_\alpha) + \sum_{\alpha'} \sum_{p'l'm'} \mathcal{A}^{(p')}_{\eta\alpha'l'm'} \mathcal{H}^{(pp')}_{\alpha lm\alpha'l'm'} \mathbf{J}^{(p)}_{lm}(k_{\mathrm{m}}, \mathbf{r}_\alpha) \right].$$
(2.48)

Analogously, the incident field at the surface of the αth sphere is

$$\mathbf{E}_{\mathrm{i},\eta\alpha} = E_0 \sum_{plm} \left[\sum_{p'l'm'} W^{(p')}_{\mathrm{i},\eta l'm'} \mathcal{J}^{(pp')}_{\alpha lm0l'm'} \right] \mathbf{J}^{(p)}_{lm}(k_{\mathrm{m}}, \mathbf{r}_\alpha)$$
(2.49)

where $\mathbf{R}_0 = 0$ is the vector position of the origin and the quantities $\mathcal{H}$ and $\mathcal{J}$ respectively in Eqs. (2.48 - 2.49) are obtained applying the *addition theorem* to the vector Helmholtz harmonics $\mathbf{H}$ and $\mathbf{J}$ together with the properties of the Clebsch-Gordan coefficients. At this stage, using the same technique for homogeneous spheres, the boundary conditions can be imposed. Once this elimination is done, a system of linear nonhomogeneous equations is obtained such as

$$\sum_{\alpha'} \sum_{p'l'm'} \mathcal{M}^{(pp')}_{\alpha lm\alpha'l'm'} \mathcal{A}^{(p)}_{\eta\alpha lm} = -\mathcal{W}^{(p)}_{\mathrm{i},\eta\alpha lm},$$
(2.50)

where new coefficients have been defined as

$$\mathcal{W}^{(p)}_{\mathrm{i},\eta\alpha lm} = \sum_{p'l'm'} W^{(p')}_{\mathrm{i},\eta l'm'} \mathcal{J}^{(pp')}_{\alpha lm0l'm'}$$
(2.51)

$$\mathcal{M}^{(p,p')}_{\alpha lm\alpha'l'm'} = (R^{(p)}_{\alpha l})^{-1} \delta_{\alpha\alpha'} \delta_{pp'} \delta_{ll'} \delta_{mm'} + \mathcal{H}^{(pp')}_{\alpha lm\alpha'l'm'}.$$
(2.52)

In the last equation, the quantities $R^{(p)}_{\alpha l}$ are the Mie coefficients [Eq. (2.44)] for the scattering from the αth sphere. The matrix $\mathcal{H}$ describes the multiple scattering processes that, in view of the small mutual distance, occur with noticeable strength among the spheres of the aggregate. The amplitudes of the scattered field are calculated by solving the system of Eq. (2.50). Furthermore, the elements $\mathcal{H}^{(p,p')}_{\alpha lm\alpha'l'm'}$ of the transfer matrix couple multipole fields both of the same and of different parity with origin on different spheres. Then, the formal solution to the system of Eq. (2.50) is

$$\mathcal{A}^{(p)}_{\eta\alpha lm} = - \sum_{p'l'm'} \left[M^{-1} \right]^{(pp')}_{\alpha lm\alpha'l'm'} \mathcal{W}^{(p')}_{\mathrm{i},\eta\alpha'l'm'}.$$
(2.53)

This equation may lead to the conclusion that matrix $\mathbb{M}^{-1}$ be the T-matrix of the aggregate. This conclusion is incorrect however, because, according to Eq. (2.38), the T-matrix relates the multipole amplitudes of the

incident field to those of the field scattered by the whole object. On the contrary, Eq. (2.53) relates the amplitudes of the incident field to those of the fields scattered by each sphere in the aggregate. In order to define the T-matrix for the whole aggregate it is necessary to express the scattered field in terms of multipole fields with the same origin. Actually, with the help of the addition theorem, the scattered field [Eq. (2.48)] can be cast into the form

$$
\begin{aligned}
\mathbf{E}_{\mathrm{s},\eta} &= E_0 \sum_{plm} \left[\sum_{\alpha'} \sum_{p'l'm'} \mathcal{A}_{\eta\alpha'l'm'}^{(p')} \mathcal{J}_{0lm\alpha'l'm'}^{(pp')} \right] \mathbf{H}_{lm}^{(p)}(k_{\mathrm{m}}, \mathbf{r}_\alpha) \\
&= E_0 \sum_{plm} A_{\eta lm}^{(p)} \mathbf{H}_{lm}^{(p)}(k_{\mathrm{m}}, \mathbf{r}_\alpha),
\end{aligned}
\tag{2.54}
$$

which is valid at a large distance from the aggregate or, at least, outside the smallest sphere with center at $\mathbf{R}_0$ that includes the whole aggregate. The preceding equation shows that the field scattered by the whole cluster can be expanded as a series of vector multipole fields with a single origin provided that the amplitudes are

$$
A_{\eta lm}^{(p)} = \sum_{\alpha'} \sum_{p'l'm'} \mathcal{A}_{\eta\alpha'l'm'}^{(p')} \mathcal{J}_{0lm\alpha'l'm'}^{(pp')}.
\tag{2.55}
$$

Then, the T-matrix of the aggregate can be defined in a compact form as

$$
T_{lml'm'}^{(pp')} = -\sum_{\alpha\alpha'} \sum_{qLM} \sum_{q'L'M'} \mathcal{J}_{0lm\alpha LM}^{(pq)} \left[M^{-1} \right]_{\alpha LM\alpha'L'M'}^{(qq')} \mathcal{J}_{\alpha L'M'0l'm'}^{(q'p')}.
\tag{2.56}
$$

The T-matrix defined in the preceding equation has the correct transformation properties under rotation, although it is non diagonal as a consequence of the lack of spherical symmetry of the aggregate.

A crucial aspect concerning the computation is the convergence of the results. In order not to lose generality, we consider the light scattering by a cluster of particles, such as our model nanowire. The calculation of the T-matrix of an aggregate requires inverting the matrix $\mathbb{M}$ whose order is, in principle, infinite. Of course the system (2.50) is truncated to some finite order by including in Eq. (2.56) terms up to order L_M, the maximum value both for L and L' in Eq. (2.56). The maximum value is chosen to ensure the required accuracy of the transition matrix elements. For a cluster of N spheres this implies the solution of a system of order $D_M = 2NL_M(L_M + 2)$, which may become too large. Actually, the inversion of the matrix $\mathbb{M}$ is

responsible for most of the time required for the calculation and this time scales, in fact, as D_M^3. Thus, on account of the definition of D_M , the computation time scales as L_M^6 whereas the storage requirements scale as L_M^4, so that it pays, in terms of both CPU time and storage requirements, to keep L_M as low as practicable. The choice of the appropriate value of L_M has been the concern of several researchers. For instance Quinten et al. [94] used the criterion suggested by Wiscombe [95]. The choice of L_M has been guided by the considerations provided by Iatì et al [25]. For an isolated dielectric sphere with radius a_s we have to choose $L_M > ka_s + m_s$ [83], where $k = nk_\nu, k_\nu = \omega/c$ is the wavenumber of the particle and m_s is an integer that depends on the refractive index. Now, by looking to Eqs. (2.50 - 2.52), we see that what distinguishes a set of independent spheres from a true aggregate of spheres is the presence of the elements $\mathcal{H}_{\alpha lm\alpha'l'm'}^{(pp')}$ that describe the multiple scattering processes occurring among the spheres. Of course, these processes become less and less effective the more the spheres are separated. By looking to the explicit expression of the $\mathcal{H}$-elements [21], one sees that their magnitudes actually become smaller and smaller for well separated spheres. As a result, we can assume that, choosing L_M a little larger than necessary to ensure the convergence of the component spheres as if they were isolated, we should also get fairly convergent values for the transition matrix elements. Thus we make the Ansatz that we can choose $L_M > k_\nu a_c + m_c$, where a_c is the radius of the smallest sphere including the entire aggregate. Even in this case m_c is an integer that depends on the refractive index.

2.6 Radiation force and torque in T-matrix formalism

In the final section we introduce the optical force [Eq. (2.1)] and torque [Eq. (2.4)] using the asymptotic properties of the vector Helmholtz harmonics and the T-matrix formalism, which has been discussed above. In fact, the expressions for the radiative force [Eq. (2.1)] and torque [Eq. (2.4)] can be significantly simplified in the far-field region ($r \to \infty$) and using the T-matrix formalism. Here, the incident $\mathbf{E}_i$, scattered $\mathbf{E}_s$ and internal $\mathbf{E}_p$ fields are expanded in terms of vector spherical harmonics $\mathbf{Z}_{lm}^*$. Moreover the integration can be performed over a spherical surface of radius r, large enough so that only transverse fields are taken in the integration since vanishing terms at infinity are neglected in the integration. A basic requirement for the correct integration in Eqs. (2.1 - 2.4) is that the particle has to be contained

inside the sphere and it is centered at the origin of the reference system. Due to the orthogonality between $\mathbf{Z}_{lm}^*$ and the radial unit vector $\hat{\mathbf{r}}$, the integrals of the first and second term of the Eq. (2.3) are identically zero. Therefore the optical force is due only to the contribution of the integral of the third term of Maxwell stress tensor. For a non-magnetic medium the optical force is:

$$\mathbf{F}_{\mathrm{rad}} = -\frac{\varepsilon_{\mathrm{m}} r^2}{4} \int_{\Omega} \left[|\mathbf{E}_{\mathrm{s}}|^2 + \frac{c^2}{n_{\mathrm{m}}^2} |\mathbf{B}_{\mathrm{s}}|^2 + 2\Re \left\{ \mathbf{E}_{\mathrm{i}} \cdot \mathbf{E}_{\mathrm{s}}^* + \frac{c^2}{n_{\mathrm{m}}^2} \mathbf{B}_{\mathrm{i}} \cdot \mathbf{B}_{\mathrm{s}}^* \right\} \right] \hat{\mathbf{r}} \, \mathrm{d}\Omega$$

$$(2.57)$$

where the integration is now carried out over the full solid angle $\Omega = 4\pi$ that represents the full solid angle describing the spherical surface. In the same way also the torque can be integrated over a spherical surface of radius r which contains the particle. Here it is convenient to set the center-of-mass of the particle as origin of the reference system. Considering Eq. (2.3), the integrals of the last two terms do not give any contribution to the torque, therefore it is given by:

$$\mathbf{\Gamma}_{\mathrm{rad}} = -\frac{\varepsilon_{\mathrm{m}} r^3}{2} \Re \left\{ \int_{\Omega} \left[(\hat{\mathbf{r}} \cdot \mathbf{E})(\mathbf{E}^* \times \hat{\mathbf{r}}) + \frac{c^2}{n_{\mathrm{m}}^2} (\hat{\mathbf{r}} \cdot \mathbf{B})(\mathbf{B}^* \times \hat{\mathbf{r}}) \right] \mathrm{d}\Omega \right\}. \quad (2.58)$$

The latter two expressions are the starting point for the electromagnetic calculations of optical forces and torque in optical trapping. We recall that the key point is to solve the scattering problem by calculating the scattered fields and consequently the Maxwell stress tensor. However, the calculation of forces an torques in this regime is usually a complicate procedure [21]. Thus, various algorithms have been developed to handle this problem [96, 97]. Among the different approaches, a successful method is based on the calculation of the transition matrix [21]. This is particularly useful and computationally effective because it is possible to exploit the rotation and translation properties of the T-matrix to obtain at once optical forces and torques for different positions and orientations of the trapped particles [17, 18, 80, 81, 98, 99, 100, 101, 102]. For these reasons, we have used this approach to compute the quantities of interest (forces, cross sections, maps) on the model particles studied in this thesis.

2.6.1 Optical forces due to a plane wave

An important case is the calculation of the optical force exerted by a linearly polarized plane wave on a particle. The incoming electric field associated to the linear polarized plane wave is expressed by Eq. (2.17). Starting

47

from Eq. (2.57), after some substitutions and mathematical steps [5], the force originated from the scattering process of a linear polarized plane wave by a spherical homogeneous particle is written as [79]:

$$\mathbf{F}_{\text{rad}} = \frac{n_{\text{m}}}{c} I_0 \left[\sigma_{\text{scat}} \hat{\mathbf{k}}_{\text{i}} - \int_{\Omega} \frac{\text{d}\sigma_{\text{scat}}}{\text{d}\Omega} \hat{\mathbf{r}} \, \text{d}\Omega \right] \tag{2.59}$$

where $I_0 = \frac{n_{\text{m}}c}{2} E_0^2$ is the intensity of the incident plane wave and $\text{d}\sigma_{\text{scat}}/\text{d}\Omega = |\mathbf{f}(\hat{\mathbf{r}}, \hat{\mathbf{k}}_{\text{i}})|^2$ is the differential scattering cross-section. The right side of this equation is composed by a first term that represents a force in $\hat{\mathbf{k}}_{\text{i}}$ direction and a second term which can present also a force component perpendicular to $\hat{\mathbf{k}}_{\text{i}}$ [79]. Therefore the component of the force along the propagation direction represents the radiation pressure:

$$\mathbf{F}_{\text{rad}}^{\parallel} = \frac{n_{\text{m}}}{c} I_0 \left[\sigma_{\text{ext}} - g_{\text{i}}\sigma_{\text{scat}} \right] \hat{\mathbf{k}}_{\text{i}} \tag{2.60}$$

while the transverse component of the force is:

$$\mathbf{F}_{\text{rad}}^{\perp} = -\frac{n_{\text{m}}}{c} I_0 \, \sigma_{\text{scat}} \left[g_1 \hat{\mathbf{e}}_{\text{i}} + g_2 (\hat{\mathbf{k}}_{\text{i}} \times \hat{\mathbf{e}}_{\text{i}}) \right] \tag{2.61}$$

where g_1 is the asymmetry parameter in the incoming wave direction [Eq. (2.22)], while g_1 and g_2 are transverse asymmetry parameters [Eqs. (2.23 - 2.24)]. For a spherical particle only g_1 is different from zero, while for small dipolar particles all the parameters g_{i}, g_1 and g_2 are zero. The optical torque exerted by a linear polarized plane wave on a spherical particle is zero. However, torque is not zero in presence of elliptically polarized light and when the beads are made of an absorbing material [103].

On the other hand, when we deal with scatterers more complex than the single homogeneous sphere, such as radially symmetric non-homogeneous scatters or cluster, the expression of the radiation force [Eq. (2.57)] should be rewritten in terms of T-matrix formalism. By substituting the expansions of the incident [Eq. (2.27)] and scattered waves [Eq. (2.30)] in terms of multipoles taken in the asymptotic limit $(r \to \infty)$ into Eq. (2.57) [5], the expression for the radiation force along the direction of a unit vector $\hat{\mathbf{u}}$, $i.e.$, $F_{\text{rad}}(\hat{\mathbf{u}}) = \mathbf{F}_{\text{rad}} \cdot \hat{\mathbf{u}}$ can be obtained, such as:

$$F_{\text{rad}}(\hat{\mathbf{u}}) = -\frac{\varepsilon_{\text{m}}E_0^2}{2k_{\text{m}}^2} \Re \left\{ \sum_{plm} \sum_{p'l'm'} i^{l-l'} I_{lml'm'}^{(pp')}(\hat{\mathbf{u}}) \left[A_{\text{s},lm}^{(p)*} A_{\text{s},l'm'}^{(p')} + W_{\text{i},lm}^{(p)*} A_{\text{s},l'm'}^{(p')} \right] \right\} , \tag{2.62}$$

where the amplitudes $W_{\text{i},lm}^{(p)*}$ of the incident field and the amplitudes $A_{\text{s},l'm'}^{(p)}$ of the scattered field are given by Eq. (2.38) or Eq. (2.53) in terms of the

elements of the T-matrix, depending on if we deal with a single sphere or a cluster. Furthermore, in this equation,

$$I_{lml'm'}^{(pp')}(\hat{\mathbf{u}}) = \oint_\Omega (\hat{\mathbf{r}} \cdot \hat{\mathbf{u}})\, i^{p-p'}\, \mathbf{Z}_{lm}^{(p)*}(\hat{\mathbf{r}}) \cdot \mathbf{Z}_{l'm'}^{(p')}(\hat{\mathbf{r}})\, \mathrm{d}\Omega\;. \tag{2.63}$$

The integrals $I_{lml'm'}^{(pp')}(\hat{\mathbf{u}})$ can be expressed in closed form [17] as

$$I_{lml'm'}^{(pp')}(\hat{\mathbf{u}}) = \frac{4\pi}{3} \sum_{\mu=-1,0,1} Y_{1\mu}^*(\hat{\mathbf{u}}) K_{\mu;lml'm'}^{(pp')}\;, \tag{2.64}$$

where the unit vectors are expressed in terms of spherical harmonics through:

$$
\begin{aligned}
K_{\mu;lml'm'}^{(pp')} &= \oint_\Omega Y_{1\mu}(\hat{\mathbf{r}}) i^{p-p'} \mathbf{Z}_{lm}^{(p)*}(\hat{\mathbf{r}}) \cdot \mathbf{Z}_{l'm'}^{(p')}(\hat{\mathbf{r}})\, \mathrm{d}\Omega \\
&= \sqrt{\frac{3}{4\pi}} C_1(l',l;\mu,m-\mu) O_{ll'}^{(pp')}\;,
\end{aligned} \tag{2.65}
$$

in which in turn

$$
O_{ll'}^{(pp')} =
\begin{cases}
\sqrt{\dfrac{(l-1)(l+1)}{l(2l+1)}} & l' = l-1 \text{ and } p = p' \\[2ex]
-\dfrac{1}{\sqrt{l(l+1)}} & l' = l \text{ and } p \neq p' \\[2ex]
-\sqrt{\dfrac{l(l+2)}{(l+1)(2l+1)}} & l' = l+1 \text{ and } p = p' \\[2ex]
0 & \text{otherwise}
\end{cases}
$$

and $C_1(l',l;\mu,m-\mu)$ are Clebsch-Gordan coefficients. The force expressed by Eq. (2.62) can be separated into two parts, *i.e.*,

$$F_{\mathrm{rad}}(\hat{\mathbf{u}}) = -F_{\mathrm{scat}}(\hat{\mathbf{u}}) + F_{\mathrm{ext}}(\hat{\mathbf{u}})\;, \tag{2.66}$$

where

$$F_{\mathrm{scat}}(\hat{\mathbf{u}}) = \frac{\varepsilon_{\mathrm{m}} E_0^2}{2 k_{\mathrm{m}}^2} \Re \left\{ \sum_{plm} \sum_{p'l'm'} A_{\mathrm{s},lm}^{(p)*} A_{\mathrm{s},l'm'}^{(p')} i^{l-l'} I_{lml'm'}^{(pp')}(\hat{\mathbf{u}}) \right\} \tag{2.67}$$

and

$$F_{\text{ext}}(\hat{\mathbf{u}}) = -\frac{\varepsilon_{\text{m}} E_0^2}{2k_{\text{m}}^2} \Re \left\{ \sum_{plm} \sum_{p'l'm'} W_{\text{i},lm}^{(p)*} A_{\text{s},l'm'}^{(p')} i^{l-l'} I_{lml'm'}^{(pp')}(\hat{\mathbf{u}}) \right\} . \qquad (2.68)$$

$F_{\text{scat}}(\hat{\mathbf{u}})$ depends on the amplitudes $A_{\text{s},lm}^{(p)}$ of the scattered field only, while $F_{\text{ext}}(\hat{\mathbf{u}})$ depends both on $A_{\text{s},lm}^{(p)}$ and on the amplitudes $W_{\text{i},lm}^{(p)}$ of the incident field. This dependence is analogous to that on the scattering and extinction cross-sections for the force exerted by a plane wave.

2.6.2 Optical forces due to a focused beam

The most important case for the scope of this thesis is the computation of the radiation forces in a optical trap composed by focused laser beam with high-NA. In order to calculate the multipole amplitudes $\tilde{W}_{\text{i},lm}^{(p)}$ of a focused beam, the expansion of the incoming beam into plane waves and its focusing can be exploited as described in the Sect. (1.4). The expansion of the focused beam around the focal point is given by Eq. (1.11), i.e.,

$$\mathbf{E}_{\text{f}}(x, y, z) = \frac{ik_{\text{t}} f e^{-ik_{\text{t}} f}}{2\pi} \int\limits_0^{\theta_{\max}} \sin\theta \int\limits_0^{2\pi} \mathbf{E}_{\text{ff},t}(\theta, \varphi) e^{i[k_{\text{t},x} x + k_{\text{t},y} y]} e^{ik_{\text{t},z} z} \, \mathrm{d}\varphi \, \mathrm{d}\theta ,$$

where each plane wave transmitted through the objective lens $\mathbf{E}_{\text{ff},t}(\theta, \varphi)$ can be expanded into multipoles according to Eq. (2.27), i.e.,

$$\mathbf{E}_{\text{ff},t}(\theta, \varphi) \equiv \mathbf{E}_{\text{i}}(r, \hat{\mathbf{r}}) = E_0 \sum_{plm} W_{\text{i},lm}^{(p)}(\hat{\mathbf{k}}_{\text{i}}, \hat{\mathbf{e}}_{\text{i}}) \mathbf{J}_{lm}^{(p)}(k_{\text{m}} r, \hat{\mathbf{r}}) ,$$

with the amplitudes given by Eqs. (2.29). Therefore, the amplitudes of the focused field are

$$\tilde{W}_{\text{i},lm}^{(p)}(\mathbf{P}) = \frac{ik_{\text{t}} f e^{-ik_{\text{t}} f}}{2\pi} \int\limits_0^{\theta_{\max}} \sin\theta \int\limits_0^{2\pi} E_{\text{i}}(\theta, \varphi) \, W_{\text{i},lm}^{(p)}(\hat{\mathbf{k}}_{\text{i}}, \hat{\mathbf{e}}_{\text{i}}) \, e^{ik_{\text{t}} \cdot \mathbf{P}} \, \mathrm{d}\varphi \, \mathrm{d}\theta, \quad (2.69)$$

where the centre around which the expansion is performed is considered displaced by $\mathbf{P}$ with respect to the focal point $\mathbf{O}$ and the amplitudes $\mathcal{W}_{lm}^{(p)}(\mathbf{P})$ define the focal field and can be numerically calculated once the characteristics of the optical system are known. The radiation force are calculated

through the knowledge of the scattered amplitudes $\tilde{A}^{(p)}_{s,lm}$, *e.g.*, by using the T-matrix [Eqs. (2.38 - 2.53)] and:

$$F_{\text{rad}}(\hat{\mathbf{u}}) = -\frac{\varepsilon_{\text{m}}}{2k_{\text{m}}^2}\Re\left\{\sum_{plm}\sum_{p'l'm'}i^{l-l'}I^{(pp')}_{lml'm'}(\hat{\mathbf{u}})\left[\tilde{A}^{(p)*}_{s,lm}\tilde{A}^{(p')}_{s,l'm'} + \tilde{W}^{(p)*}_{i,lm}\tilde{A}^{(p')}_{s,l'm'}\right]\right\}.$$

$$(2.70)$$

In practice, the expression of the force in this equation is obtained from the correspondent one for the plane wave [Eq. (2.62)] *mutatis mutandis* by changing $E_0 W^{(p)}_{i,lm} \to \tilde{W}^{(p)}_{i,lm}(\mathbf{P})$ and $E_{\text{i}} A^{(p)}_{s,lm} \to \tilde{A}^{(p)}_{s,lm}$ [17].

Chapter 3

Size scaling in optical trapping of spherical particles and nanowires

In this chapter, we present numerical results on optical trapping of dielectric (polystyrene) spherical particles and nanowires. We use numerical codes based on light scattering in the T-matrix framework to calculate optical forces through the Maxwell stress tensor. We explore the properties of optical trapping as a function of particle size (size scaling) for both spheres and nanowires. We discuss how shape controls the mechanical effects of light at the mesoscale.

3.1 Polystyrene sphere

We consider the paradigmatic model of non-absorbing polystyrene spheres of different size. Polystyrene, $(C_8H_8)_n$, spheres are a typical sample used in optical tweezers experiments since they are easily purchased in accurate spherical shape and are used as size standard in microscopy techniques. They are easily functionalized and are well suited for optical tweezers applications in a biological environment [11]. Thus, they often represent the standard sample used for optical force calibration in optical tweezers [104]. The particle refractive index is $n_p(\lambda_0 = 830 \text{ nm}) = 1.57$ [105]. For our calculations we choose the parameters of the optical tweezers experimental setup at CNR-IPCF. Thus, we fix the wavelength of the trapping laser beam at $\lambda_0 = 830$ nm and we consider the particles immersed in water ($n_m = 1.33$). We consider a gaussian laser beam, as schematized in Fig. (1.3), focused by an ideal aplanatic lens which does not absorb and does not produce any aberration.

The numerical aperture [Eq. (1.10)] of the objective lens is taken as NA= 1.3.

We are interested in the exact calculation of optical forces, related trap stiffnesses, and their scaling with particle size (*size scaling*). We cover a wide size range with particle radius ranging from 50 nm (well within the Rayleigh regime) up to 1.4 μm (for which ray optics can be used for optical force calculations). Therefore, the size parameter [Eq. (1.1)] ranges between $[0.50 - 14.09]$ and only at the extreme values of the considered interval we could, in principle, apply ray optics or dipole approximation calculations. This is indeed the typical size range of optical tweezers experiments [5].

For accurate calculations of the optical forces we use the T-matrix approach [see Sect. (2.4)] and then we compare results with dipole approximation for a better understanding of the size scaling. In our computational method we follow the general formulation of light scattering described in Chap. (2). First, we calculate the focal fields by using the angular spectrum representation of a focused gaussian beam written in paraxial approximation [Eq. (1.11)]. These are the incident fields that together with the scattered fields are expanded in a series of vector spherical harmonics with known amplitudes, $W_{i,lm}^{(p)}$ and $A_{s,lm}^{(p)}$ [Eqs. (2.27 - 2.30)], respectively. Then, the elements of the transition matrix $T_{l'm'lm}^{(p'p)}$ are calculated by the inversion of the matrix of the linear system obtained by imposing the boundary conditions to the fields across the spherical surface [see Eq. (2.39)]. The resulting elements are used to calculate the Maxwell stress tensor, the optical forces, and the trapping properties in which we are interested. Finally, in our calculations, the direction of propagation of the beam is taken along z, therefore the plane of polarization is xy.

A graph of the calculated strongly focused incident field intensity is provided in Fig. (3.1). In these field intensity maps it is evident how the most elongated region is along the propagation (axial) direction, z, as expected for a focused gaussian beam. Moreover, in the xy plane the linear polarization of the incident beam breaks the cylindrical symmetry in the focal plane producing a tighter spot size along y with respect to the polarization direction, x. This has observable consequences also on the symmetry of the optical trap and the transverse stiffnesses, κ_x and κ_y, particularly when dealing with nanostructures [12, 37].

3.1.1   Cartesian components of the optical force

Within the approach previously presented, we have computed the (x, y, z) components of the optical force on the points of a grid employed with specified resolution. These components are calculated in a micron-sized range,
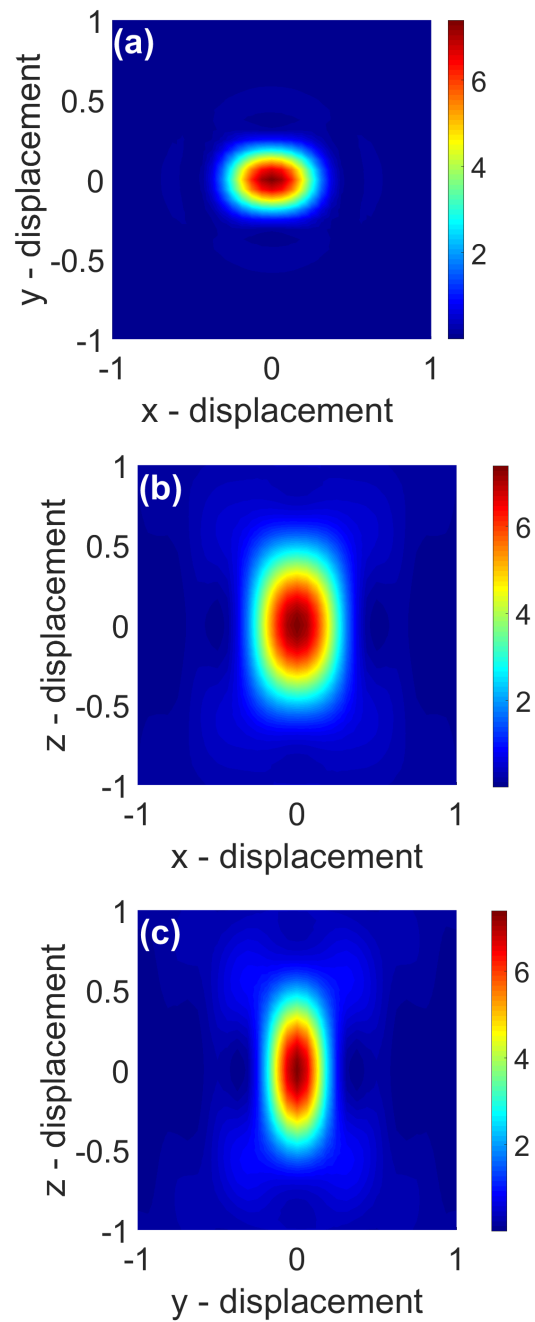
Figure 3.1: Maps of the focused field intensity normalized to the field entering the objective lens in the xy (a), xz (b), and yz (c) planes. We have considered a strongly focused field (NA = 1.3) that is linearly polarized along x and propagates along the z direction. Therefore, in the xy plane the cylindrical symmetry of the intensity map is broken by the polarization, while in xz and yz planes the shape of the field appears elongated because of the beam propagation.

55

[−1.4 μm,1.4 μm], around the paraxial nominal focus of the beam. So, we can plot the force as a function of particle displacement in each spatial direction, x, y, z. The trapping position of the particle in the longitudinal (z) direction is typically offset from the centre of the grid because of the 'pushing' effect of the optical scattering force. To calculate the force on the particle at the equilibrium position, the z (longitudinal) coordinate at which the axial force vanishes must first be found. The force plots in the transverse directions (x, y) can then be calculated. As discussed in Sect. (1.3), it is often convenient to calculate the dimensionless force (trapping) efficiencies along the three cartesian directions, $Q_i = cF_i/n_\mathrm{m}P$ with $i = x, y, z$. In Fig. (3.2) we show them as calculated for individual latex spheres with radius $a = [50$ nm, 300 nm, 600 nm, 1400 nm]. This is an interval spanning from the nano- to the meso-scale, at small size of the particle [Figs. (3.2a - 3.2b - 3.2c)], the graphs present a relative maximum and minimum approximately at the particle radius. As expected, it is here that the greatest restoring force is exerted. Instead, for larger dimensions of the particle, the curve tends to flatten out towards zero in proximity of the equilibrium point [Fig. (3.2d)]. The reason is that for larger particles the volume of the particle exceeds the interaction volume related with the laser spot, and the related stiffness tends to zero.

The convergence of the results has been carefully checked through the examined particle size range and we use a multipole order $l_M = 15$ in all the computations.

3.1.2   Trap stiffnesses and size scaling

Size scaling is a paradigm of nanoscience [38, 106]. It characterizes solid state systems for many applications in the most different research fields [107]. Crucial properties of materials and interactions change dramatically with size [108]. Much progress has already been done in the synthesis, assembly, and fabrication of nanomaterials, and, equally important, toward a wide variety of technological applications [109]. The properties of materials with nanometric dimensions are significantly different from those of atoms or bulk materials, and the appropriate control of such properties at this mesoscale have led to new science as well as new products, devices and technologies [106]. The size scaling properties of optical forces help us understand the important features of optical trapping in a wide size range and their comparison with experiments.

As mentioned in Chap. (1) [see Eq. (1.8)] and clearly shown in Fig. (3.2), in proximity of the equilibrium point the optical force can be linearized as an elastic restoring force with negative slope, e.g., $F_x \approx -\kappa_x x$. Thus, opti-
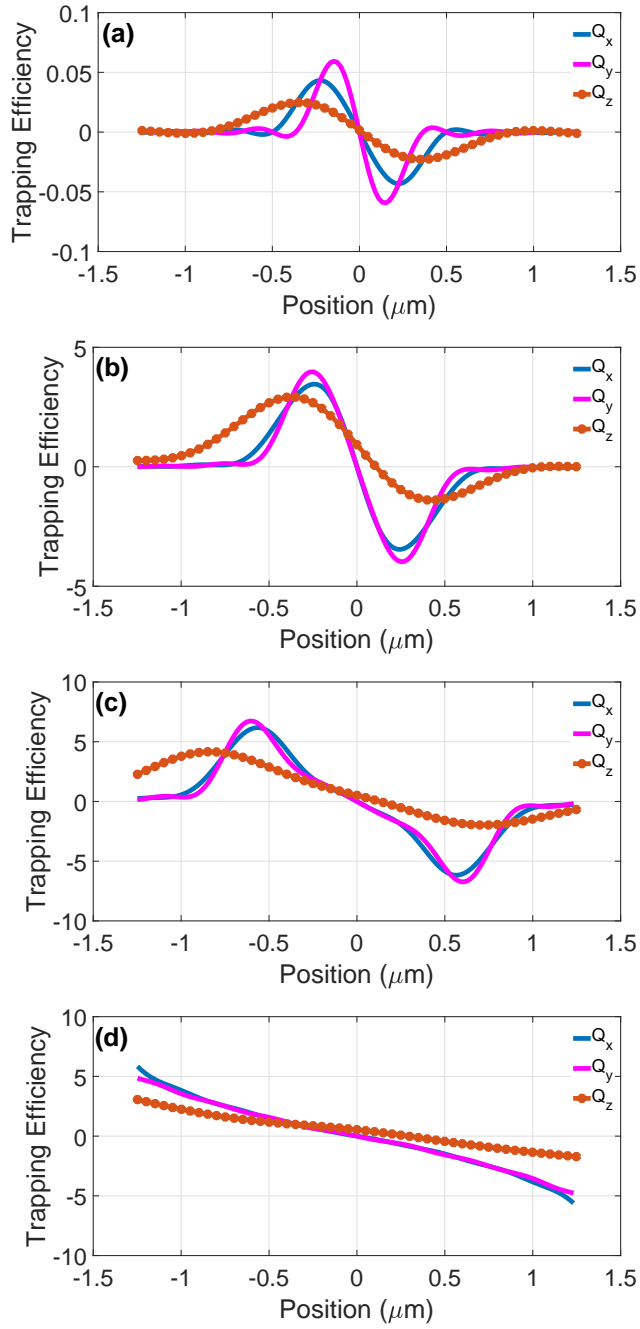
Figure 3.2: Trapping efficiencies (Q_x, Q_y, Q_z) for a latex ($n_{\mathrm{p}} = 1.57$) sphere immersed in water ($n_{\mathrm{m}} = 1.33$) in the transverse, x, y, and longitudinal, z, directions, as function of displacement from the nominal paraxial focus. The model spheres have radius: 50 nm (a), 300 nm (b), 600 nm (c), 1400 nm(d). The focal spot is obtained overfilling an aplanatic water-immersion objective (NA= 1.30). The dots are referred to the calculated efficiencies on the grid points.

57

cal tweezers can be approximated with an effective harmonic potential with spring constants or trap stiffnesses κ_x, κ_y κ_z. These quantities are of crucial importance in experiments because represent quantities measured when performing optical tweezers calibration [110]. In order to calculate the optical trap stiffnesses, we simply get the slope of the force-displacement graphs at the equilibrium position, where the force vanishes. In Fig. (3.3) we show the calculated stiffnesses as a function of particle radius (or, equivalently, of the size parameter since we work at fixed wavelength).

As observed for the individual force graphs, the spring constants tend to zero for large particles in all cartesian components. In the three graphs, an absolute maximum is present corresponding to a radius of $a \approx 300$ nm. This is the radius for which the volume of the scatterer overlaps the laser spot, optimizing the interaction region. However, the peak in the axial direction [Fig. (3.3c)] is more depressed than in the transverse ones [Figs. (3.3a - 3.3b)]. This is due to the shape of the focal spot shown in Fig. (3.1), representing the maps associated with the incident field, which show a tighter profile in the transverse direction than in the axial one, yielding a tighter effective potential and a larger stiffness in x, y with respect to z. For size larger than this maximum, the trend of the constants undergoes a hyperbolic scaling behaviour, $\kappa \propto a^{-1}$, this is also consistent with calculations in the ray optics approximation [5]. Using the T-matrix approach, we can reproduce the full electromagnetic theory of optical forces with great precision. In fact, when particles become larger than the interaction region, we also find the onset of modulation in the stiffnesses caused by the interference between the different multipoles. An exhaustive explanation of the interplay between the different multipoles for mesoscale particles is described by Nieminen et al. [111].

On the other hand, for smaller values, the behavior of the trap constants increases cubically, $\kappa \propto a^3$, according, in first approximation, to the Rayleigh approximation discussed in Chap. (1). As an example, in Fig. (3.4a), we compared the trend of the axial stiffness, calculated with the T-matrix approach, Fig. (3.3), with what is analytically obtained by a dipole approximation [see Subsect. (1.5.2)] and considering a diffraction limited Gaussian beam spot. Here the Gaussian beam waist, w_0, that appears in the expression of the spring constants κ_ρ^{G} and κ_z^{G} [Eqs. (1.28 - 1.31)] is provided by the Abbe criterion [66, 112] so that $w_0 = 0.5\lambda_0/\mathrm{NA}$. As shown by a logarithmic scale plot in Fig. (3.4b), the comparison between values calculated in dipole approximation and T-matrix is very good up to 200 nm. The trend, which goes as a^3, is related to the proportionality of the quasi-static Clausius-Mossotti polarisability to the volume of the scatterer [see Eq. (1.14)]. The same type of comparison and considerations hold for size scaling of κ_x and κ_y. The first experimental study of a full size scaling from nano to microscale was
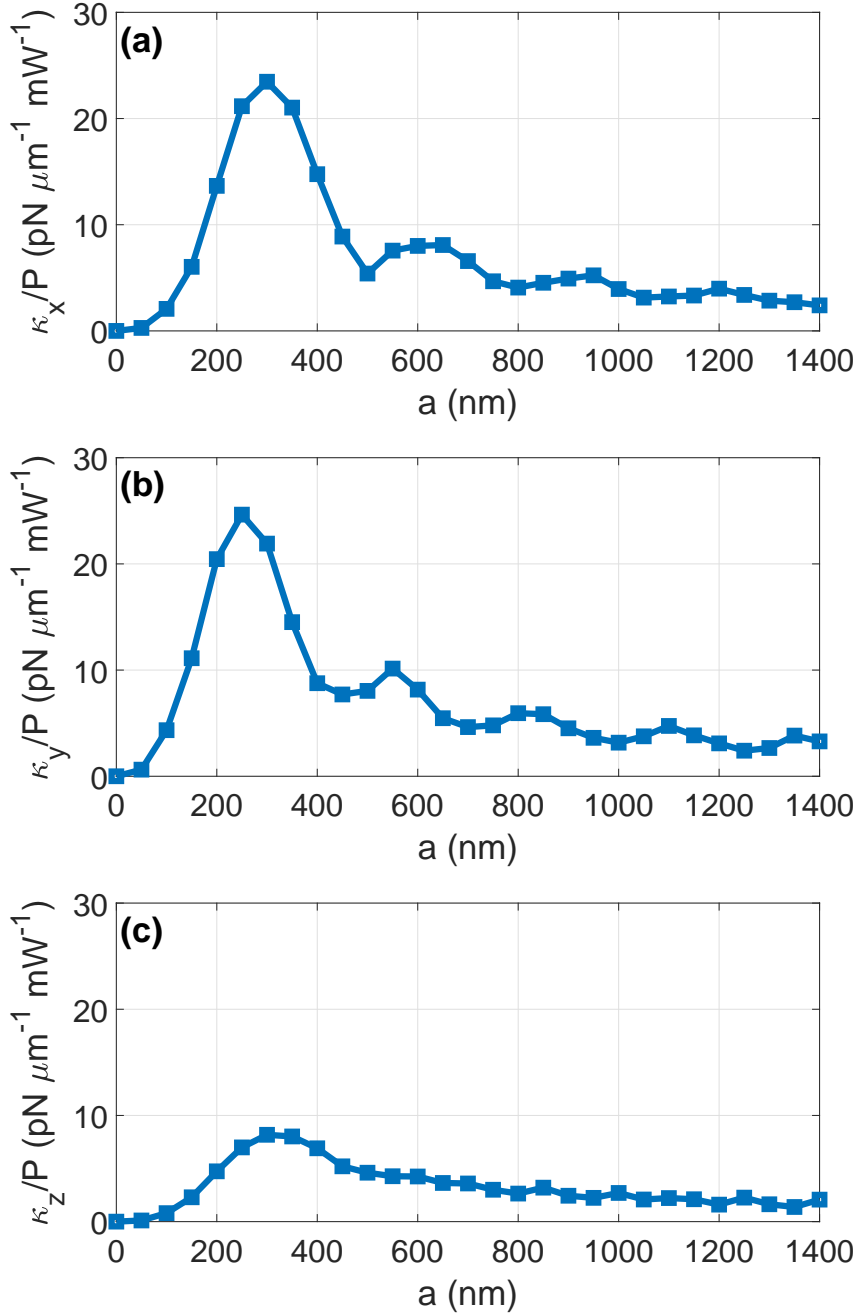
Figure 3.3: Optical trap stiffnesses, κ_x (a), κ_y (b), κ_z (c), for a latex ($n_{\mathrm{p}} = 1.57$) sphere immersed in water ($n_{\mathrm{m}} = 1.33$) in the transverse, x (a) - y (b), and longitudinal z (c) directions, as a function of the particle radius a. The radius of the considered spheres spans in the interval [50 nm - 1400 nm]. The dots, excluding zero, are the calculated points.
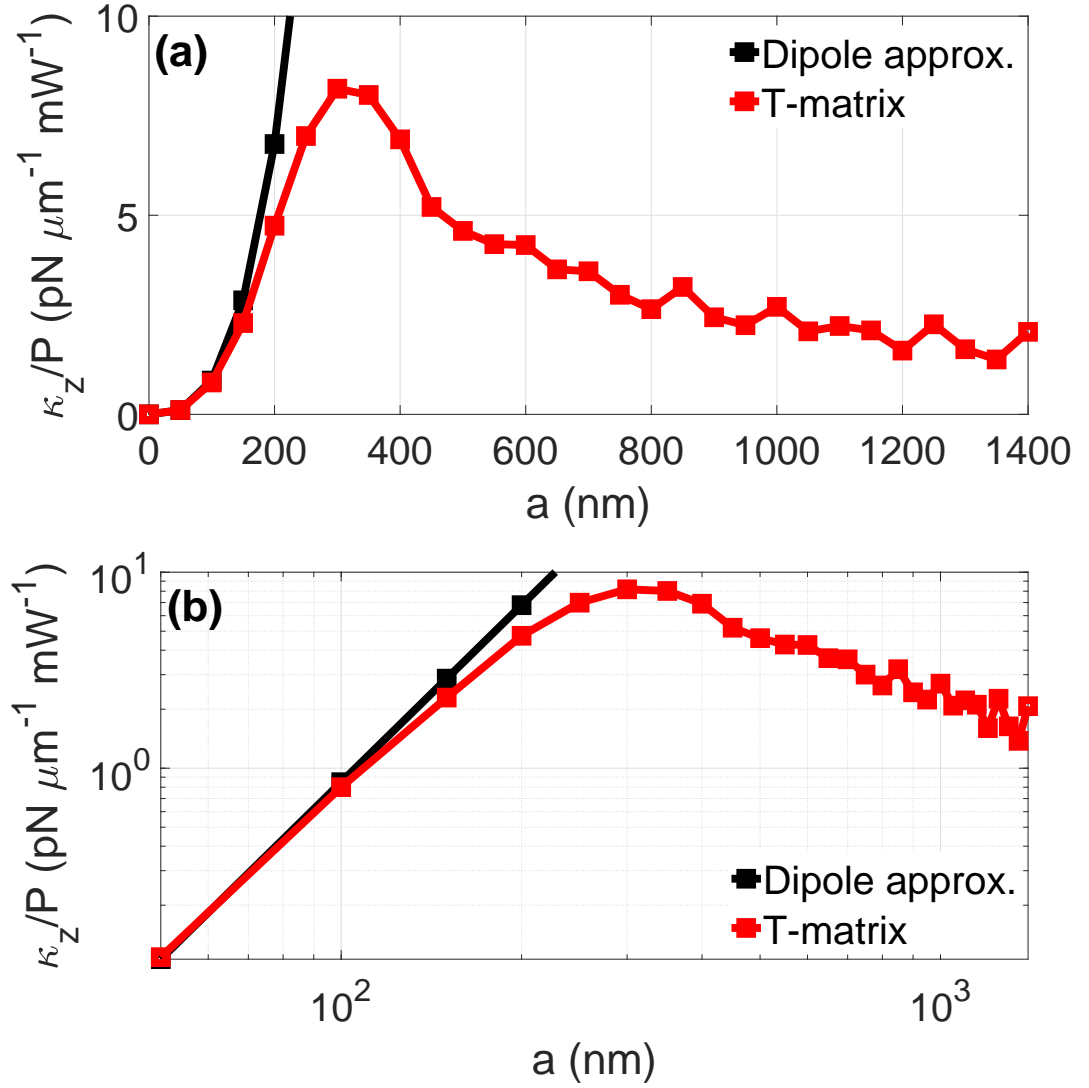
Figure 3.4: Optical trap stiffnesses along the z-direction for a latex ($n_{\mathrm{p}} = 1.57$) sphere immersed in water ($n_{\mathrm{m}} = 1.33$) as a function of the particle radius a. The radius of the considered spheres spans in the interval [50 nm - 1400 nm] (d). The red data are obtained using the T-matrix approach. The black line is, instead, referred to the dipole approximation calculations considering a diffraction limited Gaussian beam. Fig. (a) is a linear plot while in Fig. (b) we have used the logarithmic scale.

reported by Rohrbach [104].

3.2 Polystyrene nanowire

The second type of particles we have considered are dielectric nanowires. Nanowires have attracted considerable interest within the scientific community as an innovative material with applications in nanotechnology [113]. They are defined as structures with a high aspect ratio, being characterized by two spatial dimensions in the range of tens of nanometers and the third one on a much longer scale, typically micrometers. Moreover, due to their very large surface-to-volume ratio, nanowires can lead to strongly enhanced surface effects as compared to bulk materials. Their extreme geometry, combined, in the case of semi-conducting nanowires, with important intrinsic physical properties, leads to a wide range of novel physical applications. Because of their potential technological importance, the ability to manipulate, characterize and integrate nanowires on an individual basis is highly desirable, and optical trapping provides an ideal platform to achieve these aims [38, 114].

We model the nanowires as linear chains of homogeneous non-absorbing spherical particles of latex spheres [18]. Here, we focus our attention only to nanowires aligned along the direction of propagation of the incident field (z) with the aim to investigate their length scale behaviour. This is justified by the fact that the optical torque aligns the nanowires along the axial propagation direction [18] as also experimentally observed on average [38, 114]. Following the philosophy adopted for the previous case of the sphere, we model the trapping of a linear particle cluster by a laser beam with fixed wavelength $\lambda_0 = 830$ nm and numerical aperture NA= 1.3. We are interested, once again, in the calculation of the optical forces and in particular on how the trap stiffnesses scale as a function of the nanowire length, L. Each sphere composing the linear cluster has refractive index $n_{\rm p}(\lambda_0 = 830$ nm$) = 1.57$ [105] and they are immersed in water ($n_{\rm m} = 1.33$). The radius of the single sphere is fixed to 50 nm because the idea is to model a linear structure that grows along the longitudinal direction z, at the mesoscale and remains at the nanoscale in the transverse plane xy. The calculation is conducted for different lengths and, by adding the spheres, we work in a range in which the half-length of the cluster, $L/2$, spans from 50 nm (a single sphere) to 1500 nm (corresponding to 30 spheres in the cluster). In Fig. (3.5) an example of this arrangement is sketched, where we consider a nanowire composed by $N = 10$ spheres.

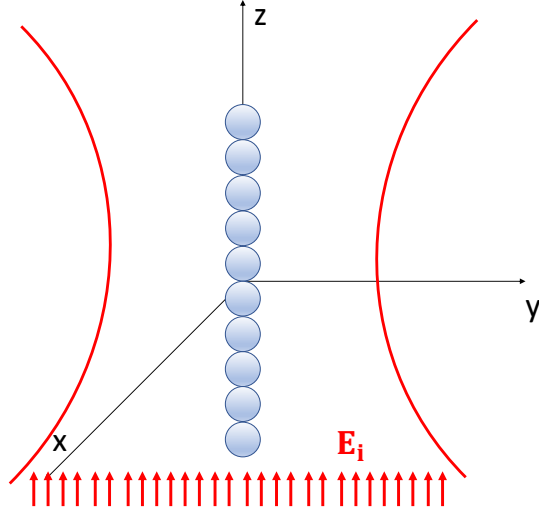Given the complexity of the scatterer, which has only cylindrical sym-

61

Figure 3.5: Model for a nanowire of 1 μm. It is composed by $N = 10$ spheres of radius 50 nm. The system shows a cylindrical symmetry with respect to the direction of propagation z of the incident beam. The region, within the red lines, is the one with the greatest focusing.

metry with respect to the longitudinal direction of the incident beam, the T-matrix method performs very well thanks to its high precision and calculation speed. Thus, the incident and scattered fields are expanded in a series of vector spherical harmonics with amplitudes $\mathcal{W}_{i,lm}^{(p)}$ and $\mathcal{A}_{s,lm}^{(p)}$, respectively given by Eq. (2.53). Then, as seen in Subsect. (2.5.2), the elements of the transition matrix $T_{l'm'lm}^{(p'p)}$ are calculated by the inversion of the matrix of the linear system, obtained by imposing the boundary conditions to the fields across the surface of the scatterer [see Eq. (2.53)]. As in the previous single sphere case, the incident fields of the scattering problem are the focal fields calculated in the angular spectrum representation [Eq. (1.11)]. Finally, optical forces and trapping properties are obtained through the Maxwell tensor as described in the Chap. (2). A convergence test has been made and we adopted a multipole order $L_M = 8$ for nanowire half-lengths $L/2$ between 50 nm and 500 nm ($N = [1 - 10]$) while $L_M = 15$ for $L/2$ between 600 nm and 1.5 μm ($N = [12 - 30]$).

3.2.1 Optical force components, trap stiffnesses, and size scaling

We present in Fig. (3.6) the results of the computation of the cartesian components of the optical force efficiencies for nanowires with half-length

$L/2 = $ [50 nm, 300 nm, 600 nm, 1400 nm]. We have implemented the same method used in the case of the sphere. Consequently, in Fig. (3.7), we have shown the optical trap stiffnesses, κ_x, κ_y, κ_z, as a function of the half-length of the linear cluster.

In Fig. (3.6), we show how the force acts on nanowires of different lengths. As already done for the single spheres, we investigate an interval of length spanning from the nano- to the microscale. We can immediately notice how in Figs. (3.6a - 3.6b - 3.6c), for short length of the scatterer, the graphs present the typical maximum and minimum that is maintained at the same positions for the transverse, x, y, directions, while it moves approximately with the edges of the nanowire for the axial, z, direction. Consequentially, the linear cluster is trapped at an equilibrium position in proximity to the nominal focus with a small dissipative scattering force. This is a first crucial difference between nanowires and spheres. It is at the ends of the nanowire that a greater trap efficiency is developed in z and, given the particular cylindrical symmetry of the aggregate with respect to the direction of incidence of the beam, the equilibrium point is set at the midpoint of the nanowire. In this regard, heuristic considerations are reported by Simpson and Hanna [115], while experimental demonstrations were obtained by Irrera et al. [38]. As can be expected, when the length of the nanowire grows to such an extent that it is no longer completely contained in the high intensity region of the laser spot, the trap efficiencies collapse towards zero showing the flat pattern of Fig. (3.6d).

Now let us analyze the trap constants size scaling behaviour as the length of the nanowire varies. We plot these trends in Figs. (3.7 - 3.8), where in the latter we have also highlighted the comparison between the scaling for the single sphere and the one for the nanowire. We observe two different trends for κ_x [Fig. (3.7a)] and κ_y [Fig. (3.7b)], in the transverse plane, and κ_z [Fig. (3.7c)] along the longitudinal direction. The transverse stiffnesses show a linear growth at short length that saturates when the length reaches the axial spot size optimizing the optomechanical interaction when the nanowire overlaps the laser spot high intensity region in the axial direction. In other words, the contribution of the spheres, composing the linear cluster, outside the interaction region where trapping takes place, is negligible in the transverse spring constants values.

Instead, the size scaling behaviour of the axial stiffness, κ_z, appears with a similar trend to the one for a single sphere [see Fig. (3.3c)]. The two axial graphs have in common the occurrence of the maximum around 300 nm because, as in the case of a single sphere, the linear aggregate at this particular value has a length comparable with the axial size of the high intensity spot. On the other hand, the main difference between optical trapping of
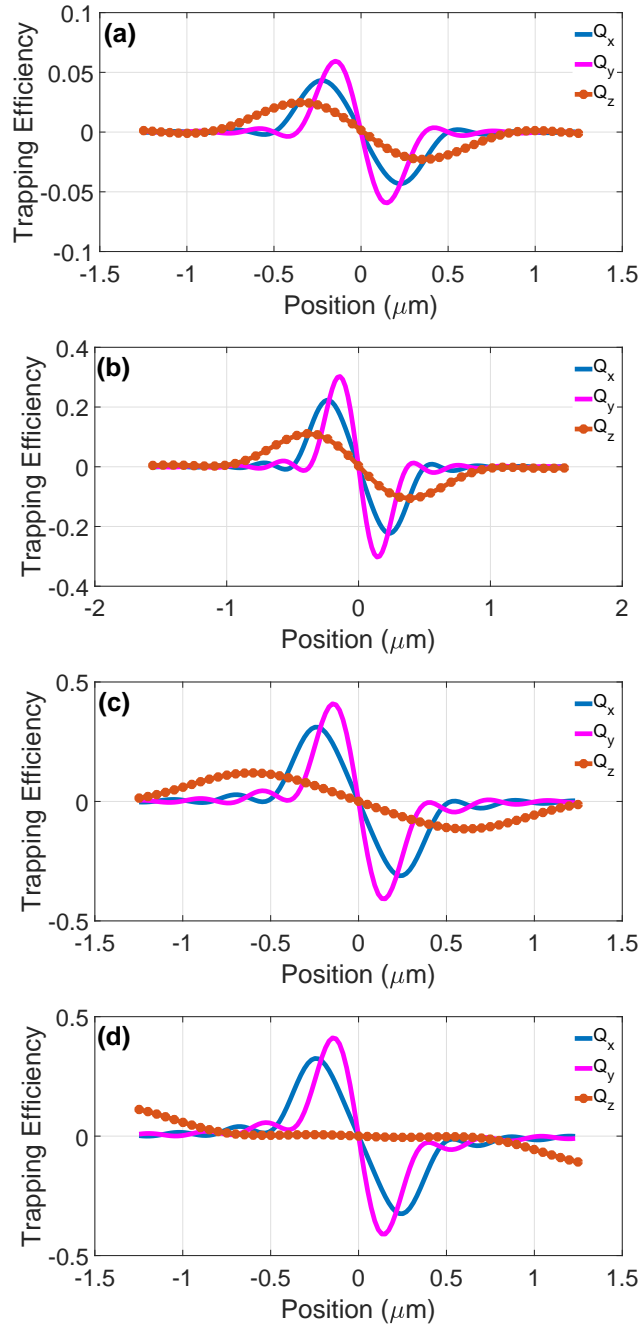
63

Figure 3.6: Trapping efficiencies (Q_x, Q_y, Q_z) for a nanowire composed by latex $(n_\mathrm{p} = 1.57)$ spheres immersed in water $(n_\mathrm{m} = 1.33)$ in the transverse, x - y, and longitudinal z, directions, as function of displacement in the same directions from the location of the paraxial focus. The considered linear clusters have half-length $L/2$: 50 nm (a), 300 nm (b), 600 nm (c), 1400 nm (d). The focus is obtained overfilling an aplanatic water-immersion objective (NA= 1.30).
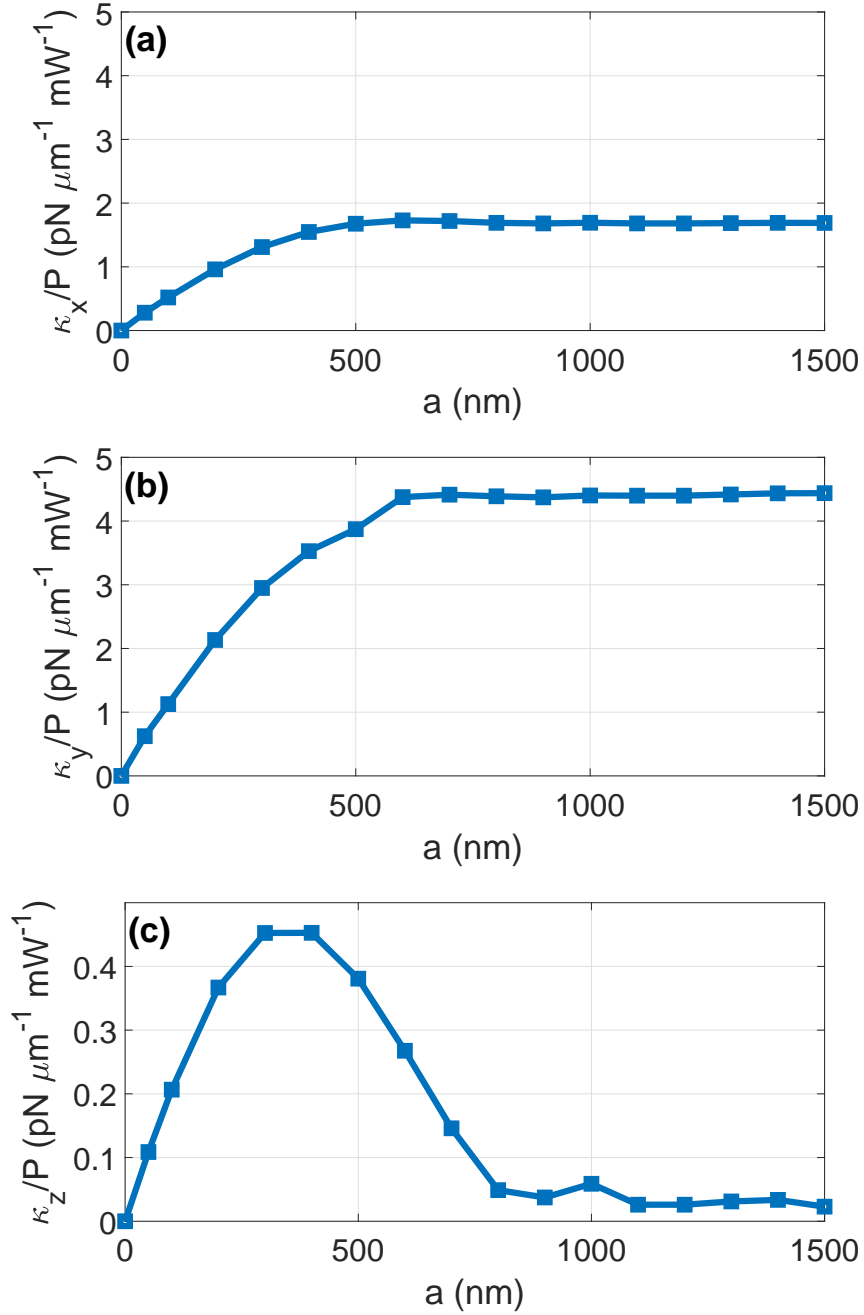
Figure 3.7: Optical trap stiffnesses, κ_x (a), κ_y (b), κ_z (c), for a nanowire composed by latex ($n_\mathrm{p} = 1.57$) spheres immersed in water ($n_\mathrm{m} = 1.33$) in the transverse, x (a) - y (b), and longitudinal z (c), directions, depending on the half-length $L/2$ of the linear cluster. The dimension of the considered aggregate spans in the interval [50 nm - 1500 nm] or, in other words, between number of spheres N [1 − 30].
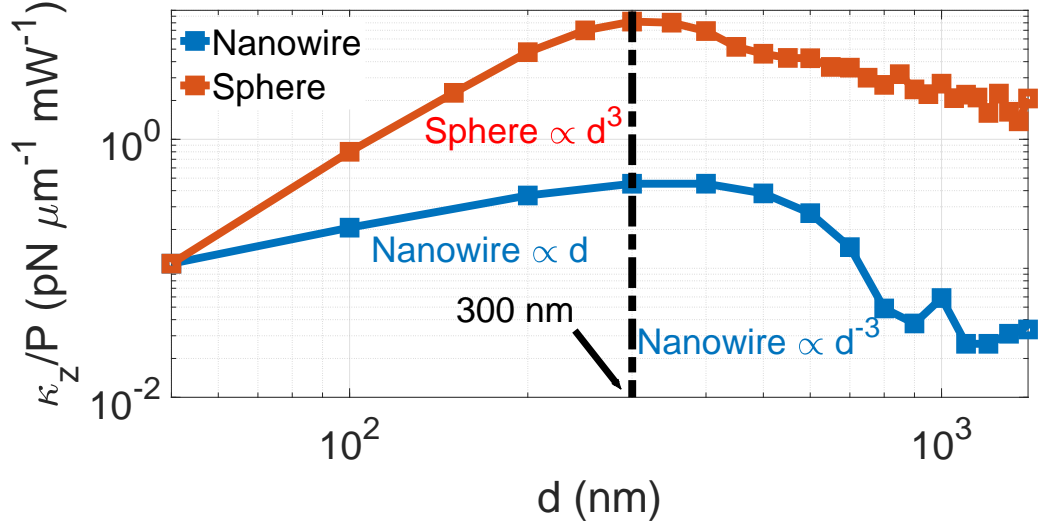
Figure 3.8: Comparison of the optical trap stiffness, in logarithmic scale, κ_z, between a nanowire composed by latex ($n_\mathrm{p} = 1.57$) spheres and a single sphere, immersed in water ($n_\mathrm{m} = 1.33$), depending on the dimension d which is the half-length $L/2$ for the linear cluster and the radius a for the sphere. The dimension spans in the interval [50 nm - 1400 nm]. The two curves have in common an overlap at 300 nm, corresponding to the maximum occupation of the mostly trapped volume. The main difference is in the size scaling: for small size the stiffness of the sphere scales as d^3 while for the nanowire as d; for large size the stiffness on the sphere scales as d^{-1}, while for the linear cluster decreases as d^{-3}.

the two model particles lies in the size scaling as shown in Fig. (3.8). Here we directly compare the size scaling for the two model systems by plotting the axial spring constants for the nanowire as a function of the half-length, $d = L/2$, and for the sphere as a function of its radius, $d = a$. The stiffness of the nanowire grows linearly for short length, $\kappa_z \propto d$, while for the spheres we recall the cubic growth, $\kappa_z \propto d^3$. This is justified in dipole approximation by the one-dimensional geometry of the nanowire growth in contrast to the three-dimensional geometry of the sphere growth. For large length, instead, the axial spring constant decreases in a hyperbolic cubic manner, $\kappa_z \propto d^{-3}$, in contrast to the hyperbolic scaling for the sphere, $\kappa_z \propto d^{-1}$. An appreciable analytical calculation is provided by Simpson et al. [115] while experiments on the size scaling in the optical trapping of silicon nanowires is provided by Irrera et al. [38].

Chapter 4

Spin-dependent optical forces in trapped ZnO nanowires

In this last chapter we present results associated with the onset of a spin-dependent component of the optical force occurring in trapped ZnO nanowires. These components are associated with the 'spin-momentum' part of the Poynting vector, introduced by Belinfante in classical field theory, and directed perpendicularly with respect to the propagation direction of the incident light. We first introduce the general concepts of canonical and spin momentum, then we show calculations of the spin-dependent optical force component on tilted nanowires for plane wave illumination and for optical tweezers. Experimental consequences of spin-dependent transverse forces in trapped ZnO nanowires have been recently observed at CNR-IPCF (Messina).

4.1   Canonical and spin momenta

In quantum mechanics the relation between linear momentum $\mathbf{p}$ and wavevector $\mathbf{k}$ is established through the de Broglie relation, $\mathbf{p} = \hbar\mathbf{k}$. Classically, instead, this assertion is not always true. Poynting introduced the electromagnetic momentum density as a cross product of the electric and magnetic field vectors, $\boldsymbol{\mathcal{S}} \propto \boldsymbol{\mathcal{E}} \times \boldsymbol{\mathcal{H}}$. Unlike the straightforward de Broglie's formula, the Poynting momentum is not obviously associated nor directed as the wavevector $\mathbf{k}$. We can find the alignment with the wavevector, *i.e.*, in the simplest case of a homogeneous plane electromagnetic wave [116]. However, when evanescent fields are considered, the Poynting vector is generally not directed as the local wavevector [117].

The origin of this discrepancy between the Poynting momentum and wavevector lies within the framework of relativistic field theory. The lin-

ear momentum of the electromagnetic field is the spacial part of the total energy-momentum tetra-vector, that is the conserved charge associated to the translational symmetry of space-time in according to Nöether's theorem [118, 119]. Applied to the free electromagnetic field Lagrangian, in vacuum, this theorem produces as Nöether's current the canonical energy-momentum tensor $T_{\text{can}}^{\mu\nu}$, with $\mu, \nu = 0, 1, 2, 3$ temporal and spacial indexes, respectively [117]:

$$T_{\text{can}}^{\mu\nu} = -\frac{1}{4}\eta^{\mu\nu}F^{\rho\sigma}F_{\rho\sigma} + (\partial^\mu A_\rho) F^{\nu\rho}, \tag{4.1}$$

here ∂^μ is the tetra-divergence, A^μ is the electromagnetic tetra-potential, $F^{\mu\nu}$ is the anti-symmetric electromagnetic tensor, $\eta^{\mu\nu}$ is the Minkowski space-time metric tensor, and we have used the natural units $\varepsilon_0 = \mu_0 = c = 1$. This tensor is gauge-dependent but non-symmetric. In 1940, Belinfante suggested a symmetrisation procedure to 'improve' [120] the tensor [Eq. (4.1)], in such manner to make it gauge-invariant and symmetric [121]. He added the following total-divergence term $T_{\text{spin}}^{\mu\nu}$ (constructed from the spin tensor) to the canonical energy-momentum tensor:

$$T_{\text{spin}}^{\mu\nu} = -\partial_\rho \left(A^\mu F^{\nu\rho} \right). \tag{4.2}$$

The resulting symmetric energy-momentum tensor (also known as the *Belinfante energy-momentum tensor*) is:

$$\Theta^{\mu\nu} = T_{\text{can}}^{\mu\nu} + T_{\text{spin}}^{\mu\nu} = -\frac{1}{4}\eta^{\mu\nu}F^{\rho\sigma}F_{\rho\sigma} + F^\mu_{\;\rho}F^{\nu\rho}. \tag{4.3}$$

In turn, the Belinfante spin-correction term [Eq. (4.2)] is usually regarded as 'virtual' because it does not contribute to the energy-momentum conservation law, energy transport, and integral momentum of a localized field [122, 123]. The momentum density of a free electromagnetic field is given by the $\Theta^{i0} \equiv P^i$ spacial components of the energy-momentum tensor. In this manner, the canonical, spin, and Poynting momentum densities, in vectorial form, are obtained from the Eqs. (4.1 - 4.2) as:

$$\mathbf{P}_{\text{can}} = \mathcal{E}_i \nabla \mathcal{A}_i, \tag{4.4}$$

$$\mathbf{P}_{\text{spin}} = -(\boldsymbol{\mathcal{E}} \cdot \nabla)\boldsymbol{\mathcal{A}}, \tag{4.5}$$

$$\boldsymbol{\mathcal{S}} = \mathbf{P}_{\text{can}} + \mathbf{P}_{\text{spin}} = \boldsymbol{\mathcal{E}} \times \boldsymbol{\mathcal{B}} \tag{4.6}$$

where $\boldsymbol{\mathcal{A}}$ is the vector-potential.

Although the canonical and spin momenta are gauge-dependent, there are several strong indications that in a number of situations the experimentally-measured quantities correspond to the canonical quantities taken in some

particular gauge. In optical experiments, the measured quantities correspond to the Coulomb gauge, and hereafter we assume this gauge. In our computation, we are interested in monochromatic optical fields of frequency ω. Then, performing time averaging over the ω-oscillations, we obtain expressions for the time-averaged *canonical, spin*, and *Poynting momentum densities* [see Subsect. (1.5.1)] in a generic optical field [123, 124]:

$$
\begin{aligned}
\langle \mathbf{P}_{\mathrm{can}} \rangle &= \tfrac{1}{2\omega} \Im \left\{ (\mathbf{E}^* \cdot \nabla) \mathbf{E} \right\}, \\
\langle \mathbf{P}_{\mathrm{spin}} \rangle &= \tfrac{1}{4\omega} \nabla \times \Im \left\{ \mathbf{E}^* \times \mathbf{E} \right\}, \\
\langle \mathbf{S} \rangle &= \mathbf{P}_{\mathrm{can}} + \mathbf{P}_{\mathrm{spin}} = \tfrac{1}{2} \Re \left\{ \mathbf{E}^* \times \mathbf{B} \right\}.
\end{aligned}
\tag{4.7}
$$

In the quantum-field framework, the canonical momentum in the Eqs. (4.7) generates spatial translations of the field, in the same way as the de Broglie formula is associated with the operator $\hat{\mathbf{p}} = -i\nabla$ generating translations of a quantum wavefunction. Therefore, the canonical momentum density of monochromatic optical fields is naturally associated with the local wavevector $\mathbf{k}_{\mathrm{loc}}$ of the wave electric field, which is determined by the phase gradient normal to the wavefront [123, 124, 125, 126]:

$$
\langle \mathbf{P}_{\mathrm{can}} \rangle \propto \Re \left\{ (\mathbf{E}^* \cdot \hat{\mathbf{p}}) \mathbf{E} \right\} \propto \mathbf{k}_{\mathrm{loc}} |\mathbf{E}|^2.
\tag{4.8}
$$

In turn, the spin momentum in the Eqs. (4.7) represents a solenoidal edge current, which is generated by the intrinsic spin angular momentum in the field:

$$
\begin{aligned}
\langle \mathbf{P}_{\mathrm{spin}} \rangle &= \tfrac{1}{2} \nabla \times \langle \mathbf{s}_{\mathrm{d}} \rangle \\
\langle \mathbf{s}_{\mathrm{d}} \rangle &= \tfrac{1}{2\omega} \Im \left\{ \mathbf{E}^* \times \mathbf{E} \right\} \propto (\mathbf{E}^* \cdot \hat{\mathbf{s}}) \mathbf{E}
\end{aligned}
\tag{4.9}
$$

where $\hat{\mathbf{s}}$ is the vector of spin-1 matrices [123, 124, 127] and produced by the spin angular momentum density $\mathbf{s}_{\mathrm{d}}$ (that is, the oriented ellipticity of the local polarization) of the field. Owing to its solenoidal nature, this spin momentum does not transport energy, and is usually considered as unobservable *perse*. In contrast to $\mathbf{P}_{\mathrm{can}}$, the Belinfante spin momentum $\mathbf{P}_{\mathrm{spin}}$ is determined by circular polarization and phase inhomogeneity of the field rather than by its wavevector [121, 122, 128, 129]. Thus, the Poynting vector represents a sum of qualitatively different canonical and spin contributions. Moreover, it is the Belinfante spin momentum that is responsible for the difference between the local propagation and Poynting-vector directions in structured light.

This structure of the electromagnetic momentum has traditionally been regarded as an abstract field-theory construction. However, recently it has

been argued that simple optical fields offer an opportunity to investigate, simultaneously and independently, the canonical and spin momenta of light in experiments on optical forces. Antognozzi et al. [117] measured for the first time the extraordinary optical momentum and transverse spin-dependent force using a femtonewton-resolution nano-cantilever immersed in an evanescent optical field above a total internal reflecting glass surface. Bekshaev et al. [129] analyzed the interference field formed by two electromagnetic plane waves (with the same frequency but different wave vectors) and they found that such a field reveals a rich and highly non-trivial structure of the local momentum and spin densities. Basically the idea behind these experiments is the use of non-homogeneous incident fields to bring out measurable effects of the 'Belinfante' contribution.

4.2 Spin-dependent optical forces on tilted ZnO nanowires

In this context, we investigate the occurrence of spin-dependent optical forces on tilted zinc oxide (ZnO) nanowires. Thus, the symmetry breaking of the light scattering problems is governed by the non-spherical shape of the scatterer and its tilting with respect to the circularly polarized light propagation direction. We first study the case of plane wave illumination by calculating the radiation pressure cross sections. Then we study in details the case of a circularly polarized highly focused beam [see Eq. (2.27)], *i.e.* optical tweezers. Our choice is dictated by recent experimental results obtained at CNR-IPCF (Messina) on optically trapped ZnO nanowires (about 1 μm length and 100 nm diameter) in water that show strong evidence of spin-dependent non-conservative effects. For this reason in our calculations we use the same parameters of the experiments.

Our model system is sketched in Fig. (4.1). Ten homogeneous spherical particles, each of 50 nm, are disposed linearly such as to model a cylindrical nanowire with a length of 1 μm immersed in water ($n_{\mathrm{m}} = 1.33$). The particle refractive index is n_{p} ($\lambda_0 = 830$ nm) $= 1.96$ [130]. The incident light has a wavelength of $\lambda_0 = 830$ nm and tight focusing is modeled with an objective lens with numerical aperture NA $= 1.3$. This is the same configuration used in the previous chapter and it generates a focused field as reproduced in Fig. (3.1). To calculate the optical forces on this nanowire we rotate it with respect to its midpoint in the xz plane for values of the polar angle θ in the interval $[0 - \pi/2]$. Given the geometry of the system, we expect the onset of the 'Belinfante' spin-components of the force along the y direction according
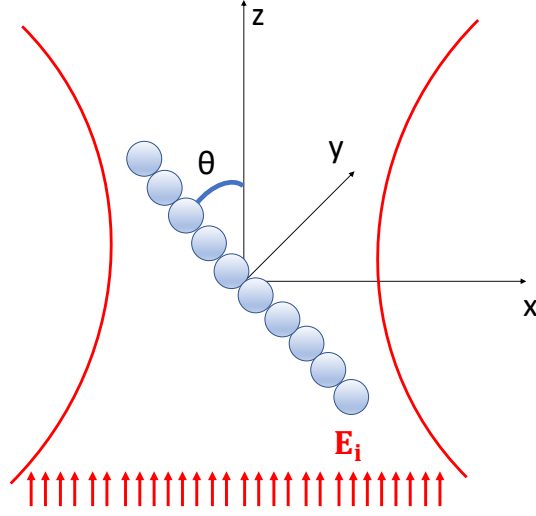
70

Figure 4.1: Model for a tilted nanowire of 1 μm. It is composed by $N = 10$ spheres of radius $a = 50$ nm. The system breaks the cylindrical symmetry with respect to the direction of propagation z of the incident beam and it is tilted of a certain polar angle θ in the xz plane. The red lines represent the focused laser beam that creates the optical trap.

to Eq. (4.9).

4.2.1 Plane wave illumination and radiation pressure cross sections

A first indication of the occurrence of the spin-dependent force component on tilted nanowires is given by calculating the radiation pressure cross sections. We consider plane wave illumination and calculate the cross sections (with sign) as a function of the tilting angle, θ, of the nanowire with respect to the propagation axis. Following the definitions given in Chap. (2), we calculate the quantities $\sigma_{\mathrm{rad}}^x = cF_x/n_{\mathrm{m}}I_0$, $\sigma_{\mathrm{rad}}^y = cF_y/n_{\mathrm{m}}I_0$, $\sigma_{\mathrm{rad}}^z = cF_z/n_{\mathrm{m}}I_0$. The results are shown in Figs. (4.2a - 4.2b - 4.2c). We compare the cross sections for linear (blue) and circularly polarized (red and magenta) plane waves. The first plot, Fig. (4.2a), shows the behaviour of the in-plane transverse $x-$component of the radiation force. Both linear and circular polarization result in a similar trend with tilting angle, showing a negative force pushing the nanowire opposite to its tilting. More importantly both circular polarization, left and right, yield the same transverse radiation pressure cross section (shown in red). Hence the in-plane force $x-$component is the results of the non-spherical shape, but it is not dependent on spin. Similar considerations
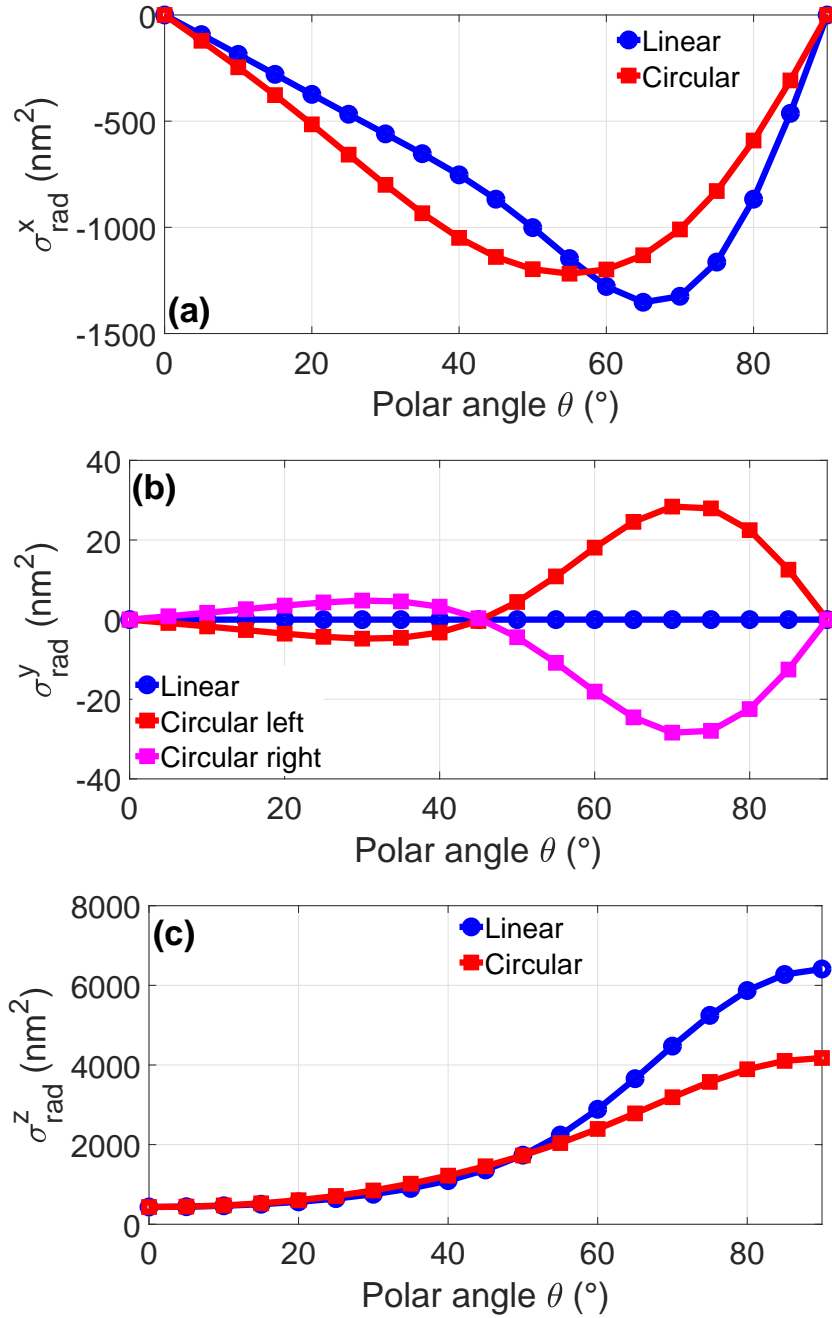
71

Figure 4.2: Radiation pressure cross sections (with sign) $\sigma_{\rm rad}^x$ (a), $\sigma_{\rm rad}^y$ (b), $\sigma_{\rm rad}^z$ (c), as a function of the nanowire tilting polar angle θ. The incoming field is a plane wave. The graph for $\sigma_{\rm rad}^x$ (a) and $\sigma_{\rm rad}^z$ (c) show calculations for linear (blue line) and circular polarization (red line) that are not dependent on the light helicity, i.e., for which $F_{x,z}^{\sigma_+} = F_{x,z}^{\sigma_-}$. Instead, $\sigma_{\rm rad}^y$ (b) shows the spin-dependent cross section for linear (blue line), σ_+ (red line), and (σ_-) (magenta line) polarized light.

hold for Fig. (4.2c), that represents the longitudinal radiation pressure cross section, σ_{rad}^z. In fact, also in this case, both linear and circular polarization yield a similar angular dependence for a positive radiation pressure, and no dependence of the force on light helicity. Instead, a striking difference occurs for the out-of-plane cross section, σ_{rad}^y, shown in Fig. (4.2b). First, this optical force component is zero for linear polarization (blue data). Secondly, for circular polarization a force component occurs as the nanowire is tilted and it changes its sign for opposite circular polarized light. For left-handed light, σ_+, the spin-dependent radiation pressure cross section starts from 0 at $\theta = 0°$, it becomes negative up to $\theta = 45°$, then changes sign up to a maximum at about $\theta = 70°$, and finally goes back to zero, as expected, when the nanowire is at $\theta = 90°$. For right-handed light, σ_-, the dependence is opposite. This clearly shows that the onset of the 'Belinfante' spin-component of the optical force is crucially related to the shape and symmetry of the scatterer and not only to the occurrence of evanescent fields.

4.2.2 Spin-dependent force components in optical tweezers

In this section we present the optical force dependence on the nanowire tilting polar angle θ in the optical tweezers. To calculate them, we used the same method described earlier in Chap. (3) for the latex sphere and nanowire. We use a grid to 'sample' the Cartesian space [see Subsect. (3.1.1)]. However, rather than following the linear cluster at its equilibrium point and calculating its restoring force, we fix the centre-of-mass of the nanowire in the nominal focus of the beam that is the origin of the coordinate system. Thus, we calculate the force components, F_i $(i = x, y, z)$, of the radiation force that is exerted on the tilted nanowire. We perform the calculations for linear (l), left-handed (σ_+) and right-handed (σ_-) circularly polarized incident light. In the Fig. (4.3) we show these forces, normalized to the power P, as a function of polar angle θ that spans from $0°$ to $90°$.

We first note a significant difference between a linear and circular polarization optical tweezers. From Figs. (4.3a - 4.3c), showing the components x and z of the radiation force, we conclude that $F_{x,z}^l \neq F_{x,z}^\sigma$. The reason is that the different polarization, linear or circular, changes the shape of the intensity profile in the focal spot and, hence, the in-plane spin-independent force components, $F_{x,z}$. Furthermore, the x component [Fig. (4.3a)] has two zero points at $0°$ and $90°$ in both linear and circular polarization. This is because in all cases, at these angles, the cluster is symmetric with respect to the propagation axis. The two curves have a minimum in proximity of
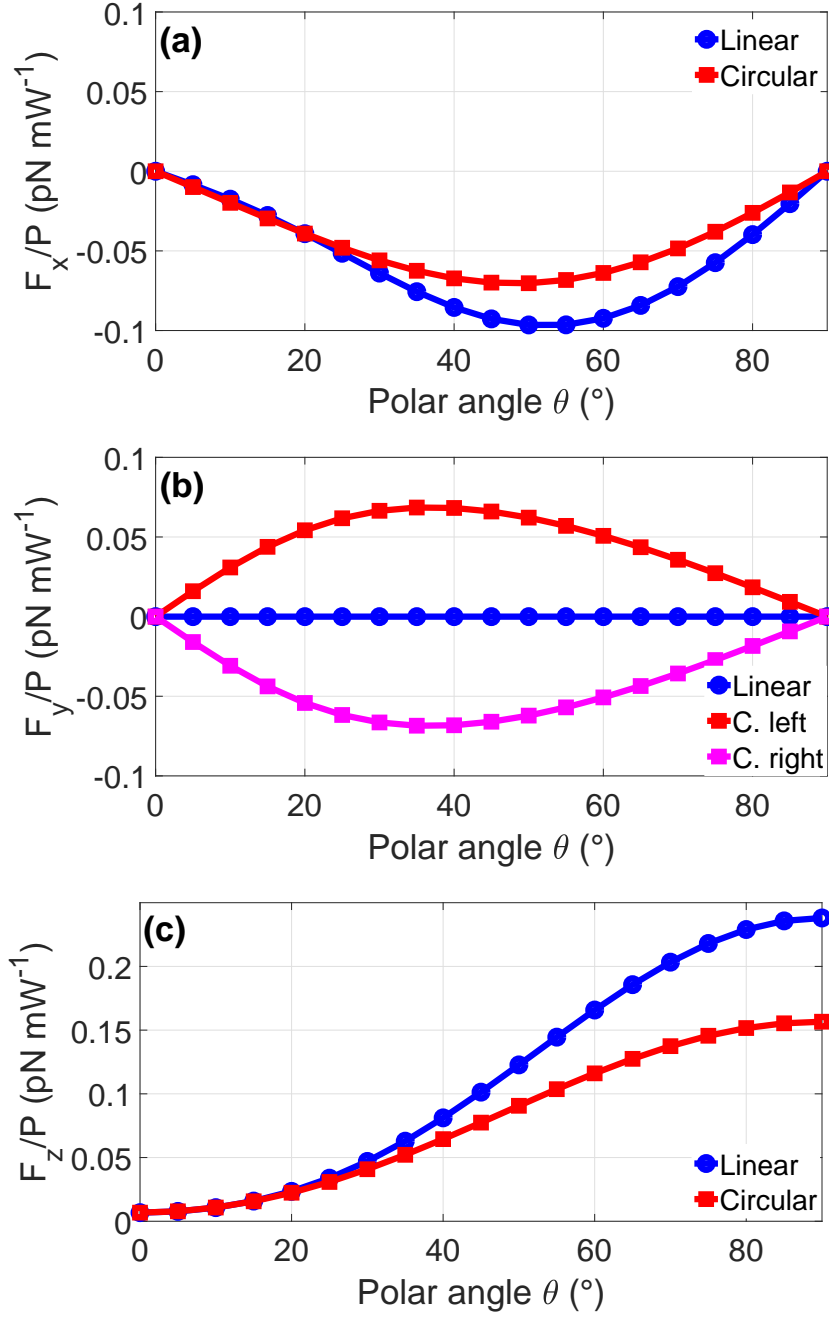
Figure 4.3: Cartesian components of the radiation force normalized to power, F_x/P (a), F_y/P (b), F_z/P (c), as a function of the nanowire tilting polar angle θ in the optical tweezers. The graphs in (a) and (c) show the x and z components for linear (blue line) and circular (red line) polarization for which $F_{x,z}^{\sigma_+} = F_{x,z}^{\sigma_-}$. The plot for the y spin-dependent component is shown for linear (blue line), σ_+ (red line) and (σ_-) (magenta line) polarized light.

$\theta \approx 45°$, which shows that the modulus of the transverse optical force is maximum when the symmetry breaking is maximum. In other words, the nanowire behaves like 'a sail in the wind' that can turn left or right depending on its orientation. This 'sailing effect' is also evident in the longitudinal component, F_z, as visualized in Fig. (4.3c). For both linear and circular polarization $F_z^{l,\sigma}$ at 0° are small and, by tilting the nanowire, they increase until a maximum is reached at $\theta = \pi/2$ when the nanowire is perpendicular to the laser beam propagation direction maximizing its cross section. Both x and z force components are not dependent on the light helicity and the calculations for left-handed (σ_+) and right-handed (σ_-) yield exactly the same results. Instead, Fig. (4.3b) shows a breaking of chiral symmetry since $F_y^{\sigma+}$ is exactly opposite to $F_y^{\sigma-}$ while, for each polar angle F_y^l is null. Thus, the out-of-plane (y) optical force component is spin-dependent and occurs only when the light is circularly polarized. Both circular polarizations show a maximum modulus of the force at around $\theta \approx 45°$, when the symmetry breaking is maximum.

Finally, to better appreciate how the components of the left and right-handed circular polarization forces behave in the focal region, we show the force maps when the nanowire is found at $\theta = [0°, 30°, 60°, 90°]$. These maps, shown in Figs. (4.4 - 4.5 - 4.6 - 4.7), are made by subtracting point-to-point the force components $F_{x,y}^{\sigma-}$ from $F_{x,y}^{\sigma+}$.

Here we analyze the behaviour of the non-conservative force components in a region around the focal spot by moving the nanowire in the transverse xy plane. In particular, we plot the difference $F_i^{\sigma+} - F_i^{\sigma-}$, $i = x, y$ to enhance any chiral effect. In Fig. (4.4) we have this comparison for $\theta = 0$. In this configuration there is a symmetry in the differential maps around the z-axis, the transverse components [Fig. (4.4)] are zero at the origin, while they are non-zero and opposite in sign away from the symmetry axis where the cylindrical symmetry is broken. Figs. (4.5 - 4.6) show the differential maps for $\theta = 30°$ and $\theta = 60°$, respectively. Here the symmetry of the differential maps is fully broken. In particular, for the spin-dependent component, F_y, the map shows three quasi-oblate regions standing out: one around the origin (red) where there is a maximum, and the other two (blue), on the opposite sides of the origin where there is a minimum. Concerning F_x, the difference is much smaller because this component is less dependent on the light helicity and it is not zero only when the nanowire is shifted away from the origin. Finally, at $\theta = 90°$ [see Figs. (4.7a - 4.7c)] the differential maps of $F_{x,y}^{\sigma+} - F_{x,y}^{\sigma-}$ have a much smaller intensity than the tilted cases. This is reasonable since we recover symmetry as for $\theta = 0°$. Moreover, the edges of the nanowire lie away from the high intensity focal spot and therefore, the radiation forces are small because for nanowires optical forces are exerted to the edges [see Chap. (3)].
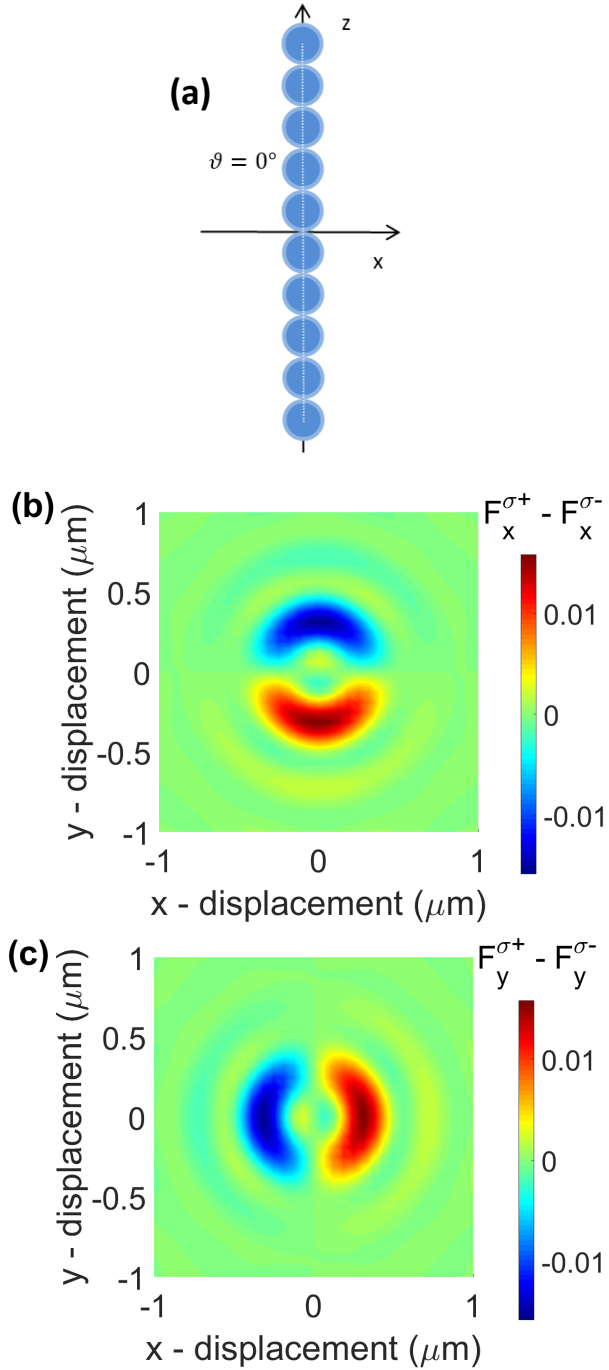
(a)

$\vartheta = 0°$

(b)

$F_x^{\sigma+} - F_x^{\sigma-}$

y - displacement (μm)

x - displacement (μm)

(c)

$F_y^{\sigma+} - F_y^{\sigma-}$

y - displacement (μm)
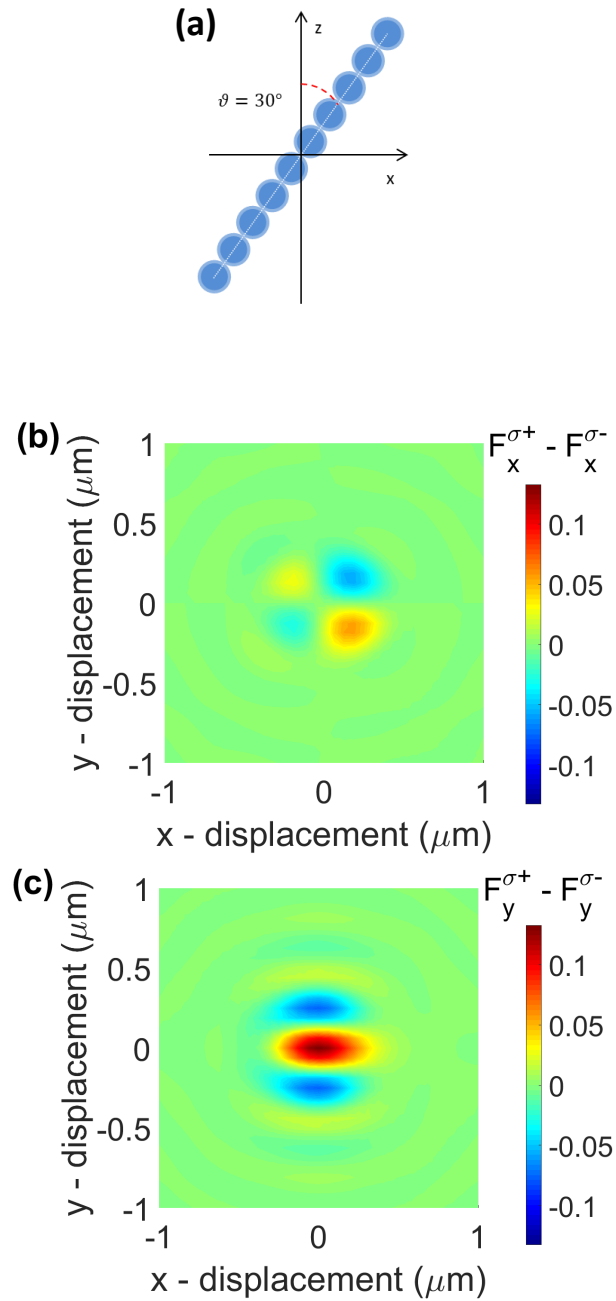
x - displacement (μm)

Figure 4.4: Maps in the xy-plane near the focus of the difference between radiation forces in left circular polarization and right one. The nanowire is at polar angle $\theta = 0°$. Here, the local differences $F_x^{\sigma+} - F_x^{\sigma-}$ (a) and $F_y^{\sigma+} - F_y^{\sigma-}$ (b) are shown and their unit of measure is pN/mW.
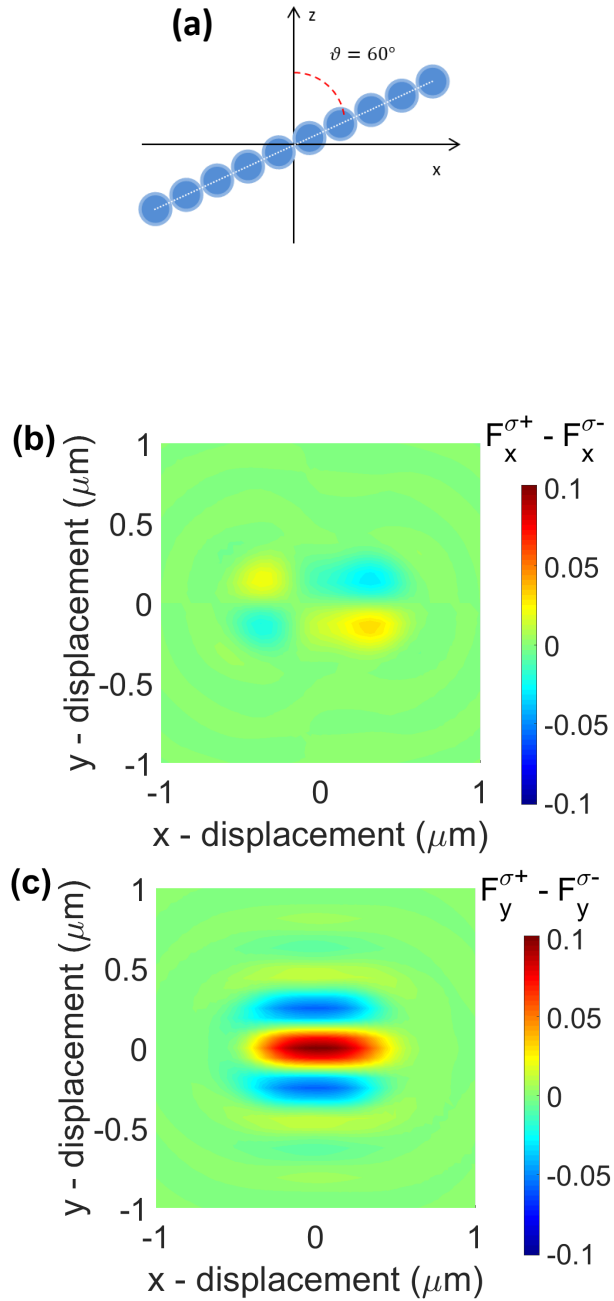
Figure 4.5: Maps in the xy-plane near the focus of the difference between radiation forces in left circular polarization and right one. The nanowire is at polar angle $\theta = 30°$. Here, the local differences $F_x^{\sigma+} - F_x^{\sigma-}$ (a) and $F_y^{\sigma+} - F_y^{\sigma-}$ (b) are shown and their unit of measure is pN/mW.
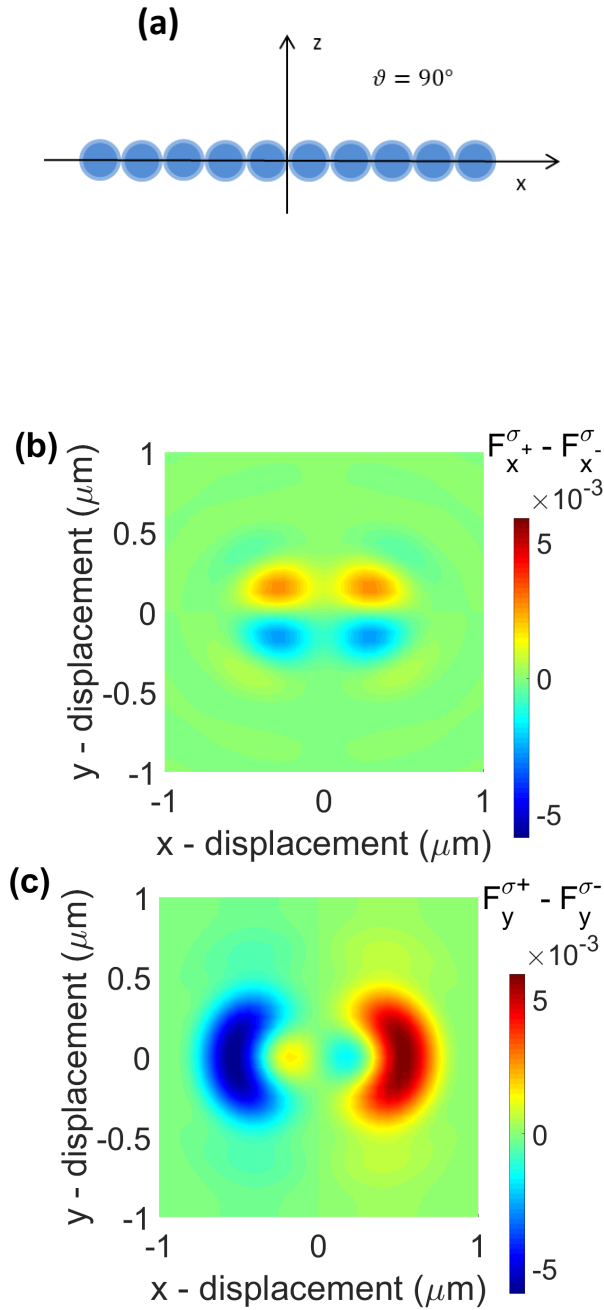
Figure 4.6: Maps in the xy-plane near the focus of the difference between radiation forces in left circular polarization and right one. The nanowire is at polar angle $\theta = 60°$. Here, the local differences $F_x^{\sigma+} - F_x^{\sigma-}$ (a) and $F_y^{\sigma+} - F_y^{\sigma-}$ (b) are shown and their unit of measure is pN/mW.

Figure 4.7: Maps in the xy-plane near the focus of the difference between radiation forces in left circular polarization and right one. The nanowire is at polar angle $\theta = 90°$. Here, the local differences $F_x^{\sigma+} - F_x^{\sigma-}$ (a) and $F_y^{\sigma+} - F_y^{\sigma-}$ (b) are shown and their unit of measure is pN/mW.

As a final remark, we note that our calculations demonstrate the onset of spin-dependent optical force components on optically trapped ZnO nanowires. Experimental consequences of a spin-dependent force component in trapped ZnO nanowires have been recently observed at CNR-IPCF. In brief, due to thermal fluctuations, an optically trapped ZnO nanowire is observed to tilt randomly off-axis. The non-conservative transverse components of the optical force induce a circulation in the centre-of-mass motion that is observed by a novel technique called photonic torque microscopy [131]. Experiments have been performed using linear, left-handed, and right-handed polarization and monitoring the non-conservative orbital motion. In linearly polarized optical tweezers, a trapped nanowire has the same probability of right or left orbital motion. Instead, for left-handed polarization an excess of about 20% in positive circulation is observed, the opposite with right-handed polarization. In conclusion, the extreme particle shape yields spin-dependent transverse components of the radiation pressure that results in a chiral non-conservative orbital rotation of the optically trapped nanowire.

Conclusions

In this master degree thesis we have investigated theoretically optical forces and optical trapping of model spherical particles and nanowires. The theoretical framework we used is based on the formalism of the transition matrix in light scattering as applied to the calculation of optical forces and torques through the Maxwell stress tensor. This approach is accurate and efficient, especially when dealing with the modeling of optical tweezers, *i.e.*, mechanical effects of a tightly focused laser beam.

We first studied in a systematic way the role of particle size and shape on optical forces and optical trapping. They play a key role on characterizing the confining optical potential, trap strength, and trap shape. We have considered size-increasing latex spheres from the nano- to the mesoscale, obtaining the optical restoring forces, trap spring constants, and analyzed their size scaling behaviour. At the nanoscale, we discussed the volumetric, $\sim d^3$, size scaling of optical trap spring constants as expected by simple calculations in dipole approximation. In contrast, for large spherical particles spring constants scale down hyperbolically as $\sim d^{-1}$. Thus, we compared these results with the optical trapping of nanowires aligned with the optical axis and modeled as a linear aggregate of nano-spheres [18]. For short nanowires optical trapping scales linearly with size, $\sim d$, as expected for a one-dimensional system at the nanoscale. In contrast, for long nanowires we obtain a saturation to a constant value in the transverse plane with respect to the light propagation direction and a scaling of $\sim d^{-3}$ in the axial propagation direction. Our calculations are in agreement with the available theoretical and experimental literature on optical trapping of spherical particles and nanowires of different size [18, 115, 38, 114].

In the last part of the thesis, we focused on some novel aspects related with the onset of spin-dependent optical forces related to the spin-component of the Belinfante's linear momentum [117]. In particular, we investigated the role of shape in the occurrence of spin optical force components in tilted ZnO nanowires illuminated by either a circularly polarized plane wave or focused laser beam. In fact, because of the breaking of the cylindrical symmetry

with respect to the optical axis, a non-conservative spin-dependent component occurs when circularly polarized light is incident on a tilted nanowire. We accurately investigated these optical forces components as a function of the nanowire tilting angle. Furthermore, we calculated force maps around the optical trap region to show how these components change with the nanowire position. This is important as in real experiments nanowire are trapped in liquids and they undergo thermal positional fluctuations. Indeed, experimental evidence of the onset of a spin-dependent force component in optical tweezers has been recently observed at CNR-IPCF, where an orbital spin-dependent circulation has been detected in trapped ZnO nanowires. Our calculations support these experimental findings.

Future theoretical work will address the azimuthal dependence, the size scaling, and shape dependence of these spin-dependent optical force components that are predicted to vanish for small spherical particles.

Acknowledgements

Mi scuso anticipatamente con tutti coloro che leggeranno queste righe per la mia proverbiale prolissità. La scelta del Corso Magistrale in Fisica Teorica è stata quasi un salto nel buio. Ringrazio la Dottoressa Antonella Iatì, Ricercatrice dell'Istituto CNR-IPCF di Messina, che ho già avuto il piacere di avere come Supervisor del mio lavoro di tesi al Corso Triennale, per avermi guidato in tale scelta. Parafrasando una delle citazioni del mio Professore di Meccanica Analitica, Domenico Fusco, questo percorso mi ha trasformato da semplice studente appassionato di fisica a fisico, mentre la città di Bologna mi ha formato come uomo. Ringrazio tutti i professori e colleghi universitari con cui ho avuto modo di scambiare ed arricchire le mie conoscenze utili all'acquisizione del metodo scientifico. In particolare Antonello e Flavio per le discussioni sulla fisica e per avermi aiutato ad entrare nella vita del Dipartimento.

Un ringraziamento speciale al mio relatore Prof. Cristian Degli Esposti-Boschi, non solo per avermi permesso di svolgere il lavoro di tesi fuori sede, ma anche per i preziosi suggerimenti sulla stesura dell'elaborato finale. Così ho potuto lavorare ancora una volta all'Istituto CNR-IPCF di Messina, dove ho avuto modo di conoscere uno staff di ricercatori all'avanguardia in diversi settori, che mi hanno accolto come uno di loro. Ringrazio i miei co-supervisor, la Dr.ssa Antonella Iatì ed il Dr. Onofrio Maragò, con i quali ho la fortuna di poter lavorare. Mi hanno permesso di interfacciarmi con nuove tematiche di ricerca e di ottenere risultati innovativi nel campo della fisica teorica della materia. Ringrazio la Prof.ssa Rosalba Saija dell'Università di Messina per avermi introdotto al linguaggio computazionale e aiutato nell'interpretazione dei risultati. Altresì sono grato alla Dott.ssa Maria Grazia Donato per il prezioso aiuto in fase di revisione finale dell'elaborato.

Infine, vorrei concludere i ringraziamenti citando coloro a cui dedico la mia tesi. Alla mia famiglia. Nonno Nato e Nonna Mora, a Voi che, prima di andare via per sempre, avreste voluto vedermi laureato: sono sicuro, ovunque siate, che mi state guardando ed organizzando qualche 'mangiata'. Papà, Mamma, Tiziana e Paolo, non riesco ad esprimere con le parole la mia pro-

fonda gratitudine nei vostri confronti. Mi avete sostenuto anche nei momenti più difficili, quando volevo mollare tutto. Avete sempre creduto in me, dandomi la libertà di fare ciò che desideravo. Per la vostra pazienza e supporto sotto tutti i punti di vista: grazie. Il meglio l'ho lasciato per ultimo: al mio Sole. Mariasole, a te che mi hai accompagnato da metà del mio percorso, in occasione dello sprint finale. Con il tuo amore, mi hai dato una forza che prima non credevo di avere, mi hai fatto capire che nulla è impossibile e che con il potere della volontà posso raggiungere ogni traguardo. Per me sei luce fatta persona e ci sei stata sempre a sostenermi anche negli innumerevoli giorni in cui non eri fisicamente presente: ti amo.

Bibliography

[1] Ashkin A. Atomic-beam deflection by resonance-radiation pressure. *Physical Review Letters*, 25(19):1321, 1970.

[2] Ashkin A. Acceleration and trapping of particles by radiation pressure. *Physical Review Letters*, 24(4):156, 1970.

[3] Ashkin A. History of optical trapping and manipulation of small-neutral particle, atoms, and molecules. *IEEE Journal of Selected Topics in Quantum Electronics*, 6(6):841–856, 2000.

[4] Ashkin A., Dziedzic J.M., Bjorkholm J.E., and Chu S. Observation of a single-beam gradient force optical trap for dielectric particles. *Optics Letters*, 11(5):288–290, 1986.

[5] Jones P.H., Maragò O.M., and Volpe G. *Optical tweezers: Principles and applications.* Cambridge University Press, Cambridge, UK, 2015.

[6] Ashkin A., Dziedzic J.M., and Yamane T. Optical trapping and manipulation of single cells using infrared laser beams. *Nature*, 330(6150):769–771, 1987.

[7] Ashkin A. and Dziedzic J.M. Optical trapping and manipulation of viruses and bacteria. *Science*, 235:1517–1521, 1987.

[8] Foot C.J. *Atomic physics*, volume 7. Oxford University Press, 2005.

[9] Dholakia K. and Čižmár T. Shaping the future of manipulation. *Nature Photonics*, 5(6):335–342, 2011.

[10] Padgett M. and Bowman R. Tweezers with a twist. *Nature Photonics*, 5(6):343–348, 2011.

[11] Fazal F.M. and Block S.M. Optical tweezers study life under tension. *Nature Photonics*, 5(6):318–321, 2011.

[12] Maragò O.M., Jones P.H., Gucciardi P.G., Volpe G., and Ferrari A.C. Optical trapping and manipulation of nanostructures. *Nature Nanotechnology*, 8(11):807–819, 2013.

[13] Maragò O.M., Gucciardi P.G., and Jones P.H. Photonic force microscopy: From femtonewton force sensing to ultra-sensitive spectroscopy. In *Scanning Probe Microscopy in Nanoscience and Nanotechnology*, pages 23–56. Springer, 2010.

[14] Olof S.N., Grieve J.A., Phillips D.B., Rosenkranz H., Yallop M.L., Miles M.J., Patil A.J., Mann S., and Carberry D.M. Measuring nanoscale forces with living probes. *Nano Letters*, 12(11):6018–6023, 2012.

[15] Chaumet P.C. and Nieto-Vesperinas M. Time-averaged total force on a dipolar sphere in an electromagnetic field. *Optics Letters*, 25(15):1065–1067, 2000.

[16] Ashkin A. Forces of a single-beam gradient laser trap on a dielectric sphere in the ray optics regime. *Biophysical Journal*, 61(2):569–582, 1992.

[17] Borghese F., Denti P., Saija R., and Iatì M.A. Optical trapping of nonspherical particles in the T-matrix formalism. *Optics Express*, 15(19):11984–11998, 2007.

[18] Borghese F., Denti P., Saija R., Iatì M.A., and Maragò O.M. Radiation torque and force on optically trapped linear nanostructures. *Physical Review Letters*, 100(16):163903, 2008.

[19] Donato M.G., Messina E., Foti A., Smart T.J., Jones P.H., Iatì M.A., Saija R., Gucciardi P.G., and Maragò O.M. Optical trapping and optical force positioning of two-dimensional materials. *Nanoscale*, 2018.

[20] Waterman P.C. Symmetry, unitarity, and geometry in electromagnetic scattering. *Physical Review D*, 3(4):825, 1971.

[21] Borghese F., Denti P., and Saija R. *Scattering from model nonspherical particles: Theory and applications to environmental physics*. Springer Science & Business Media, 2007.

[22] Mie G. Beiträge zur optik trüber medien, speziell kolloidaler metallösungen. *Annalen der Physik*, 330(3):377–445, 1908.

[23] Mishchenko M.I., Travis L.D., and Lacis A.A. *Scattering, absorption, and emission of light by small particles*. Cambridge University Press, 2002.

[24] Saija R., Iatì M.A, Borghese F., Denti P., Aiello S., and Cecchi-Pestellini C. Beyond Mie theory: The transition matrix approach in interstellar dust modeling. *The Astrophysical Journal*, 559(2):993, 2001.

[25] Iatì M.A., Giusto A., Saija R., Borghese F., Denti P., Cecchi-Pestellini C., and Aiello S. Optical properties of composite interstellar grains: A morphological analysis. *The Astrophysical Journal*, 615(1):286, 2004.

[26] Amendola V., Pilot R., Frasconi M., Maragò O.M., and Iatì M.A. Surface plasmon resonance in gold nanoparticles: A review. *Journal of Physics: Condensed Matter*, 29(20):203002, 2017.

[27] Kepler J. De cometis libelli tres, 1619.

[28] Maxwell J.C. *A Treatise on electricity and magnetism*. Clarendon Press, Oxford, 1873.

[29] Lebedew P. Untersuchungen über die druckkräfte des lichtes. *Annalen der Physik*, 311(11):433–458, 1901.

[30] Nichols E.F. and Hull G.F. A preliminary communication on the pressure of heat and light radiation. *Physics Review*, 13:307–320, 1901.

[31] Maiman T.H. Stimulated optical emission in ruby. In *Journal of the Optical Society of America*, volume 50, pages 1134–1134. Amer Inst Physics 1305 Walt Whitman RD, Ste 300, Melville, NY 11747-4501 USA, 1960.

[32] Ashkin A. and Dziedzic J.M. Optical levitation by radiation pressure. *Applied Physics Letters*, 19(8):283–285, 1971.

[33] Magazzú A. *Optical trapping and thermal dynamics of Silicon nanowires*. PhD thesis, Universitá degli studi di Messina, 2015.

[34] Magazzú A., Spadaro D., Donato M.G., Sayed R., Messina E., D'Andrea C., Foti A., Fazio B., Iatí M.A., Irrera A., et al. Optical tweezers: A non-destructive tool for soft and biomaterial investigations. *Rendiconti Lincei*, 26(2):203–218, 2015.

[35] Neuman K.C. and Nagy A. Single-molecule force spectroscopy: Optical tweezers, magnetic tweezers and atomic force microscopy. *Nature Methods*, 5(6):491–505, 2008.

[36] Svoboda K. and Block S.M. Biological applications of optical forces. *Annual Review of Biophysics and Biomolecular Structure*, 23(1):247–285, 1994.

[37] Marago O.M., Jones P.H., Bonaccorso F., Scardaci V., Gucciardi P.G., Rozhin A.G., and Ferrari A.C. Femtonewton force sensing with optically trapped nanotubes. *Nano Letters*, 8(10):3211–3216, 2008.

[38] Irrera A., Artoni P., Saija R., Gucciardi P.G., Iatì M.A., Borghese F., Denti P., Iacona F., Priolo F., and Marago O.M. Size-scaling in optical trapping of silicon nanowires. *Nano Letters*, 11(11):4879–4884, 2011.

[39] Ashkin A. Forces of a single-beam gradient laser trap on a dielectric sphere in the ray optics regime. *Methods in Cell Biology*, 55:1–27, 1997.

[40] Gordon J.P. Radiation forces and momenta in dielectric media. *Physical Review A*, 8(1):14, 1973.

[41] Purcell E.M. and Pennypacker C.R. Scattering and absorption of light by nonspherical dielectric grains. *The Astrophysical Journal*, 186:705–714, 1973.

[42] Born M. and Wolf E. *Principles of optics: Electromagnetic theory of propagation, interference and diffraction of light.* Cambridge University Press, Cambridge, United Kingdom, 1999.

[43] Callegari A., Mijalkov M., Gököz A.B., and Volpe G. Computational toolbox for optical tweezers in geometrical optics. *JOSA B*, 32(5):B11–B19, 2015.

[44] Swartzlander jr G.A., Peterson T.J., Artusio-Glimpse A.B., and Raisanen A.D. Stable optical lift. *Nature Photonics*, 5(1):48–51, 2011.

[45] Skelton S.E., Sergides M., Memoli G., Maragó O.M., and Jones P.H. Trapping and deformation of microbubbles in a dual-beam fibre-optic trap. *Journal of Optics*, 14(7):075706, 2012.

[46] Wolf E. Electromagnetic diffraction in optical systems. I. An integral representation of the image field. In *Proceedings of the Royal Society of London A: Mathematical, Physical and Engineering Sciences*, volume 253, pages 349–357. The Royal Society, 1959.

[47] Richards B. and Wolf E. Electromagnetic diffraction in optical systems. II. Structure of the image field in an aplanatic system. In *Proceedings of the Royal Society of London A: Mathematical, Physical and Engineering Sciences*, volume 253, pages 358–379. The Royal Society, 1959.

[48] Debye P. Das verhalten von lichtwellen in der nähe eines brennpunktes oder einer brennlinie. *Annalen der Physik*, 335(14):755–776, 1909.

[49] Dholakia K. and Zemánek P. Colloquium: Gripped by light: Optical binding. *Reviews of Modern Physics*, 82(2):1767, 2010.

[50] Draine B.T. and Goodman J. Beyond clausius-mossotti-wave propagation on a polarizable point lattice and the discrete dipole approximation. *The Astrophysical Journal*, 405:685–697, 1993.

[51] Albaladejo S., Laroche M.I., Marquésand M., and Sáenz J.J. Scattering forces from the curl of the spin angular momentum of a light field. *Physical Review Letters*, 102(11):113602, 2009.

[52] Marqués M.I. and Sáenz J.J. Reply to comment on scattering forces from the curl of the spin angular momentum of a light field. *Physical Review Letters*, 111(5):059302, 2013.

[53] Donato M.G., Vasi S., Sayed R., Jones P.H., Bonaccorso F., Ferrari A.C., Gucciardi P.G., and Maragò O.M. Optical trapping of nanotubes with cylindrical vector beams. *Optics Letters*, 37(16):3381–3383, 2012.

[54] Skelton S.E., Sergides M., Saija R., Iatì M.A., Maragó O.M., and Jones P.H. Trapping volume control in optical tweezers using cylindrical vector beams. *Optics Letters*, 38(1):28–30, 2013.

[55] Marqués M.I. Beam configuration proposal to verify that scattering forces come from the orbital part of the poynting vector. *Optics Letters*, 39(17):5122–5125, 2014.

[56] Brzobohatỳ O., Šiler M., Trojek J., Chvátal L., Karásek V., Paták A., Pokorná Z., Mika F., and Zemánek P. Three-dimensional optical trapping of a plasmonic nanoparticle using low numerical aperture optical tweezers. *Scientific Reports*, 5:8106, 2015.

[57] Brzobohatỳ O., Arzola M. A.V., Šiler, Chvátal L., Jákl P., Simpson S., and Zemánek P. Complex rotational dynamics of multiple spheroidal particles in a circularly polarized, dual beam trap. *Optics Express*, 23(6):7273–7287, 2015.

[58] Kuhn S., Asenbaum P., Kosloff A., Sclafani M., Stickler B.A., Nimm-richter S., Hornberger K., Cheshnovsky O., Patolsky F., and Arndt M. Cavity-assisted manipulation of freely rotating silicon nanorods in high vacuum. *Nano Letters*, 15(8):5604–5608, 2015.

[59] Kuhn S., Kosloff A., Stickler B.A., Patolsky F., Hornberger K., Arndt M., and Millen J. Full rotational control of levitated silicon nanorods. *Optica*, 4(3):356–360, 2017.

[60] Zemánek P., Jonáš A., Šrámek L., and Liška M. Optical trapping of rayleigh particles using a gaussian standing wave. *Optics Communications*, 151(4-6):273–285, 1998.

[61] Barker P.F. and Shneider M.N. Cavity cooling of an optically trapped nanoparticle. *Physical Review A*, 81:023826, 2010.

[62] Chang D.E., Regal C.A., Papp S.B., Wilson D.J., Ye J., Painter O., Kimble H.J., and Zoller P. Cavity opto-mechanics using an optically levitated nanosphere. *Proceedings of the National Academy of Sciences of U.S.A.*, 107:1005–1010, 2010.

[63] Romero-Isart O., Juan M.L., Quidant R., and Cirac J.I. Toward quantum superposition of living organisms. *New Journal of Physics*, 12:033015, 2010.

[64] Braginskii V.B. and Manukin A.B. *Measurement of weak forces in physics experiments*. University of Chicago Press, Chicago, IL, 1977.

[65] Abbott B.P., Abbott R., Abbott T.D., Abernathy M.R., Acernese F., Ackley K., Adams C., Adams T., Addesso P., Adhikari R.X., et al. Observation of gravitational waves from a binary black hole merger. *Physical Review Letters*, 116(6):061102, 2016.

[66] Novotny L. and Hecht B. *Principles of nano-optics*. Cambridge University Press, Cambridge, United Kingdom, 2012.

[67] Kippenberg T.J. and Vahala K.J. Cavity opto-mechanics. *Optical Express*, 15:17172–17205, 2007.

[68] Wilson-Rae I., Nooshi N., Zwerger W., and Kippenberg T.J. Theory of ground state cooling of a mechanical oscillator using dynamical back-action. *Physical Review Letters*, 99:093901, 2007.

[69] Marquardt F., Chen J.P., Clerk A.A., and Girvin S.M. Quantum theory of cavity-assisted sideband cooling of mechanical motion. *Physical Review Letters*, 99:093902, 2007.

[70] Cohen-Tannoudji C., Dupont-Roc J., and Grynberg G. *Atom-photon interactions: Basic processes and applications*. John Wiley & Sons, Inc., New York, NY, 1992.

[71] Gardiner C. and Zoller P. *Quantum noise: A handbook of Markovian and non-Markovian quantum stochastic methods with applications to quantum optics*. Springer Verlag, Heidelberg, Germany, 2004.

[72] Schliesser A., Rivière R., Anetsberger G., Arcizet O., and Kippenberg T.J. Resolved-sideband cooling of a micromechanical oscillator. *Nature Physics*, 4:415–419, 2008.

[73] Romero-Isart O., Pflanzer A.C., Juan M.L., Quidant R., Kiesel N., Aspelmeyer M., and Cirac J.I. Optically levitating dielectrics in the quantum regime: Theory and protocols. *Physical Review A*, 83:013803, 2011.

[74] Kiesel N., Blaser F., Delić U., Grass D., Kaltenbaek R., and Aspelmeyer M. Cavity cooling of an optically levitated submicron particle. *Proceedings of the National Academy of Sciences of U.S.A.*, 110:14180–14185, 2013.

[75] Li T., Kheifets S., and Raizen M.G. Millikelvin cooling of an optically trapped microsphere in vacuum. *Nature Physics*, 7:527–530, 2011.

[76] Gieseler J., Deutsch B., Quidant R., and Novotny L. Subkelvin parametric feedback cooling of a laser-trapped nanoparticle. *Physical Review Letters*, 109:103603, 2012.

[77] Borghese F., Saija P., Denti R., Toscano G., and Sindoni O.I. Multiple electromagnetic scattering from a cluster of spheres. I. Theory. *Aerosol Science and Technology*, 3(2):227–235, 1984.

[78] Draine B.T. The discrete-dipole approximation and its application to interstellar graphite grains. *The Astrophysical Journal*, 333:848–872, 1988.

[79] Mishchenko M.I. Radiation force caused by scattering, absorption, and emission of light by nonspherical particles. *Journal of Quantitative Spectroscopy and Radiative Transfer*, 70(4-6):811–816, 2001.

[80] Nieminen T.A., Rubinsztein-Dunlop H., and Heckenberg N.R. Calculation and optical measurement of laser trapping forces on non-spherical particles. *Journal of Quantitative Spectroscopy and Radiative Transfer*, 70(4-6):627–637, 2001.

[81] Saija R., Iatì M.A., Giusto A., Denti P., and Borghese F. Transverse components of the radiation force on nonspherical particles in the T-matrix formalism. *Journal of Quantitative Spectroscopy and Radiative Transfer*, 94(2):163–179, 2005.

[82] Piccirillo B., Slussarenko S., Marrucci L., and Santamato E. The orbital angular momentum of light: Genesis and evolution of the concept and of the associated photonic technology. *Rivista Nuovo Cimento*, 36(11):501–555, 2013.

[83] Stratton J.A., Morse P.M, Chu L.J., and Hutner R.A. *Elliptic cylinder and spheroidal wave functions: Including tables of separation constants and coefficients.* J. Wiley & sons, inc., 1941.

[84] Ishimaru A. Wave propagation and scattering in random media and rough surfaces. *Proceedings of the IEEE*, 79(10):1359–1366, 1991.

[85] Van de Hulst H.C. *Light scattering by small particles.* Courier Corporation, 1957.

[86] Fucile E., Denti P., Borghese F., Saija R., and Sindoni O.I. Optical properties of a sphere in the vicinity of a plane surface. *Journal of the Optical Society of America A*, 14(7):1505–1514, 1997.

[87] Wyatt P.J. Scattering of electromagnetic plane waves from inhomogeneous spherically symmetric objects. *Physical Review*, 134(7AB):AB1, 1964.

[88] Abramowitz M. and Stegun I.A. *Handbook of mathematical functions with formulas, graphs and mathematical table*, volume 2172. Dover New York, 1965.

[89] Gustafson B.Å.S., Kolokolova L., Xu Y., Greenberg J.M., and Stognienko R. Interactions with electromagnetic radiation: Theory and laboratory simulations. In *Interplanetary dust*, pages 509–567. Springer, 2001.

[90] Bruning J. and Lo Y. Multiple scattering of e.m. waves by spheres part I. Multipole expansion and ray-optical solutions. *IEEE Transactions on Antennas and Propagation*, 19(3):378–390, 1971.

[91] Peterson B. and Ström S. T-matrix formulation of electromagnetic scattering from multilayered scatterers. *Physical Review D*, 10(8):2670, 1974.

[92] Gerardy J.M. and Ausloos M. Absorption spectrum of clusters of spheres from the general solution of Maxwell's equations. The long-wavelength limit. *Physical Review B*, 22(10):4950, 1980.

[93] Borghese F., Denti P., Toscano G., and Sindoni O.I. An addition theorem for vector helmholtz harmonics. *Journal of Mathematical Physics*, 21(12):2754–2755, 1980.

[94] Quinten M., Kreibig U., Henning T., and Mutschke H. Wavelength-dependent optical extinction of carbonaceous particles in atmospheric aerosols and interstellar dust. *Applied Optics*, 41(33):7102–7113, 2002.

[95] Wiscombe W.J. *Mie scattering calculations: Advances in technique and fast, vector-speed computer codes.* National Technical Information Service, US Department of Commerce, 1979.

[96] Simpson S.H. Inhomogeneous and anisotropic particles in optical traps: Physical behaviour and applications. *Journal of Quantitative Spectroscopy and Radiative Transfer*, 146:81–99, 2014.

[97] Nieminen T.A., Du Preez-Wilkinson N., Stilgoe A.B., Loke V.L.Y., Bui A.A.M., and Rubinsztein-Dunlop H. Optical tweezers: Theory and modelling. *Journal of Quantitative Spectroscopy and Radiative Transfer*, 146:59–80, 2014.

[98] Borghese F., Denti P., Saija R., and Iatì M.A. Radiation torque on non-spherical particles in the transition matrix formalism. *Optics Express*, 14(20):9508–9521, 2006.

[99] Simpson S.H. and Hanna S. Numerical calculation of interparticle forces arising in association with holographic assembly. *Journal of the Optical Society of America A*, 23(6):1419–1431, 2006.

[100] Simpson S.H. and Hanna S. Optical trapping of spheroidal particles in gaussian beams. *Journal of the Optical Society of America A*, 24(2):430–443, 2007.

[101] Saija R., Denti P., Borghese F., Maragó O.M., and Iatì M.A. Optical trapping calculations for metal nanoparticles. Comparison with experimental data for Au and Ag spheres. *Optics Express*, 17(12):10231–10241, 2009.

[102] Nieminen T.A., Loke V.L.Y., Stilgoe A.B., Heckenberg N.R., and Rubinsztein-Dunlop H. T-matrix method for modelling optical tweezers. *Journal of Modern Optics*, 58(5-6):528–544, 2011.

[103] Marston P.L. and Crichton J.H. Radiation torque on a sphere caused by a circularly-polarized electromagnetic wave. *Physical Review A*, 30(5):2508, 1984.

[104] Rohrbach A. Stiffness of optical traps: Quantitative agreement between experiment and electromagnetic theory. *Physical review letters*, 95(16):168102, 2005.

[105] Sultanova N., Kasarova S., and Nikolov I. Characteristics of optical polymers in the design of polymer and hybrid optical systems. *Bulgarian Journal of Physics*, 40(3):258–264, 2013.

[106] Wolf E.L. *Nanophysics and nanotechnology: An introduction to modern concepts in nanoscience.* John Wiley & Sons, 2015.

[107] Alivisatos A.P. Semiconductor clusters, nanocrystals and quantum dots. *Science*, 271(5251):933–937, 1996.

[108] Gudiksen M.S., Lauhon L.J., Wang J., Smith D.C., and Lieber C.M. Growth of nanowire superlattice structures for nanoscale photonics and electronics. *Nature*, 415(6872):617, 2002.

[109] Dick K.A. A review of nanowire growth promoted by alloys and non-alloying elements with emphasis on Au-assisted III–V nanowires. *Progress in Crystal Growth and Characterization of Materials*, 54(3-4):138–173, 2008.

[110] Pesce G., Volpe Giorgio, Maragò O.M., Jones P.H., Gigan S., Sasso A., and Volpe Giovanni. Step-by-step guide to the realization of advanced optical tweezers. *Journal of the Optical Society of America B*, 32(5):B84–B98, 2015.

[111] Nieminen T.A., Stilgoe A.B., Heckenberg N.R., and H Rubinsztein-Dunlop. Approximate and exact modeling of optical trapping. In *Optical Trapping and Optical Micromanipulation VII*, volume 7762, page 77622V. International Society for Optics and Photonics, 2010.

[112] Briggs A. and Kolosov O. *Acoustic microscopy*, volume 67. Oxford University Press, 2010.

[113] Huang Y., Duan X., Cui Y., Lauhon L.J., Kim K.H., and Lieber C.M. Logic gates and computation from assembled nanowire building blocks. *Science*, 294(5545):1313–1317, 2001.

[114] Reece P.J., Toe W.J., F. Wang, Paiman S., Gao Q., Tan H.H., and Jagadish C. Characterization of semiconductor nanowires using optical tweezers. *Nano Letters*, 11(6):2375–2381, 2011.

[115] Simpson S.H. and Hanna S. Stability analysis and thermal motion of optically trapped nanowires. *Nanotechnology*, 23(20):205502, 2012.

[116] Jackson J.D. *Classical electrodynamics*. AAPT, 1999.

[117] Antognozzi M., Bermingham C.R., Harniman R.L., Simpson S., Senior J., Hayward R., Hoerber H., Dennis M.R., Bekshaev A.Y., Bliokh K.Y., et al. Direct measurements of the extraordinary optical momentum and transverse spin-dependent force using a nano-cantilever. *Nature Physics*, 12(8):731, 2016.

[118] Bogoliubov N.N. and Shirkov D.V. *Introduction to the theory of quantized fields*. Interscience Publisher, New York, USA, 1959.

[119] Lifschitz L.D. and Landau E.M. *Teoria dei campi*. Editori Riuniti, Roma, IT, 1976.

[120] Soldati R. Introduction to Quantum Field Theory. Online notes, Bologna, February 2018. http://www.robertosoldati.com.

[121] Belinfante F.J. On the current and the density of the electric charge, the energy, the linear momentum and the angular momentum of arbitrary fields. *Physica*, 7(5):449–474, 1940.

[122] Ohanian H.C. What is spin? *American Journal of Physics*, 54(6):500–505, 1986.

[123] Bliokh K.Y., Bekshaev A.Y., and Nori F. Dual electromagnetism: Helicity, spin, momentum and angular momentum. *New Journal of Physics*, 15(3):033026, 2013.

[124] Berry M.V. Optical currents. *Journal of Optics A: Pure and Applied Optics*, 11(9):094001, 2009.

[125] Bliokh K.Y., Bekshaev A.Y., Kofman A.G., and Nori F. Photon trajectories, anomalous velocities and weak measurements: A classical interpretation. *New Journal of Physics*, 15(7):073022, 2013.

[126] Barnett S.M. and Berry M.V. Superweak momentum transfer near optical vortices. *Journal of Optics*, 15(12):125701, 2013.

[127] Bliokh K.Y. and Nori F.N. Transverse and longitudinal angular momenta of light. *Physics Reports*, 592:1–38, 2015.

[128] Bliokh K.Y., Bekshaev A.Y., and Nori F. Extraordinary momentum and spin in evanescent waves. *Nature Communications*, 5:3300, 2014.

[129] Bekshaev A.Y., Bliokh K.Y., and Nori F. Transverse spin and momentum in two-wave interference. *Physical Review X*, 5(1):011039, 2015.

[130] Bond W.L. Measurement of the refractive indices of several crystals. *Journal of Applied Physics*, 36(5):1674–1677, 1965.

[131] Irrera A., Magazzú A., Artoni P., Simpson S.H., Hanna S., Jones P.H., Priolo F., Gucciardi P.G., and Maragó O.M. Photonic torque microscopy of the nonconservative force field for optically trapped silicon nanowires. *Nano Letters*, 16(7):4181–4188, 2016.